

DESIGN AND ANALYSIS OF MICROWAVE PASSIVE DEVICES USING  
TAPERED LINES



*Ramanand Sagar Sangam*



**DESIGN AND ANALYSIS OF MICROWAVE PASSIVE DEVICES  
USING TAPERED LINES**

A

*Thesis Submitted*

*in Partial Fulfilment of the Requirements*

*for the Degree of*

**DOCTOR OF PHILOSOPHY**

By

**RAMANAND SAGAR SANGAM**



DEPARTMENT OF ELECTRONICS AND ELECTRICAL ENGINEERING

INDIAN INSTITUTE OF TECHNOLOGY GUWAHATI

GUWAHATI - 781 039, ASSAM, INDIA

March 2020



## Declaration

I hereby declare that the thesis entitled “**Design and Analysis of Microwave Passive Devices Using Tapered Lines**”, submitted in the *Department of Electronics and Electrical Engineering, Indian Institute of Technology Guwahati, Assam, India*, for the award of the degree of **Doctor of Philosophy**, has been carried out by me under the supervision and guidance of Prof. Rakesh Singh Kshetrimayum. The results embodied in this thesis are original and have not been submitted to any other University or Institute for the award of any degree or diploma.

Dated:

Ramanand Sagar Sangam

Place: Guwahati

Research Scholar

Dept. of Electronics and Electrical Engineering

Indian Institute of Technology Guwahati

Guwahati - 781039, Assam, India.



## Certificate

This is to certify that the thesis entitled “**DESIGN AND ANALYSIS OF MICROWAVE PASSIVE DEVICES USING TAPERED LINES**”, submitted by **Ramanand Sagar Sangam** (146102015), a research scholar in the *Department of Electronics and Electrical Engineering, Indian Institute of Technology Guwahati*, for the award of the degree of **Doctor of Philosophy**, is a record of an original research work carried out by him under our supervision and guidance. The thesis has fulfilled all requirements as per the regulations of the institute and in my opinion has reached the standard needed for submission. The results embodied in this thesis have not been submitted to any other University or Institute for the award of any degree or diploma.

Dated:  
Guwahati.

Prof. Rakhesh Singh Kshetrimayum  
Professor  
Dept. of Electronics and Electrical Engg.  
Indian Institute of Technology Guwahati  
Guwahati - 781 039, Assam, India.





*To my grand parents and parents*



## Acknowledgements

First and foremost, I feel it as a great privilege in expressing my deepest and most sincere gratitude to my supervisor Prof. Rakesh Singh Kshetrimayum for his excellent guidance throughout my PhD tenure. His kindness, dedication and attention to the details has been a source of great inspiration to me. My heartfelt thanks to my supervisor for his unlimited support and patience that he has shown towards me. His emphasis on clear communication helped me a lot. He has enriched my life in many significant ways. I thank him from the bottom of my heart for always being there with me during my journey as a research scholar at IIT Guwahati.

I would like to thank my doctoral committee members: Dr. R. K. Sonkar, Prof. A. K. Sarma, and Dr. N. Nallam for sparing time out of their busy schedule to evaluate my progress and enrich this work with their valuable suggestions and feedbacks. I extend my sincere thanks to Mr. U. K. Sarma and all the staff members from EEE office and academic office for helping me out in all sorts of ways during my stay at IIT Guwahati.

During my PhD, I found really wonderful lab-mates and fellow research scholars. I express my sincere thanks to my seniors Dr. Jitendra Prajapati, Dr. Somen Bhattacharjee and Dr. Anand Agarwal for some of the extremely important discussions and feedbacks during the initial days of my PhD. I had a great time with my many friends at IIT Guwahati including but not limited to Vimal Kr. S. Yadav, Mohit Joshi, Mohit Mishra, Anirban Bhowal, Sumantra Chaudhury, Sanjib Mog, Sumit Dash, R. Uikay, R. Palthiya, S. Poolakkal, P. Anoop, Pawan Kumar, Prateek Rathore, Arijit Roy, Rahul Nair and Kaushik Debbarma. These guys made my stay at IIT Guwahati memorable. I will cherish the time spent with them. I thank them all for their friendship.

My deepest gratitude goes to my family for their continuous love and support throughout my studies. The opportunities that they have given me and their unlimited sacrifices are the reasons where I am and what I have accomplished so far. They have been and will remain my source of inspiration to achieve every possible height in my journey.

Finally, I believe this research experience will greatly benefit my career in the future.

*Ramanand Sagar Sangam*



# Abstract

The research work presented in this thesis deals with size miniaturization and performance enhancement of various microwave passive devices using tapered lines and spoof surface plasmon polariton (SSPP) on planar type of transmission line like microstrip line and substrate integrated waveguide (SIW). Microwave passive devices and components such as filters, power dividers, directional couplers and antennas are the essential building blocks of microwave circuits and systems. In the modern time of ever-expanding wireless and consumer electronics market, it is highly desirable to design these devices which have a compact size, lower cost, lighter weight with superior performances.

Novel bandpass filters are designed, analyzed and fabricated for ultra-wideband (UWB) (3.1-10.6 GHz) applications. To suppress the interference from IEEE 802.11a WLAN band signals in UWB spectrum, sharp notch stopband around 5.5 GHz has been created using exponentially tapered impedance line stub loaded microstrip resonator. The theoretical characterization of tapered lines such as triangular taper, exponential taper, and Klopfenstein taper are proposed many years ago, but for practical realization, linear tapers are the most common and simple tapers which are widely used for impedance matching, eliminating the step discontinuities between transmission lines, and in the design of power dividers, directional couplers, filters, antennas, etc. Although linear tapers have been used in the design of such several microwave devices, theoretical characterization of such taper is not available in the literature. Hence, the theoretical characterization of linear tapers is presented in this work. Subsequently, using linearly tapered microstrip lines (MSLs), a taper transition between microstrip line and substrate integrated waveguide (SIW) component, an ultra-broadband bandpass filter, and an unequal T-junction power divider have been designed, fabricated and tested. The proposed T-junction power dividers could be very useful in UWB or super-wideband (SWB) system where coupling ratio of more than 10 dB over a very broad range of frequency is desired for a passive signal cancellation. A

very compact dual-port, aperture coupled and tapered fed patch antenna with a very high isolation has been proposed for in-band full-duplex 2.4 GHz ISM applications. The same technique could further be utilized for designing antennas for in-band full-duplex radios such as for WiMAX applications.

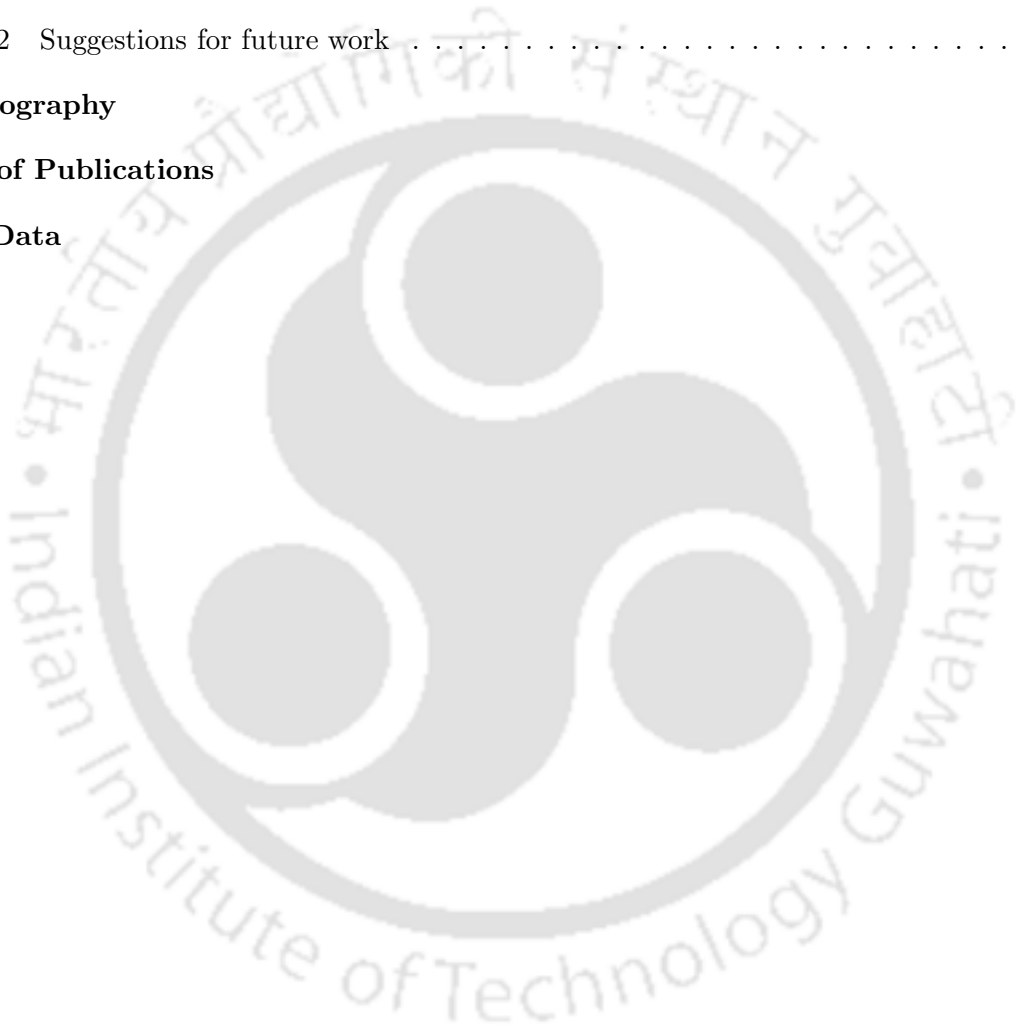
SIW is a relatively new type of transmission line which provides the bridge between bulky metallic waveguide and lossy planar technology. By using the curve fitting technique, an approximate design equation has been developed for calculating the width of iris windows of iris SIW bandpass filter. An iris SIW bandpass filter at V-band has also been designed to validate the proposed method. A taper transition is generally required to connect microstrip line and SIW for smooth impedance and field matching between them over a broad range of frequency. Also, the introduction of slow-wave or low pass characteristics of SSPP in SIW offers higher performances broadband microwave devices. Hence, using hybrid structure of linear taper, SIW and SSPP, broadband bandpass filters with wide out-of-band rejection have been designed for X-band applications. A dumbbell-shaped SSPP has been proposed, which shows more slow-wave effects than rectangle-shaped SSPP for the same height of grooves. Hence, it could be used efficiently in the design of compact, low loss and highly integrated microwave devices. The size of proposed hybrid SSPP-SIW filters are very compact, amounts to only about a wavelength at the center frequency, which is much lesser than the length of existing hybrid SSPP-SIW filters.

# Contents

List of Figures	xix
List of Tables	xxiii
List of Acronyms	xxv
<b>1 Introduction</b>	<b>1</b>
1.1 Microstrip line	2
1.2 Introduction to tapers	4
1.2.1 Exponential taper	5
1.2.2 Triangular taper	6
1.2.3 Klopfenstein taper	6
1.3 Microwave passive devices	8
1.3.1 Filters	8
1.3.2 Power dividers	10
1.3.3 Antennas	12
1.4 Research background and motivation	13
1.5 Contribution of the thesis	18
1.6 Thesis organization	19
<b>2 Notched UWB filter using ETILSLMR</b>	<b>21</b>
2.1 Introduction	22
2.2 Initial UWB filter design	24
2.2.1 Theoretical analysis of proposed UWB filter	27
2.3 Notched-band UWB filter design	28
2.3.1 Theoretical analysis of notched-band UWB filter	32
2.4 Comparison with measured results	34

2.5	Summary . . . . .	37
<b>3</b>	<b>Linear tapers: analysis, design and applications</b>	<b>39</b>
3.1	Introduction . . . . .	40
3.2	Linear impedance taper . . . . .	42
3.3	Comparison with different tapered lines . . . . .	44
3.4	Linearly tapered transition between microstrip line and SIW component . . . . .	47
3.5	Linearly tapered coupled-line ultra-broadband bandpass filter . . . . .	51
3.5.1	Filter structure and operation . . . . .	51
3.5.2	Implementation and experimental results . . . . .	56
3.6	Summary . . . . .	58
<b>4</b>	<b>Broadband T-junction power dividers using linear taper</b>	<b>59</b>
4.1	Introduction . . . . .	60
4.2	Design and analysis . . . . .	61
4.2.1	An approximate theoretical analysis . . . . .	61
4.3	Simulation and experimental results . . . . .	66
4.4	Summary . . . . .	72
<b>5</b>	<b>Dual-port, aperture coupled and linearly tapered fed full-duplex antenna</b>	<b>73</b>
5.1	Introduction . . . . .	74
5.2	Antenna design . . . . .	76
5.3	Results and discussion . . . . .	78
5.4	Summary . . . . .	84
<b>6</b>	<b>Filters design using SIW, SSPP and linear taper</b>	<b>85</b>
6.1	Iris SIW bandpass filter for V-band applications . . . . .	86
6.1.1	Introduction . . . . .	86
6.1.2	Design techniques . . . . .	87
6.1.3	Approximate design equation . . . . .	88
6.1.4	Iris SIW bandpass filter design . . . . .	91
6.2	Hybrid SSPP-SIW bandpass filters for X-band applications . . . . .	92
6.2.1	Introduction . . . . .	92
6.2.2	Dispersion characteristics of SIW and SSPPs . . . . .	94

6.2.3 Demonstration of hybrid SSPP-SIW bandpass filters . . . . .	98
6.3 Comment on “ [1]” . . . . .	107
6.4 Summary . . . . .	109
<b>7 Conclusions and future work</b>	<b>111</b>
7.1 Conclusions . . . . .	112
7.2 Suggestions for future work . . . . .	113
<b>Bibliography</b>	<b>115</b>
<b>List of Publications</b>	<b>123</b>
<b>Bio-Data</b>	<b>125</b>





# List of Figures

1.1	Microstrip line (a) Geometry and (b) Electric and magnetic field lines. . . . .	3
1.2	A tapered transmission line and the model for an incremental length of the tapered line (a) Continuously tapered transmission line and (b) Model for an incremental step change in impedance of the tapered line. . . . .	4
1.3	Reflection coefficient magnitude response for the different tapers. . . . .	7
2.1	Configuration of the design with single SC stub. . . . .	25
2.2	Simulated S-parameters of the design with single SC stub. . . . .	25
2.3	Schematic of the initial UWB filter design. . . . .	26
2.4	Simulated S-magnitudes of the initial UWB filter. . . . .	27
2.5	Equivalent configuration of the initial UWB filter. . . . .	28
2.6	Comparison of simulation with analytical results for the designed UWB filter. . . . .	29
2.7	Configuration of the notched-band design with single tapered SC stub. . . . .	29
2.8	Simulated results for the notched-band design with single tapered SC stub (a) $ S_{21} $ for different tapered widths $W_3$ and (b) S-parameters with $W_3 = 10$ mm. . . . .	30
2.9	Proposed notched-band UWB filter structure. . . . .	31
2.10	Predicted magnitude of S parameters for the notched-band UWB filter. . . . .	31
2.11	Proposed two-section short-circuited transmission line structure. . . . .	32
2.12	Comparison of simulation with analytical S-magnitudes for the notched-band UWB filter. . . . .	33
2.13	Photograph of the fabricated filters. . . . .	33
2.14	Comparison of measured and simulated results for the initial UWB filter. . . . .	34
2.15	Comparison of measured and simulated results for the proposed UWB filter with notch function. . . . .	35
3.1	(a) Linear impedance taper and (b) Linear width taper. . . . .	42

## List of Figures

---

3.2	Reflection coefficient magnitude response for the linear impedance taper. . . . .	43
3.3	Impedance variations for the different tapers. . . . .	44
3.4	Width variations for the different tapers. . . . .	45
3.5	Reflection coefficient magnitude versus frequency for the different tapers. . . . .	46
3.6	Schematic of the linearly tapered transition between microstrip line and SIW section. . . . .	47
3.7	SIW model with different transitions (a) No transition (b) 3 steps transition (c) 5 steps transition and (d) Linearly tapered transition. . . . .	48
3.8	$ S_{21} $ for stepped vs. linearly tapered transition. . . . .	49
3.9	$ S_{11} $ for stepped vs. linearly tapered transition. . . . .	49
3.10	Prototype of fabricated linearly tapered transition between microstrip line and SIW component. . . . .	50
3.11	S-parameters of the linearly tapered transition (Solid lines represent simulated results and dashed lines represent measured results). . . . .	50
3.12	Schematic of the proposed ultra-broadband BPF design (a) Top view and (b) Bottom view (open loop DGS on the ground). . . . .	51
3.13	The model with different coupled-lines (a) 3 stepped (b) 6 stepped and (c) Linearly tapered coupled-line. . . . .	52
3.14	Simulated $ S_{21} $ of 3 stepped, 6 stepped and linearly tapered coupled-lines without open loop DGS. . . . .	53
3.15	Simulated $ S_{21} $ for different tapered widths $w_3$ in mm, without open loop DGS. . . . .	54
3.16	Simulated S-parameters for different gap widths $g$ in mm (with open loop DGS on the ground). . . . .	55
3.17	Simulated S-parameters (HFSS and CST) for the proposed ultra-broadband BPF. . . . .	56
3.18	The photographs of fabricated prototype proposed BPF (a) Top view and (b) Bottom view. . . . .	56
3.19	S-parameters of the proposed BPF (Solid lines represent simulated results and dashed lines represent measured results). . . . .	57
3.20	Group delay of the proposed BPF. . . . .	57
4.1	(a) Layout of the proposed unequal T-junction power divider and (b) Equivalence of (a) in terms of ABCD parameters of elementary block. . . . .	62

4.2	Analysis model of the design. . . . .	63
4.3	Equivalent 2-port network of Figure 1 when (a) Port-3 is terminated with the matched load $Z_0$ and (b) Port-2 is terminated with the matched load $Z_0$ . . . . .	64
4.4	Theory and simulated S-parameters of the power divider. Black lines $\rightarrow$ theory & gray lines $\rightarrow$ HFSS results. . . . .	66
4.5	Simulated S-parameters of the power divider for varying $w_3$ in mm. . . . .	67
4.6	Simulated amplitude and phase response of $S_{21}$ & $S_{31}$ for the power divider. . . . .	68
4.7	Simulated amplitude and phase response of $S_{32}$ for the power divider. . . . .	69
4.8	Simulated S-parameters of the power divider. Black lines $\rightarrow$ HFSS results and gray lines $\rightarrow$ CST results. . . . .	70
4.9	Simulated S-parameters of the SWB T-junction power divider. . . . .	70
4.10	Photograph of the prototype fabricated T-junction power divider. . . . .	71
4.11	S-parameters of the T-junction power divider (Solid lines represent HFSS simulated results and dashed lines represent measured results). . . . .	71
5.1	Geometry of the proposed antenna. . . . .	77
5.2	$ S_{11} $ vs frequency of dual-port patch antenna. . . . .	78
5.3	$ S_{22} $ vs frequency of dual-port patch antenna. . . . .	78
5.4	$ S_{21} $ vs frequency of dual-port patch antenna. . . . .	79
5.5	Surface current distributions at all three metallic surfaces when Port-1 is excited. . . . .	80
5.6	Surface current distributions at all three metallic surfaces when Port-2 is excited. . . . .	81
5.7	Radiation pattern (port 1) of the dual-port patch antenna at 2.4 GHz. . . . .	82
5.8	Radiation pattern (port 2) of the dual-port patch antenna at 2.4 GHz. . . . .	83
6.1	Model of inductive window and its equivalent circuit. . . . .	88
6.2	Plot of iris width variation corresponding to normalized inverter parameter K. . . . .	89
6.3	3 <sup>rd</sup> order iris SIW bandpass filter design. . . . .	91
6.4	Simulated frequency response of the designed iris SIW BPF. . . . .	92
6.5	Configuration of unit cells (a) SIW unit (b) Rectangle-shaped SSPP unit and (c) Dumbbell-shaped SSPP unit. . . . .	94

## List of Figures

---

6.6	Dispersion diagrams (a) SIW unit (b) Rectangle-shaped & dumbbell-shaped SSPP units and (c) Different radii of dumbbell-shaped SSPP unit. . . . .	95
6.7	Dispersion diagrams of hybrid SSPP-SIW units (a) Rectangle-shaped and (b) Dumbbell-shaped with fixed $r = 0.41$ mm. . . . .	96
6.8	Configuration of the hybrid SSPP-SIW structure with graded rectangular slots heights of $h_i$ ( $i = 1, 2, 3, 4$ ) ( $a = 14.85$ mm, $h = 6.5$ mm, $W = 17.5$ mm, $L_1 = 9.25$ mm, $W_1 = 1.565$ mm, $L_2 = 6$ mm, $W_2 = 3.625$ mm and $L_3 = 21.6$ mm). . . . .	98
6.9	Simulated S-parameters of the hybrid SSPP-SIW structure with varied graded rectangular slots heights, $h_i$ ( $i = 1, 2, 3, 4$ ). . . . .	99
6.10	Configurations of the proposed hybrid SSPP-SIW filters (a) Rectangle-shaped and (b) Dumbbell-shaped. . . . .	100
6.11	Simulated transmission coefficients of the proposed hybrid SSPP-SIW structures (a) Different widths of SIW with rectangle-shaped SSPP (b) Different heights of rectangle-shaped SSPP and (c) Different radii of dumbbell-shaped SSPP with fixed $h = 6.5$ mm. . . . .	101
6.12	Electric field distributions of the rectangle-shaped SSPP-SIW bandpass filter (a) At the lower frequency stopband (b) At the passband and (c) At the upper frequency stopband. . . . .	102
6.13	Electric field distributions of the rectangle-shaped SSPP-SIW bandpass filter (a) Across the cross-sections at 10.25 GHz and (b) 0.5 mm above the top surface at 10.25 GHz. . . . .	102
6.14	Electric field distributions of the dumbbell-shaped SSPP-SIW bandpass filter (a) At the lower frequency stopband (b) At the passband and (c) At the upper frequency stopband. . . . .	104
6.15	Electric field distributions of the dumbbell-shaped SSPP-SIW bandpass filter (a) Across the cross-sections at 10.25 GHz and (b) 0.5 mm above the top surface at 10.25 GHz. . . . .	104
6.16	Photograph of the fabricated prototype rectangle-shaped SSPP-SIW BPF. . . . .	105
6.17	Photograph of the fabricated prototype dumbbell-shaped SSPP-SIW BPF. . . . .	105
6.18	S-parameters of the rectangle-shaped SSPP-SIW bandpass filter (Solid lines represent simulated results and dashed lines represent measured results). . . . .	105
6.19	S-parameters of the dumbbell-shaped SSPP-SIW bandpass filter (Solid lines represent simulated results and dashed lines represent measured results). . . . .	106
6.20	Dispersion diagrams (a) SSPP unit and (b) SIW unit. . . . .	107
6.21	Dispersion curves for varied SSPP unit parameters. . . . .	108

# List of Tables

2.1	Design parameter values for the initial UWB filter . . . . .	26
2.2	Design parameter values for the notched-band UWB filter . . . . .	31
2.3	Comparison of notch band characteristics with reported notched-band UWB filters . .	36
4.1	Performance comparison of the power divider with existing unequal T-junction power dividers . . . . .	72
5.1	Performance comparison (experimental) of the proposed antenna with the antennas available in the literature . . . . .	84
6.1	Calculated and theoretical normalized inverter parameters for different iris width . . .	90
6.2	Design parameters of rectangle-shaped hybrid SSPP-SIW filter (Units: mm) . . . . .	100
6.3	Performance comparison with the existing planar SIW filters . . . . .	106



# List of Acronyms

ACS	Asymmetric Coplanar Strip
BPF	Bandpass Filter
BW	Bandwidth
CAD	Computer-Aided Design
CPW	Coplanar Waveguide
CSSRR	Complementary Single Split Ring Resonator
CST	Computer Simulation Technology
DGS	Defected Ground Structure
EBG	Electromagnetic Bandgap
EM	Electromagnetic
ESM	Electronic Support Measure
ETILSLMR	Exponentially Tapered Impedance Line Stub Loaded Microstrip Resonator
FBW	Fractional Bandwidth
FCC	Federal Communications Commission
FDD	Frequency Division Duplex
FEM	Finite Element Method
FM	Frequency Modulation
HFSS	High Frequency Structure Simulator
HMSIW	Half Mode Substrate Integrated Waveguide
HTS	High-Temperature Superconductor
IEEE	Institute of Electrical and Electronics Engineer
IL	Insertion Loss
ISM	Industrial, Scientific and Medical
LTCC	Low-Temperature Cofired Ceramics

## List of Acronyms

---

MEMS	Microelectromechanical System
MMIC	Monolithic Microwave Integrated Circuits
MMR	Multiple-Mode Resonator
MSL	Microstrip Line
PCB	Printed Circuit Board
PCM	Pulse Code Modulation
RF	Radio Frequency
RFID	Radio Frequency Identification
RL	Return Loss
SCRLH	Simplified Composite Right/Left Handed
SIW	Substrate Integrated Waveguide
SMA	Sub Miniature A
SPP	Surface Plasmon Polariton
SSPP	Spoof Surface Plasmon Polariton
SWB	Super-Wideband
TDD	Time Division Duplex
TE	Transverse Electric
TEM	Transverse Electromagnetic
TL	Transmission Line
UTL	Uniform Transmission Line
UWB	Ultra-Wideband
VNA	Vector Network Analyzer
VSWR	Voltage Standing-Wave Ratio
WiMAX	Worldwide Inter-operability for Microwave Access
WLAN	Wireless Local Area Network



# 1

## Introduction

### Contents

---

1.1	Microstrip line . . . . .	2
1.2	Introduction to tapers . . . . .	4
1.3	Microwave passive devices . . . . .	8
1.4	Research background and motivation . . . . .	13
1.5	Contribution of the thesis . . . . .	18
1.6	Thesis organization . . . . .	19

---

Microwave passive devices such as filters, power dividers, directional couplers and antennas are the essential components of microwave communication, test and measurement systems. In the present day, it is highly desirable to design these devices in compact size, lower cost, lighter weight with superior performances. Over the past several decades, a lot of research works has been carried out to achieve these requirements using planar transmission lines like microstrip line and substrate integrated waveguide (SIW). In this introductory chapter, we briefly present the background and underlying motivation of this research to design planar microwave passive devices and antenna for different microwave applications. Further, contribution and organization of the thesis are outlined in this chapter.

### 1.1 Microstrip line

Microstrip line is one of the simplest and most popular type of planar transmission line, as it can be fabricated by photolithographic processes and easily integrated with other active and passive microwave devices. The geometry of a microstrip line is shown in Figure 1.1(a). It consists of a strip conductor of width  $W$  and thickness  $t$ , printed on a grounded substrate of height  $h$  and relative permittivity  $\epsilon_r$ . Unlike stripline, where all the field lines are confined in a homogeneous dielectric medium, microstrip has most of the field lines concentrated between the strip conductor and the ground plane, and some fraction in the air region above the strip, as depicted in Figure 1.1(b). Hence, due to inhomogeneous nature and so phase mismatch occurs at the dielectric-air interface, a microstrip line cannot support a pure TEM wave.

The exact fields inside microstrip constitute a hybrid TE-TM waves which requires more advanced analysis techniques. In most practical applications, dielectric substrate is electrically very thin ( $h \ll \lambda$ ), that means longitudinal components of the fields in a microstrip line would be very much smaller than transverse components which can be neglected, and so the fields are quasi-TEM [2]. For quasi-TEM microstrip lines, we can replace the inhomogeneous air-dielectric media with an equivalent homogeneous dielectric medium having effective permittivity  $\epsilon_e$ , ( $1 < \epsilon_e < \epsilon_r$ ) which is dependent on the substrate height  $h$  and conductor width  $W$ . For this equivalent model, effective permittivity  $\epsilon_e$  and characteristic impedance  $Z_0$  of the microstrip are obtained using quasi-static analysis. The effective dielectric constant ( $\epsilon_e$ ) of a microstrip line can be approximated as

$$\epsilon_e = \frac{\epsilon_r + 1}{2} + \frac{\epsilon_r - 1}{2} \frac{1}{\sqrt{1 + 12h/W}}. \quad (1.1)$$

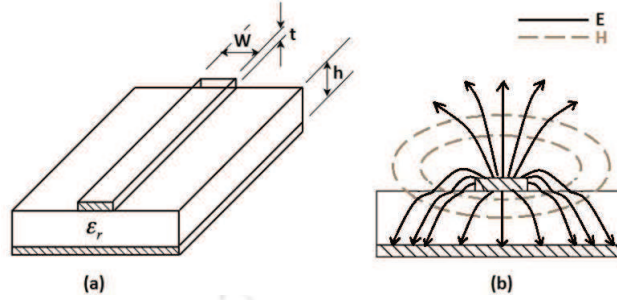


**Figure 1.1:** Microstrip line (a) Geometry and (b) Electric and magnetic field lines.

Once the effective dielectric constant of a microstrip line is determined, the guided wavelength ( $\lambda_g$ ) of the quasi-TEM mode of microstrip is given [2] by

$$\lambda_g = \frac{\lambda_0}{\sqrt{\epsilon_e}} = \frac{c}{f_0 \sqrt{\epsilon_e}} \quad (1.2)$$

where  $\lambda_0$  is the free space wavelength at the operation frequency  $f_0$  and  $c$  is the velocity of light in free space. The propagation constant ( $\beta$ ) and phase velocity ( $v_p$ ) can be determined as

$$\beta = \frac{2\pi}{\lambda_g} \quad (1.3)$$

$$v_p = \frac{\omega}{\beta} = \frac{c}{\sqrt{\epsilon_e}} \quad (1.4)$$

For given dimensions of the microstrip line, the characteristic impedance can be calculated from [2] as

$$Z_0 = \begin{cases} \frac{60}{\sqrt{\epsilon_e}} \ln \left( \frac{8h}{W} + \frac{W}{4h} \right) & \text{for } \frac{W}{h} \leq 1 \\ \frac{120\pi}{\sqrt{\epsilon_e} [W/h + 1.393 + 0.667 \ln(W/h + 1.444)]} & \text{for } \frac{W}{h} \geq 1. \end{cases} \quad (1.5)$$

If the characteristic impedance  $Z_0$  and the dielectric constant  $\epsilon_r$  are known, the expression for  $W/h$  in terms of  $Z_0$  and  $\epsilon_r$  can be expressed [2] as

$$\frac{W}{h} = \begin{cases} \frac{8e^A}{e^{2A}-2} & \text{for } \frac{W}{h} < 2 \\ \frac{2}{\pi} \left[ B - 1 - \ln(2B - 1) + \frac{\epsilon_r - 1}{2\epsilon_r} \left\{ \ln(B - 1) + 0.39 - \frac{0.61}{\epsilon_r} \right\} \right] & \text{for } \frac{W}{h} > 2 \end{cases} \quad (1.6)$$

where

$$A = \frac{Z_0}{60} \sqrt{\frac{\epsilon_r + 1}{2}} + \frac{\epsilon_r - 1}{\epsilon_r + 1} \left( 0.23 + \frac{0.11}{\epsilon_r} \right) \quad (1.7)$$

$$B = \frac{377\pi}{2Z_0 \sqrt{\epsilon_r}}.$$

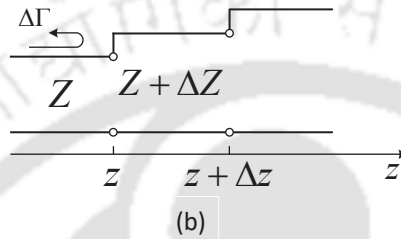
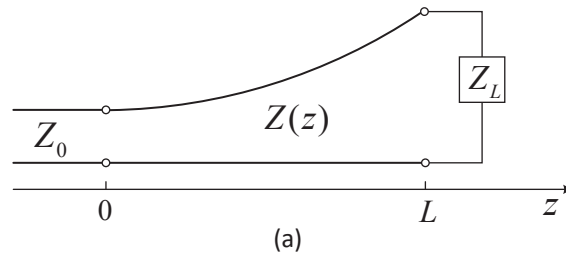


**Figure 1.2:** A tapered transmission line and the model for an incremental length of the tapered line (a) Continuously tapered transmission line and (b) Model for an incremental step change in impedance of the tapered line.

## 1.2 Introduction to tapers

Two transmission lines of different characteristic impedances can be matched over the desired bandwidth by using multisection quarter-wave transformers. However, its length would be larger if a higher matching bandwidth is required. As the number of  $N$  discrete sections increases, the step changes in characteristic impedance between the two sections becomes smaller. Thus, for  $N \rightarrow \infty$ , we approach to a continuously tapered line, as shown in Figure 1.2(a). For a finite and shorter length, it is always being preferred to use a tapered line so that a smooth impedance and field matching between two transmission lines of different characteristic impedances can be achieved over a very large bandwidth. We will see that different passband characteristics can be obtained by changing the type of tapers.

The continuously tapered line, as shown in Figure 1.2(a), can be considered to be made up of a number of small incremental length  $\Delta z$ , with a change in impedance of  $\Delta Z(z)$  from one section to the next, as shown in Figure 1.2(b). Then, the step change  $\Delta Z(z)$  in impedance at  $z$  produces an incremental reflection coefficient given by

$$\Delta\Gamma = \frac{(Z + \Delta Z) - Z}{(Z + \Delta Z) + Z} \simeq \frac{\Delta Z}{2Z} \quad (1.8)$$

As the limit  $\Delta z \rightarrow 0$ , we can get the differential reflection coefficient as

$$d\Gamma = \frac{dZ}{2Z} = \frac{1}{2} \frac{d}{dz} \left\{ \ln \left( \frac{Z}{Z_0} \right) \right\} dz. \quad (1.9)$$

By using the theory of small reflections [2], the total reflection coefficient at  $z = 0$  can be computed by summing up all the partial reflections with their appropriate phase shifts as

$$\Gamma(\theta) = \frac{1}{2} \int_0^L e^{-j2\beta z} \frac{d}{dz} \left\{ \ln \left( \frac{Z}{Z_0} \right) \right\} dz \quad (1.10)$$

where  $\theta = 2\beta l$ , is the electrical length and  $L$  is the total length of taper. So if impedance profile  $Z(z)$  is known,  $\Gamma(\theta)$  can be readily evaluated as a function of frequency. Alternatively, if  $\Gamma(\theta)$  is specified, then in principle  $Z(z)$  can be obtained, but this procedure is very difficult and generally avoided [3,4]. Now, we will discuss three different kinds of tapers: exponential, triangular and Klopfenstein taper, whose impedance profile  $Z(z)$  is known, and the resulting responses are evaluated.

### 1.2.1 Exponential taper

For an exponential taper, the impedance variation  $Z(z)$  can be expressed as

$$Z(z) = Z_0 e^{az} \quad \text{for } 0 < z < L. \quad (1.11)$$

At  $z = 0$ ,  $Z(0) = Z_0$  and at  $z = L$ ,  $Z(L) = Z_L = Z_0 e^{aL}$ , so the constant  $a$  can be determined as

$$a = \frac{1}{L} \ln \left( \frac{Z_L}{Z_0} \right). \quad (1.12)$$

Now, the reflection coefficient response  $\Gamma(\theta)$  for exponential taper can be obtained from (1.10) as

$$\begin{aligned} \Gamma(\theta) &= \frac{1}{2} \int_0^L e^{-j2\beta z} \frac{d}{dz} \left\{ \ln \left( \frac{Z_0 e^{az}}{Z_0} \right) \right\} dz \\ &= \frac{1}{2L} \ln \left( \frac{Z_L}{Z_0} \right) \int_0^L e^{-j2\beta z} dz \\ &= \frac{1}{2} \ln \left( \frac{Z_L}{Z_0} \right) e^{-j\beta L} \frac{\sin \beta L}{\beta L}. \end{aligned} \quad (1.13)$$

In the above derivation, it has been assumed that the propagation constant ( $\beta$ ) of the tapered line is constant along the line, which is an assumption generally valid only for TEM lines.

## 1. Introduction

---

### 1.2.2 Triangular taper

For a triangular taper, the differential term  $\frac{d}{dz} \ln \left( \frac{Z}{Z_0} \right)$  is a triangular function of  $z$ , and  $Z(z)$  is expressed as

$$Z(z) = \begin{cases} Z_0 e^{2(z/L)^2 \ln(Z_L/Z_0)} & \text{for } 0 \leq z \leq L/2 \\ Z_0 e^{(4z/L - 2z^2/L^2 - 1) \ln(Z_L/Z_0)} & \text{for } L/2 \leq z \leq L. \end{cases} \quad (1.14)$$

So that

$$\frac{d}{dz} \ln \left( \frac{Z}{Z_0} \right) = \begin{cases} \frac{4z}{L^2} \ln \left( \frac{Z_L}{Z_0} \right) & \text{for } 0 \leq z \leq L/2 \\ \left( \frac{4}{L} - \frac{4z}{L^2} \right) \ln \left( \frac{Z_L}{Z_0} \right) & \text{for } L/2 \leq z \leq L. \end{cases} \quad (1.15)$$

Substituting (1.15) in (1.10), and integrating, we get the reflection coefficient response  $\Gamma(\theta)$  for triangular taper as

$$\Gamma(\theta) = \frac{1}{2} \ln \left( \frac{Z_L}{Z_0} \right) e^{-j\beta L} \left[ \frac{\sin(\beta L/2)}{\beta L/2} \right]^2. \quad (1.16)$$

### 1.2.3 Klopfenstein taper

For a given taper length, the Klopfenstein impedance taper [4, 5] has been proved to be optimum due to the minimum reflection coefficient over the passband. Alternatively, for a maximum reflection coefficient specification in the passband, the Klopfenstein taper yields the shortest length of matching section. This taper is derived from a stepped Chebyshev transformer as the number of sections increases to infinity. The logarithm of the characteristic impedance variation of the Klopfenstein taper is given by [2]

$$\ln(Z(z)) = \frac{1}{2} \ln(Z_L Z_0) + \frac{\Gamma_0}{\cosh A} A^2 \phi \left( \frac{2z}{L} - 1, A \right) \quad \text{for } 0 \leq z \leq L \quad (1.17)$$

where the function  $\phi(x, A)$  is defined as

$$\phi(x, A) = -\phi(-x, A) = \int_0^x \frac{I_1 \left( A \sqrt{1 - y^2} \right)}{A \sqrt{1 - y^2}} dy \quad \text{for } |x| \leq 1 \quad (1.18)$$

where  $I_1(x)$  is the modified Bessel function. A very simple and effective method for finding the values of  $\phi(x, A)$  is presented in [6].

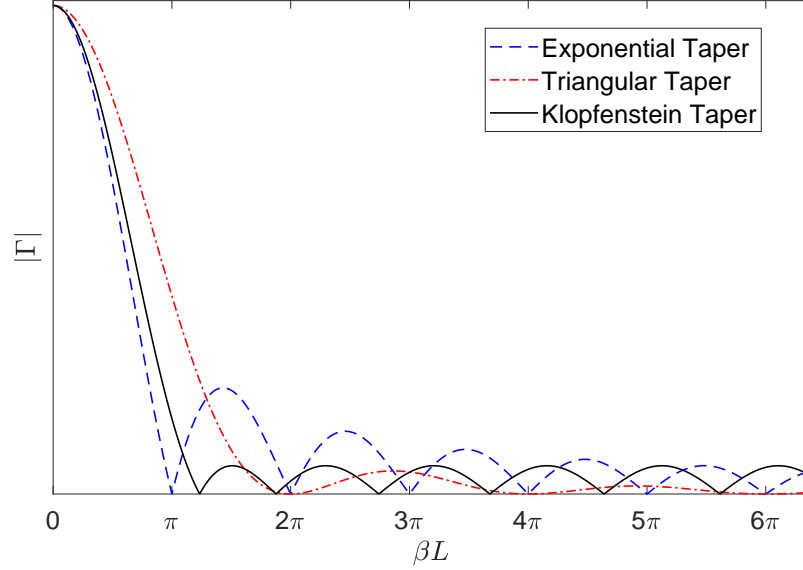


**Figure 1.3:** Reflection coefficient magnitude response for the different tapers.

The resulting reflection coefficient of Klopfenstein taper is given by [2]

$$\Gamma(\theta) = \Gamma_0 e^{-j\beta L} \frac{\cos \sqrt{(\beta L)^2 - A^2}}{\cosh A} \quad \text{for } \beta L > A. \quad (1.19)$$

If  $\beta L < A$ , the  $\cos \sqrt{(\beta L)^2 - A^2}$  term becomes  $\cosh \sqrt{A^2 - (\beta L)^2}$ .  $\Gamma_0$  is the reflection coefficient at zero frequency, which is given as

$$\Gamma_0 = \frac{Z_L - Z_0}{Z_L + Z_0} \simeq \frac{1}{2} \ln \left( \frac{Z_L}{Z_0} \right). \quad (1.20)$$

The passband is defined as  $\beta L \geq A$ , and so the maximum ripple in the passband is

$$\Gamma_m = \frac{\Gamma_0}{\cosh A} \quad (1.21)$$

because  $\Gamma_0$  oscillates between  $\pm \frac{\Gamma_0}{\cosh A}$  for  $\beta L > A$ . The disadvantage of this taper is that it has steps at  $z = 0$  and  $L$  (the ends of the tapered section), and so does not connect the source and load impedances smoothly.

The resulting reflection coefficient magnitude responses (versus  $\beta L$  or frequency) for exponential, triangular and Klopfenstein taper are plotted in Figure 1.3. It can be noted that the peaks in  $|\Gamma|$  decrease with increasing length in case of exponential and triangular tapers, while it is set to be constant for the desired passband of the Klopfenstein taper. A better matching at lower frequencies

can be achieved by increasing the length of the taper, but at the same time length of the matching section would become longer. The peaks of the triangular taper are lower than the corresponding peaks of the exponential case, but the first null for the triangular taper occurs at  $\beta L = 2\pi$ , whereas for the exponential taper it occurs at  $\beta L = \pi$ . It implies that at lower frequencies, the exponential tapers will have better passband than a triangular taper. For the given condition (say,  $\Gamma_m = 0.02$ ), the Klopfenstein taper provides better passband than the other two tapers, but its design consists of modified Bessel function which is very complicated to design practically and also it has step discontinuities at the junctions  $z = 0$  and  $L$  (the ends of the tapered section). It can also be noted that like the stepped-Chebyshev matching transformer, the response of the Klopfenstein taper has equal-ripple lobes versus frequency in its passband.

### 1.3 Microwave passive devices

Microwave passive devices and components are the essential building blocks of microwave circuits and systems that operate in the frequency range from 300 MHz to 300 GHz (corresponding to wavelengths of 1 m to 1 mm in free space). These devices will split, combine, filter, attenuate, and/or shift the phase of a microwave signal as it propagates through a particular transmission system. Microwave filters, power dividers and antennas will be briefly discussed here.

#### 1.3.1 Filters

A microwave filter is a two-port network used to control the frequency response at a certain point in a microwave system by providing transmission within the passband of the filter and attenuation in the stopband of the filter. The applications of filters can be found in almost every type of microwave communication, test and measurement system, and radar. In the late 1930s, image parameter method was developed to design low-frequency filters for radio and telephone applications. This method consists of cascaded two-port filter sections to achieve the desired cutoff frequencies and attenuation characteristics, but do not provide the specification of the response over the complete operating frequency range. Thus, even being a relatively simple procedure, designing the filters using image parameter method often need to be iterated many times to achieve the desired results.

The majority of modern microwave filters are designed by using the insertion-loss method, whereby the amplitude response of the filter is approximated by using network synthesis techniques that have been extended to accommodate microwave distributed circuit elements. A general four-step procedure

is followed for all pole: determination of filter specifications, design of a low-pass prototype filter, scaling and transforming the filter, and implementation (conversion of lumped elements to distributed elements consisting of transmission line sections). The subject of microwave filters is quite extensive, due to their importance in various practical systems and a numerous designs are carried out using advanced computer-aided design (CAD) tools such as full-wave electromagnetic (EM) simulators and advanced network synthesis techniques.

### Filter parameters definition

The fundamental specifications for designing filters are frequency range, bandwidth, insertion loss, return loss, stopband attenuation and frequencies, roll-off rate, input and output feedline impedances, voltage standing-wave ratio (VSWR), phase linearity, group delay, temperature range, and transient response. The input of a filter is driven by a signal generator with the output passing to a load. At the input plane of the filter, the power may be broken down into three components:

$P_{in}$  → the incident power from the generator,

$P_R$  → the power reflected back to the generator and

$P_L$  → the power passed on to the load.

### Insertion loss

The insertion loss (IL) (in decibels) is the ratio of incident power to the transmitted power

$$IL = 10 \log(P_{in}/P_L) = -10 \log(|\Gamma|^2) = -20 \log(|S_{21}|) \quad (1.22)$$

### Return loss

Three related parameters, the return loss (RL), VSWR, and reflection coefficient ( $\Gamma$ ), are commonly used to characterize filter reflections. The return loss is the ratio of incident power to the reflected power (in dB)

$$RL = 10 \log(P_{in}/P_R) = -10 \log\left(\frac{VSWR - 1}{VSWR + 1}\right)^2 = -10 \log(|\Gamma|^2) = -20 \log(|S_{11}|) \quad (1.23)$$

where  $\Gamma$  is the reflection coefficient.

### Types of filters and their applications

Basically there are four types of filters: low-pass, high-pass, bandpass and band-stop (also called band-

## 1. Introduction

---

reject). An ideal filter would have zero insertion loss in the passband, constant group delay or linear phase response in the passband, and infinite attenuation in the stopband. But in practice, all filters exhibit spurious responses where they have some rejection in the passband and finite transmission in the stopband. It is best described by the filter performances over the frequencies of interest. Over the past two decades, the explosive growth in wireless communication employing portable devices has generated a significant market for compact size, lower cost, lesser loss, and light weight filters. Various technologies such as monolithic microwave integrated circuits (MMIC), micromachining, microelectromechanic system (MEMS), high-temperature superconductor (HTS) and low-temperature cofired ceramics (LTCC) are being used to meet stringent requirements for RF/microwave filters. Furthermore, the incorporation of other active and passive devices in filter circuits, results in rapid development of microwave filters. Almost all microwave receivers, transmitters, and test setups require filtering action. The main filter functions are to reject undesirable signal frequencies outside the filter passband and to channelize or combine different frequency signals. Good examples for the former applications are mixers (low pass) and multipliers (bandpass). A well-described example for the latter application is the channelized receiver in which a bank of filters is used to separate input signals. Specific applications include electronic support measure (ESM) receivers, satellite communications, mobile communications, metrology, radar, remote sensing systems, pulse code modulation (PCM) communications, and microwave FM multiplexers.

### 1.3.2 Power dividers

A power divider (or, splitter) is a passive microwave component which divides the power of input signal into two or more output signals of lesser power. Since power divider is a reciprocal network, they can also be used as a power combiner, where two (or more) ports are used to combine input signals into a single output port. Power dividers are used in microwave frequencies because usually we have only one microwave source and we need to input this single source to many microwave devices in a microwave device network. Similarly, we require power combiners to combine the power from many microwave devices to the single output port in many practical applications. They are widely used in mixers, antenna array feed networks, phase shifters, power amplifiers, and vector modulators [2].

#### Basic properties of power dividers

A power divider is a three-port network which can be characterized using the following properties:

[TH-2274\\_146102015](#)

- Reciprocal → A passive component with no anisotropic materials must be a reciprocal network.
- Lossless → To avoid power loss, we aim to have a lossless network.
- Matching → All ports should be matched to avoid reflection from the ports.
- Isolation → The output ports should be isolated so that any unwanted signal coming from one output port should not go to the other output lines.

However, it is impossible to design a power divider which is lossless, reciprocal and matched at all ports simultaneously. By relaxing any of these conditions, different types of power dividers can be realized.

### Types of power dividers

Following three are the main types of power dividers:

- (1) **Lossless T-junction power divider:** It is a simple three-port network which satisfies the basic purpose of dividing an input signal into two separate transmission paths without any line loss. But it suffers with two main problems: no isolation between the output ports and can not be matched all the ports simultaneously.
- (2) **Lossy (resistive) T-junction power divider:** The T-junction power divider can be matched at all the ports by using lossy (resistive) components. The resistive power dividers are simple and broadband but lossy due to the resistors which absorb power. They have lesser power handling capability and higher insertion loss, which make them unsuitable for use in many types of systems. Also, they do not provide isolation between the output ports [7].
- (3) **Wilkinson power divider:** The Wilkinson power divider [8] is the most popular kind of power divider because it is easy to construct and it satisfies almost every properties of three-port network: (i) it is a reciprocal network, (ii) lossless when the output ports are matched that means only reflected power is dissipated, (iii) all the ports can be matched, and (iv) isolation between the output ports can be achieved using isolation resistor. In this power divider, there are four different sections namely: input port, quarter-wave transformer, isolation resistor, and output ports. The quarter-wave transformers are used to split the input signal into two output signals that are in phase with each other. The isolation resistor between the two output ports enables the two outputs to be matched and isolated as well. The Wilkinson power divider can be configured as N-way device, although it's primarily used for 2-way power division. Both equal

## 1. Introduction

---

and unequal split Wilkinson power dividers are possible to design. Stepped multiple sections or tapered sections can be employed for increasing the bandwidth of the power divider.

Regardless of the type of power divider, the goal of every power divider is to have the highest port-to-port isolation, lowest insertion loss and VSWR, and minimum amplitude and phase imbalance over the entire operating frequency range of the device.

### 1.3.3 Antennas

Antenna is one of the most important building blocks of a wireless communication system. It can be defined as a transducer which converts electrical signal into electromagnetic wave radiation or vice-versa. An antenna can also be viewed as a device used in matching the impedance of a transmission line or waveguide to the impedance of free space medium or vice-versa. The types of antennas can be classified based on their specifications like frequency, polarization, radiation, etc. There are various types of microwave antennas being developed over the years for different applications, including communication based applications. Microstrip patch antenna is one of the most common and popular types of microwave antenna, due to its easier fabrication, thin planar profile, simple structure, light weight, lower cost, and easier integration with other active and passive circuits on the same circuit board. It can be mounted on rigid surfaces of high-performance spacecraft, satellites, aircraft, missiles, cars and hand-held mobile phones. A microstrip patch antenna consists of a radiating patch on one side of the substrate, with a ground plane on the other side of the substrate.

#### Antenna parameters

Every antenna has some parameters that signify its characteristics and efficient realization. Typical antenna parameters are radiation pattern, bandwidth, directivity, gain, radiation efficiency, beamwidth, radiation resistance and polarization.

#### Radiation pattern

Radiation pattern of an antenna is defined as a graphical representation of its radiation properties as a function of space coordinates at the far-field. It can be magnitude of field patterns or power patterns. The patterns are oftenly normalized with respect to their maximum value. The radiation pattern of an antenna can be [9]:

- Isotropic: A hypothetical lossless antenna having equal radiation in all directions.

- Omnidirectional: An antenna having an essentially non-directional pattern in a given plane (e.g., in azimuth) and a directional pattern in any orthogonal plane.
- Directional: An antenna having the property of radiating or receiving more effectively in some directions than in others. Usually the maximum directivity is significantly greater than that of a half-wave dipole.

### Directivity, gain and efficiency

The directivity of an antenna is defined as the ratio of the radiation intensity in a given direction from the antenna to the radiation intensity averaged over all directions. Gain is the ratio of radiation intensity in a given direction to the average radiation intensity that would be obtained if all the power input to the antenna were radiated isotropically. Directivity only measures directional properties while gain accounts the efficiency of the antenna as well. The gain of the antenna can also be expressed as the product of the antenna radiation efficiency and its directivity.

### Polarization

Polarization is the curve traced by the end point of the arrow (vector) representing the instantaneous electric field. The field must be observed along the direction of propagation. Polarization is classified as linear, circular, or elliptical. If the vector that describes the electric field at a point in space as a function of time is always directed along a line, the field is said to be linearly polarized. Linear polarization and circular polarization are special cases of elliptic polarization. The figure of the electric field traced in a clockwise rotation is designated as right-hand polarization and counter clockwise as left-hand polarization.

## 1.4 Research background and motivation

A quarter-wave transformer can match any real load impedance to any impedance of the line at the design frequency. Based on the theory of small reflections [3, 10], binomial and Chebyshev multisection transformers [2, 11] are developed for the applications requiring more bandwidth than a single quarter-wave transformer. These multi-stepped sections can be transformed into a continuously tapered transmission line by increasing the number of sections and decreasing the step changes in characteristic impedance between the sections. A smooth impedance and field transition between the two transmission lines of different characteristic impedances can be achieved over a very large

## 1. Introduction

---

bandwidth by using tapered lines of shorter length than the corresponding length of multisection quarter-wave transformers [2]. It is found that different passband characteristics can be obtained by changing the type of tapers like exponential, triangular, and Klopfenstein taper [2–5]. The nonuniform or tapered transmission lines can be efficiently used in the design of passive microwave components like resonators [12–14], filters [13,15–17], power dividers [18–22], and as a feed line in antennas [23–26]. An efficient technique for analyzing an arbitrary nonuniform transmission line with piecewise-linear approximation of the characteristic impedance profile of the line has been presented in [27] and a simplified analytical CAD model for linearly tapered microstrip line including losses has been developed in [28]. Further, an analytical approach for analysis of nonuniform transmission line and tapered microstrips using differential transfer matrix method has been proposed in [29].

Since the U.S. Federal Communications Commission (FCC) released the unlicensed use of the ultra-wideband (UWB) spectrum (3.1-10.6 GHz) for indoor and hand-held devices in early 2002 [30], a lot of research activities and interests have been shown in academic and industrial circles toward exploring various UWB components and devices [31]. A wideband or UWB communication has large operational bandwidth enabling high-speed data rate transfer for short-range wireless connections as well as applications in long range, low data rate, radar, and imaging systems [32]. There are some well-known techniques that have been presented in [33–37] to design wideband microwave filters, where fractional bandwidth (FBW) up to 60~80% have been achieved. Several methods have been reported in [38–51] to design UWB bandpass filters. The method presented in [38] is based on cascaded low-pass-high-pass filter sections. The concept of multiple-mode resonator (MMR) was proposed initially in [36] and based on that, UWB filters were developed in [39–45]. A design method based on network analysis and optimization in Z-domain has been employed in [46,47]. An UWB microstrip filter with an optimum FBW of greater than 120% is presented in [48] which is based on non-redundant unit elements or connecting lines. In [50], a coupled double-stepped structure and an open-loop defected ground structure (DGS) on the ground has been employed for achieving UWB bandwidth along with a wide stopband attenuation. In [49], UWB filters utilize broadside coupling between elliptical-shaped microstrip patches at the top and bottom layer of the filter's structure via an elliptical slot located at the mid layer, which contains the ground plane. A method to design microstrip bandpass filters with UWB performance, where three subsections of different lengths and coupling factors are connected to form a stepped-impedance parallel-coupled microstrip structure, is presented in [51]. To suppress

the interference to certain frequency bands like wireless local area network (WLAN) operating at 5.5 GHz in UWB region, many efforts have been put forward to design notched-band UWB filters [52–58]. A meander line slot [52], embedded open-circuited stubs [53], embedded open stubs with U-shaped DGS structure [54], complementary single split ring resonator (CSSRR) in the ground plane [55], and spurline structure in the main line [56] have been employed to produce the notch-band around 5.5 GHz. Notched band-stop filtering effect is achieved in [57] by adding coupling interdigital finger to reject the undesired WLAN radio signals. A spiral slot is introduced in [58] to achieve narrow notched band characteristics in the UWB region.

Based on tapered lines, an ultra-broadband equal split Wilkinson-type power divider has been designed in [19] which covers the whole UWB communication band. A broadband multisection Wilkinson power divider with arbitrary power split ratio is presented in [59]. The disadvantage of Wilkinson dividers is that they require an additional component selection like a resistor. An UWB power divider for spatial power combining has been proposed in [20], which comprised of a tapered transmission line and 1-to-2 power dividers to realize a 1-to-4 power-dividing function. The T-junction power dividers with prescribed response characteristics have been presented in [18, 60–63], which can be used as an equal or unequal, narrowband and broadband T junction circuits. In many cases, T-junction power dividers are preferred to be used as an unequal power division where most of the power is desired in one of the output port and least power in the other output port over a very broad frequency range [18, 21, 22]. In [18], different empirical models have been employed to realize three distinct geometrical configurations, but they do not provide much physical insight about the device operation. An analytical method has been developed in [21] to find the port parameters of exponentially tapered broadband T-junction power divider. However, the cut-off wavelength definition adopted in [21] is incorrect and the analysis with correction has been presented in [22].

In early 1985, *Pozar* [64] introduced a new technique to feed microstrip patch antennas which do not require a direct connection between the antenna and feedline. The method involves two substrates separated with a common ground plane, where one substrate contains the radiating patch and the other substrate containing the feed network, with a small aperture in the ground plane, located under the patch. The analysis of this method has been further carried-out in [65–68]. Based on this method, a dual aperture coupled circularly polarized (dual polarised) patch antenna [69] and a dual slot-coupled microstrip antenna for dual frequency operation [70] have been developed. Various

## 1. Introduction

---

techniques are being evolved over time for designing high isolation dual-polarized antennas [71–74] for narrowband and broadband applications. Dual-port dual-polarized antennas with high isolation and low cross polarization are proposed in [75–78] for full-duplex 2.4 GHz ISM band applications. A two-element monopole array excited by a  $180^\circ$  hybrid feeding network and an antenna system operating at 2.4 GHz WLAN band is presented in [79] for in-band full-duplex applications. Based on combined edge/aperture feeding method, dual-polarized (orthogonal polarized) microstrip-patch planar array antennas with high port-to-port isolation have been developed in [80,81]. A coax-feed dual-polarised patch antenna with low cross-polarisation and high port-to-port isolation is presented in [82] for WiMAX applications. A printed monopole antenna with a protruding stub in the ground plane [83] and an asymmetric coplanar strip (ACS)-fed dual-band antenna using loaded capacitance terminations [84] have been proposed for dual-band 2.4/5.8 GHz WLAN and RFID applications.

In 2001, K. Wu *et al.* invented substrate integrated waveguide (SIW), a new type of transmission line (TL) which has the merits of both metallic rectangular waveguide and planar transmission line [85–87], like low insertion loss, low radiation loss, planar structure and compact size. SIW technology has emerged as a very promising candidate for the development of microwave and millimeter-wave circuits and antennas [88–93]. A taper transition between SIW and microstrip line is presented in [85] for the first time and later, its design equations have been developed in [91,94]. Spoof surface plasmon polariton (SSPP), a plasmonic metamaterial sub-wavelength structure exhibiting slow-wave characteristics has been employed in SIW to design bandpass filters with a very high level of attenuation in the stopband. This concept of designing broadband bandpass filters using the low-pass characteristics of SSPP and high-pass characteristics of SIW termed as hybrid SSPP-SIW filters [1,95–100]. The first hybrid SSPP-SIW filter was proposed in [95], where the SSPPs structure were connected in series with SIW section. Since, the two structures are separated, resulting in a larger size, and the conversion of the fields add more complication as well. In [96], a hybrid SSPP-SIW transmission line for designing broadband BPFs have been proposed, where SSPPs propagate through arrays of transverse metallic blind holes that were designed inside the SIW. Although, it requires a thicker substrate to achieve larger slow-wave characteristics, and hence not a right choice for compact circuit applications. A planar bandpass filter based on a hybrid SSPP-SIW transmission line is presented in [97], but only simulation results have been shown. Hybrid HMSIW-SSPP structures have been proposed in [98,99], which overcome shortcomings of large size. However, their transmission characteristics further need

to be improved. Also, none of the above hybrid SSPP-SIW filters considers out-of-band rejection. A broadband BPF using hybrid SSPP-SIW structure has been proposed in [1], which showed broad out-of-band rejection but suffered from poor in-band performances. Recently, a bandpass filter based on half-mode SIW and double-layer SSPPs has been developed [100], which features wider bandwidth, smaller size and lower loss than previously reported structures.

In the above reported literature, further investigation needs to be carried out to miniaturize the size and improve the performances of microwave passive devices, which can be achieved by employing tapers, SIW and SSPP structures. In the modern time of ever expanding wireless and consumer electronics market, it is highly desirable to integrate number of circuits in a single board, and hence there is much demand for size reduction and high performance circuits. The main findings and motivation behind carrying this research work are as follows:

- By choosing the type of tapers, one can obtain the desired reflection coefficient response by setting the frequency above which there will be least reflections in the whole desired band for varied length of the taper, or the length of taper can be made to be fixed and accordingly the response can be obtained by varying frequency, see Figure 1.3. So broadband and highly efficient impedance matching networks, resonators, filters, power dividers, etc. can be designed using tapers.
- In many literature, they have used triangular taper specifications and analysis, while designing the taper the width is varied linearly which is not actually a triangular taper rather a linear width taper whose theoretical characterization is not available in the literature. So the linear tapers, which are the most practically used type of taper, has been theoretically characterized in this work and using them, several microwave passive devices have been designed and analyzed.
- Synthesis of iris SIW filters lacks the design equation for finding the widths of iris windows, which were obtained by several simulations and optimizations using EM solvers. For that, a design process and an approximate design equation has been presented and well validated.
- Recently, slow-wave or low pass characteristics of SSPP employed along with high pass characteristics of SIW to design broadband bandpass filters with a very high level of attenuation in the stopband, but they suffer with poor inband performances and large structure. These issues can be solved using the proper field or mode transition structure. Linearly graded slots, which

produces gradient momentum and smooth transition of SIW mode to SSPP mode, and a novel SSPP structure showing higher slow-wave phenomena, have been proposed in this work.

### 1.5 Contribution of the thesis

This thesis aims at the novel design and analysis of various microwave passive devices (such as filters, power dividers and antenna) that are light weight, low cost, compact size, and improved performances for different microwave frequency band applications. The main contributions of the thesis are as follows:

- Using exponentially tapered impedance line stub loaded microstrip resonator, a notch function in the UWB bandpass filter is created for suppression of WLAN signals. An approximate theoretical analysis of the filter is also presented. The fabricated notched UWB bandpass filter is tested using vector network analyzer, which shows the desired notch filter characteristics.
- Linear tapers have been theoretically characterized, and their results are compared with the other tapers. By using linearly tapered microstrip line, a broadband taper transition between microstrip line and SIW component and a novel coupled-line ultra-broadband bandpass filter is designed, fabricated and tested. The filter possesses a very compact size of  $0.20\lambda_g \times 0.26\lambda_g$  and shows a wide 10 dB passband from 4.5 to 12 GHz.
- Unequal T-junction power dividers using linear tapers have been proposed, which exhibit the power dividing ratio of more than 10 dB over an ultra-broadband or even a SWB bandwidth. A method for theoretical analysis of the power dividers has also been developed. A prototype fabricated power divider is tested and well verified.
- A dual-port, aperture coupled and linearly tapered fed patch antenna with high isolation for full-duplex 2.4 GHz ISM band applications is designed, fabricated and tested.
- An approximate design equation for iris width calculation of iris SIW bandpass filter is presented. A filter at V-band is designed and validated the design equation. Two bandpass filters using the hybrid structure of SSPP, SIW and linear taper are designed for X-band applications. Dumbbell-shaped SSPP has been proposed which shows more slow-wave effects than rectangle-shaped SSPP for the same height of grooves. The proposed filters show very good passband and wide upper

out-of-band rejection simultaneously. They possess very compact size of  $\sim 1\lambda_g \times 0.7\lambda_g$ . Their length is only about a wavelength at the center frequency, which is much lesser than the length of existing hybrid SSPP-SIW filters. Both filters are fabricated and tested successfully.

## 1.6 Thesis organization

This thesis is organized into seven chapters. The summary of each chapter is briefly outlined as follows:

- **Chapter 1:** This chapter presents an introduction to microstrip line and tapered lines. It also covers the brief background and literature review of microwave passive devices and antenna. Thereafter, motivation and contribution of the thesis are presented.
- **Chapter 2:** In this chapter, we have proposed two UWB filters, one without notch band and the other with notch band using exponentially tapered impedance line stub loaded microstrip resonator. Their approximate theoretical analysis has also been presented. The simulated results are in good agreement with the analytical and measured results.
- **Chapter 3:** This chapter presents the theoretical characterization of linear tapers and their comparison with the other tapers. By using linearly tapered microstrip lines, a broadband taper transition between the microstrip line and SIW component and a coupled-line ultra-broadband bandpass filter is designed, fabricated and tested.
- **Chapter 4:** This chapter provides an ultra-broadband T-junction power divider using linearly tapered microstrip lines. A method for theoretical analysis of the power divider has been presented approximately. The theoretical, simulated and measured results are presented. Also, a super wideband power divider is designed by following the proposed method.
- **Chapter 5:** This chapter proposes a dual-port, aperture coupled and linearly tapered fed patch antenna with high isolation for full-duplex 2.4 GHz ISM band applications. The designed antenna is simulated, fabricated and measured.
- **Chapter 6:** This chapter presents the approximate design equation for iris width calculation of iris SIW bandpass filter. By using the proposed equation, an iris SIW bandpass filter has been designed and validated for V-band applications. Also, two bandpass filters using the hybrid

## 1. Introduction

---

structure of SSPP, SIW and linear taper have been developed for X-band applications. Both filters have been designed, fabricated and tested successfully.

- **Chapter 7:** This chapter concludes the research work of the thesis and discusses some scope for future research works.



# 2

## Notched UWB filter using ETILSLMR

### Contents

2.1	Introduction . . . . .	22
2.2	Initial UWB filter design . . . . .	24
2.3	Notched-band UWB filter design . . . . .	28
2.4	Comparison with measured results . . . . .	34
2.5	Summary . . . . .	37

In this chapter, two ultra-wideband (UWB) filters, one without notch band and the other with notch band, with a fractional bandwidth (FBW) of more than 120% have been proposed. The first filter is designed with three quarter wavelength short-circuited stubs and the second filter is designed by using exponentially tapered impedance line stub loaded microstrip resonator (ETILSLMR). The first filter consists of five transmission poles within the passband. The second filter with tapered inductive loading on quarter-wavelength high impedance line exhibits a sharp notch stopband around 5.5 GHz, to suppress the interference from IEEE 802.11a WLAN band signals with an attenuation level higher than 30 dB.

### 2.1 Introduction

A wideband or an UWB bandpass filter with compact size, improved selectivity, better passband and the least varying group delays is one of the main requirements to realize UWB and other radio communication systems. There are various well-known techniques to design wideband bandpass microwave filters [33–35, 48, 101]. Parallel-coupled line, hairpin-line, interdigital line and combline filters are traditional wideband bandpass filters, which are known for their low cost and simple fabrication process [33]. The half-wavelength line resonators in parallel-coupled (or, edge-coupled) filters are positioned so that adjacent resonators are parallel to each other along half of their length, which gives relatively more coupling for a given spacing between resonators and hence wider bandwidth than end-coupled half-wavelength resonator based microstrip filters. To make the structures more compact, the resonators of parallel-coupled half-wavelength resonator filters have been folded in U-shape, which are so-called as hairpin type resonators. Interdigital bandpass filter consists of an array of quarter-wavelength line resonators, which are short-circuited at one end and open-circuited at the other end with alternative orientation. This type of microstrip bandpass filter is relatively compact but requires via-holes groundings. However, the second passband of such filter is centered at about three times the center frequency of the first passband, while for the filters with parallel-coupled half-wavelength resonators, the spurious passband is centered at around twice of the midband frequency. The combline bandpass filter is comprised of an array of coupled resonators, which are short-circuited at one end and the other end loaded with a lumped capacitance between the resonator and ground plane. By increasing the loading capacitances, the length of resonators can be made shorter, and a wider stopband can be achieved between the first passband and the unwanted second passband. These

kind of filters have coupling gaps which would be very tight when a large FBW is desired, for example, greater than 50%. The tight coupling gaps have been greatly relaxed by opting parallel-coupled three-line microstrip structures [34,35], where wideband bandpass filters with FBWs from 40% to 70% are presented. In [101], wideband and small-sized ring filters with FBWs of more than 100% have been introduced. An UWB microstrip filter with an optimum FBW of greater than 120% is presented in [48] which is based on non-redundant unit elements or connecting lines. A comparison study has also been presented in [48], showing advantages of this type of filter over conventional design whose unit elements are redundant [33].

Nowadays, multiple-mode resonators (MMRs) are the most commonly known UWB filters which have become very popular due to their simple design, compact structure and easy fabrication. The original idea of an MMR was presented in [36] and based on this concept, an UWB bandpass filter was reported in [41] for the first time in which five transmission poles were realized using two-pole parallel-coupled lines and three-mode MMR. The work of [41] was utilised in [42] for designing an UWB filter with a better feasibility by using aperture on the backside ground plane, which improved the coupling between resonator and feeders. A MMR-based UWB BPF is proposed and implemented in [39] using the hybrid microstrip/CPW structures, where a CPW nonuniform or MMR is formed on the ground plane to excite and allocate the first three resonant modes occurring around the lower end, center and higher end of the concerned UWB passband. By forming a MMR on a CPW and two single microstrip-to-CPW coupling structures with enhanced degree, a compact UWB filter is designed in [40]. An improved class of UWB BPFs is presented in [43] by driving the MMR resonator with interdigital coupled lines of enhanced coupling degree. An improved microstrip-line UWB BPF is presented in [44] by forming an alternative MMR with proper loading of three open-ended stubs. In [45], an UWB filter is realized by using modified MMR method, formed by attaching three pairs of circular impedance-stepped stubs in shunt to a high impedance microstrip line. An UWB filter using a microstrip stepped-impedance four modes resonator is proposed in [46] by implementing network analysis theory and optimization in  $Z$ -domain, where six transmission poles are obtained in the passband with a very flat group delay and compact size. The same concept with a modified theory is employed in [47], where transmission zeros have been produced on both sides of the passband by shunting two section open-circuited stubs. In [50], a coupled double-stepped structure and an open-loop defected ground structure (DGS) on the ground has been employed for achieving UWB bandwidth along with

a wide stopband attenuation. In [49], UWB filters utilize broadside coupling between elliptical-shaped microstrip patches at the top and bottom layer of the filter's structure via an elliptical slot located at the mid layer, which contains the ground plane. A method to design microstrip bandpass filters with UWB performance, where three subsections of different lengths and coupling factors are connected to form a stepped-impedance parallel-coupled microstrip structure, is presented in [51].

In UWB region, there are several other narrowband radio signals, including wireless local area network (WLAN) which operate at 5.5 GHz. Therefore, a lot of attention has been paid to design single or multiple notched-band UWB filters [52–58, 102, 103]. To suppress the undesired WLAN radio signals, a meander line slot is employed in [52], and a narrow notched band is achieved in [53] by using embedded open-circuited stubs. In [54], embedded open stubs with U-shaped DGS structure are introduced to produce a notch characteristic in the desired frequency band. Notched UWB filters were designed using complementary single split ring resonator (CSSRR) in the ground plane [55] and spurline structure in the main line [56]. Notched band-stop filtering effect is achieved in [57] by adding coupling interdigital finger to reject the undesired WLAN radio signals. A dual-notched bands UWB bandpass filter based on a simplified composite right/left-handed (SCRLH) resonator and a triple-notched bands UWB bandpass filter using triple-mode stepped impedance resonator, are developed in [58] and [102] respectively. A microstrip bandpass UWB filter with three notch bands, using five short-circuited stubs and three U-shaped open-circuited stubs is proposed in [103].

In this work, we introduce an UWB filter with FBW of more than 120%, where a uniform  $50 \Omega$  transmission line is loaded with three identical and symmetrical quarter wavelength short-circuited (SC) stubs. To suppress WLAN radio signals in UWB region, we have developed a novel notched UWB filter using exponentially tapered impedance line stub loaded microstrip resonator (ETILSLMR). The sharp notch frequency at 5.5 GHz is obtained with the help of tapered inductive loading on the quarter wavelength high impedance lines. Two prototype filters, first without notch band and second with a notch stopband, are fabricated, and a good agreement is achieved between their measured and predicted results.

## 2.2 Initial UWB filter design

The configuration of the design with single quarter-wavelength SC stub is shown in Figure 2.1. By loading a high-impedance quarter-wavelength SC stub on the conventional  $50 \Omega$  transmission line, an

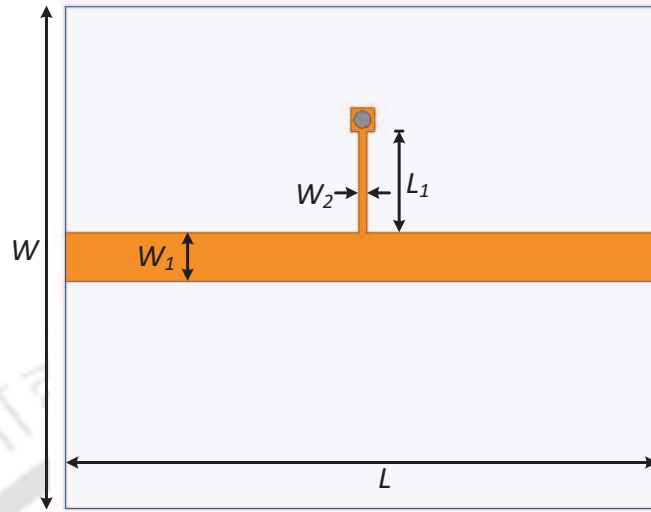


Figure 2.1: Configuration of the design with single SC stub.

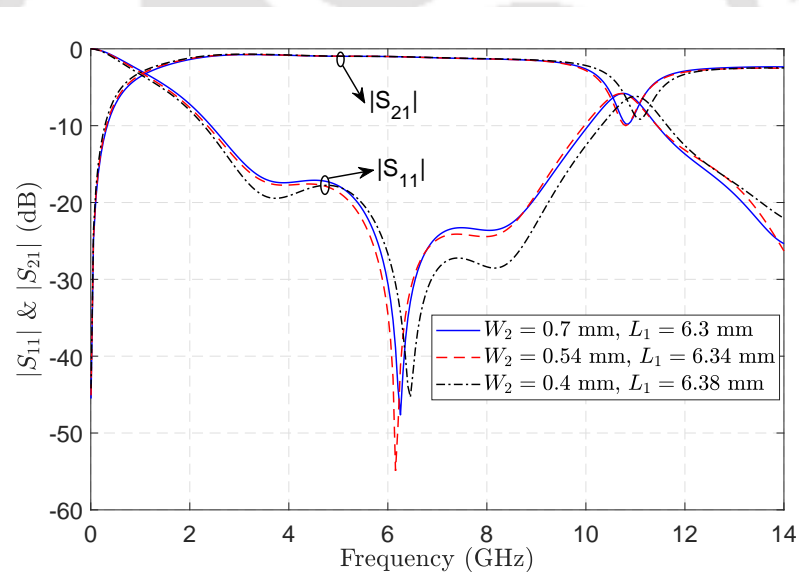


Figure 2.2: Simulated S-parameters of the design with single SC stub.

UWB bandwidth can be achieved, as shown in Figure 2.2. The results are plotted for  $100 \Omega$ ,  $110 \Omega$  and  $120 \Omega$  quarter-wavelength long SC stub, which is designed at the center frequency of  $6.85 \text{ GHz}$  using an FR4-epoxy substrate ( $\epsilon_r = 4.4$ ,  $\tan\delta = 0.02$ ,  $h = 1.6 \text{ mm}$ ). Since a quarter-wavelength SC line behaves as an open circuit at the other end, a signal will get transmitted from the one port to the other through the  $50 \Omega$  line without any disturbance from the stub loading and will have a resonance at the design frequency. Although, for the design with single stub has poor performances, which could be further improved by increasing the number of resonators or stubs. The schematic of initially

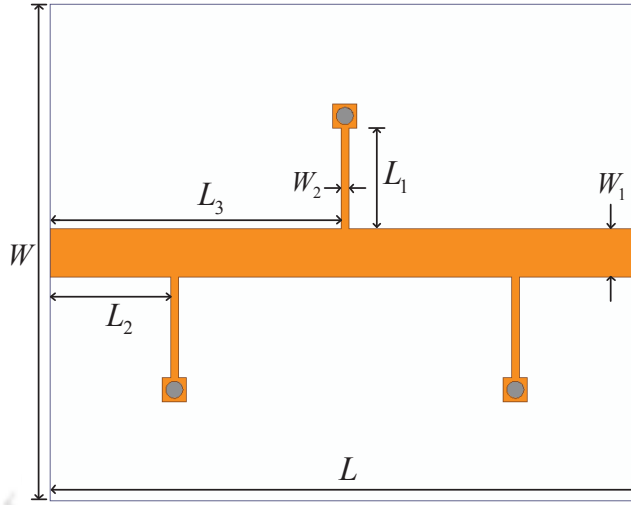


Figure 2.3: Schematic of the initial UWB filter design.

Table 2.1: Design parameter values for the initial UWB filter

$L = 38$ mm	$W = 32$ mm
$L_1 = 6.5$ mm	$W_1 = 3.1$ mm
$L_2 = 7.75$ mm	$W_2 = 0.5$ mm
$L_3 = 18.75$ mm	

designed UWB filter is shown in Figure 2.3. It consists of a uniform  $50 \Omega$  transmission line in the horizontal plane and three quarter-wavelength short-circuited stubs loaded in the vertical plane. One of the stubs is in the middle position of one side of  $50 \Omega$  transmission line and the other two, which are of the same dimensions, are at the symmetrical locations on the other side of transmission line. All the stubs are placed at a distance of about half wavelength apart from each-other to realize five transmission poles within the passband. Due to the same dimensions of each stub, two transmission zeros, one at the zero frequency and another in the upper stopband with higher selectivity has been achieved. The optimized design parameters for the proposed filter are provided in Table 2.1, and its simulated results obtained from HFSS software are shown in Figure 2.4. The passband for this UWB filter ranges from 2.6 GHz to 10.6 GHz with FBW of 121% at a center frequency of 6.6 GHz. It can be seen that S-magnitudes,  $|S_{21}| > -3$  dB and  $|S_{11}| < -10$  dB in the whole passband. The filters are designed on FR4-epoxy substrate ( $\epsilon_r = 4.4$ ,  $\tan\delta = 0.02$ ,  $h = 1.6$  mm). The diameter of each via-hole is 1.1 mm.

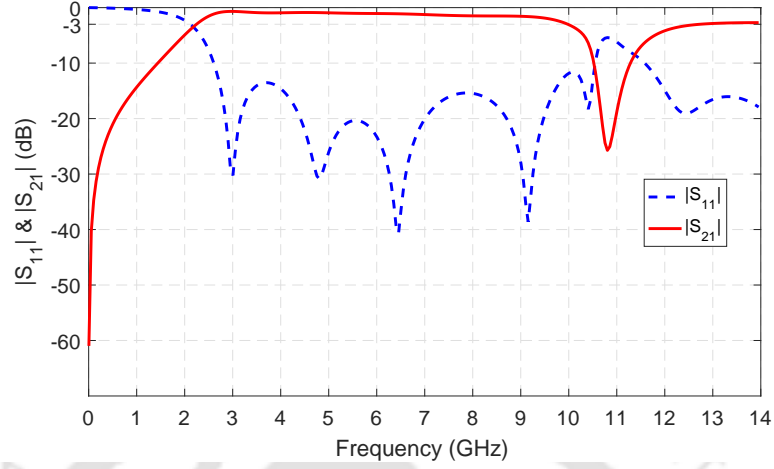


Figure 2.4: Simulated S-magnitudes of the initial UWB filter.

### 2.2.1 Theoretical analysis of proposed UWB filter

By using transmission line network analysis, an approximate theoretical analysis is performed for the UWB filter design. It is considered that transmission lines are lossless and ignores the effects of edge capacitances at the junctions, inductive effects at the short-circuited stubs and frequency dispersion. The overall ABCD matrix,  $[R]$  for the transmission line model in Figure 2.5, is obtained by multiplying the ABCD matrices of the terminal lines, shunt short-circuited stubs and connecting lines in sequence, i.e.

$$[R] = \begin{bmatrix} A & B \\ C & D \end{bmatrix} = [U][V][W][V][W][V][U] \quad (2.1)$$

where

$$[U] = \begin{bmatrix} \cos(\theta_0) & \frac{j \sin(\theta_0)}{Y_0} \\ jY_0 \sin(\theta_0) & \cos(\theta_0) \end{bmatrix} \quad (2.2)$$

$$[V] = \begin{bmatrix} 1 & 0 \\ \frac{Y_1}{j \tan(\theta_1)} & 1 \end{bmatrix} \quad (2.3)$$

$$[W] = \begin{bmatrix} \cos(\theta'_0) & \frac{j \sin(\theta'_0)}{Y_0} \\ jY_0 \sin(\theta'_0) & \cos(\theta'_0) \end{bmatrix} \quad (2.4)$$

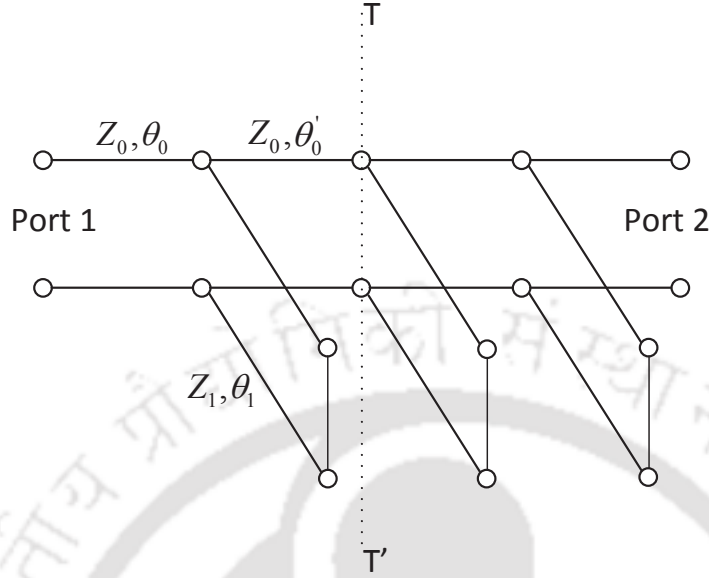


Figure 2.5: Equivalent configuration of the initial UWB filter.

Using the matched source and load condition with impedances,  $Z_0$ , the S parameters of the proposed model can be obtained from (2.1) as

$$S_{11} = \frac{A + \frac{B}{Z_0} - CZ_0 - D}{A + \frac{B}{Z_0} + CZ_0 + D} \quad (2.5)$$

$$S_{21} = \frac{2}{A + \frac{B}{Z_0} + CZ_0 + D} \quad (2.6)$$

The analytical results of the designed UWB filter are plotted and compared with simulation results, as shown in Figure 2.6. A shift at higher frequencies are mainly observed in the analytical results due to lossless transmission lines and frequency-independent dielectric material assumptions, which are frequency-dependent parameters and subsequently their in-band transmission and stopband attenuation are relatively higher than the simulated results.

### 2.3 Notched-band UWB filter design

In order to design an UWB filter with notch characteristic, the designed UWB filter in the earlier section is modified by loading exponential tapered impedance line on each quarter wavelength short-circuited stub and the resonator is termed as exponentially tapered impedance line stub loaded microstrip resonator (ETILSLMR). The configuration of the notched-band design with single tapered

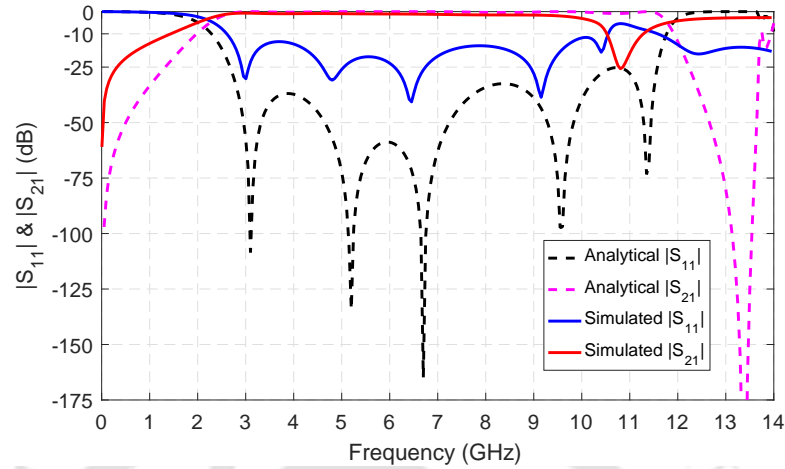


**Figure 2.6:** Comparison of simulation with analytical results for the designed UWB filter.

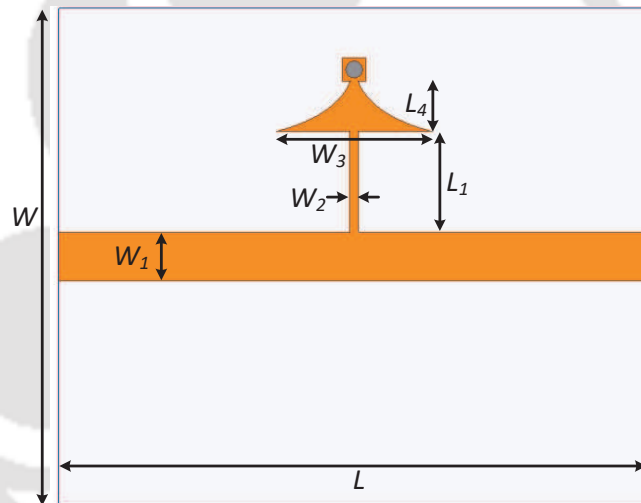


**Figure 2.7:** Configuration of the notched-band design with single tapered SC stub.

SC stub is shown in Figure 2.7. The design parameters are as:  $W = 32$  mm,  $L = 38$  mm,  $W_1 = 3.1$  mm,  $W_2 = 0.5$  mm,  $L_1 = 6.5$  mm and  $L_4 = 3.25$  mm. It has been found that by varying the width of exponentially tapered section  $W_3$ , the notch stopband at a desired frequency in the passband can be achieved, as can be seen in Figure 2.8(a). The tapered loading result in higher inductive effect on quarter-wavelength resonator, due to which a notch-band is produced in the passband. Simulated S-parameters for the proposed single ETILSLMR with  $W_3 = 10$  mm are shown in Figure 2.8(b). The notch-band attenuation could be further improved by loading more of such resonators. By using this method, a notched-band UWB filter is designed, as shown in Figure 2.9. Its optimized dimensions

## 2. Notched UWB filter using ETILSLMR

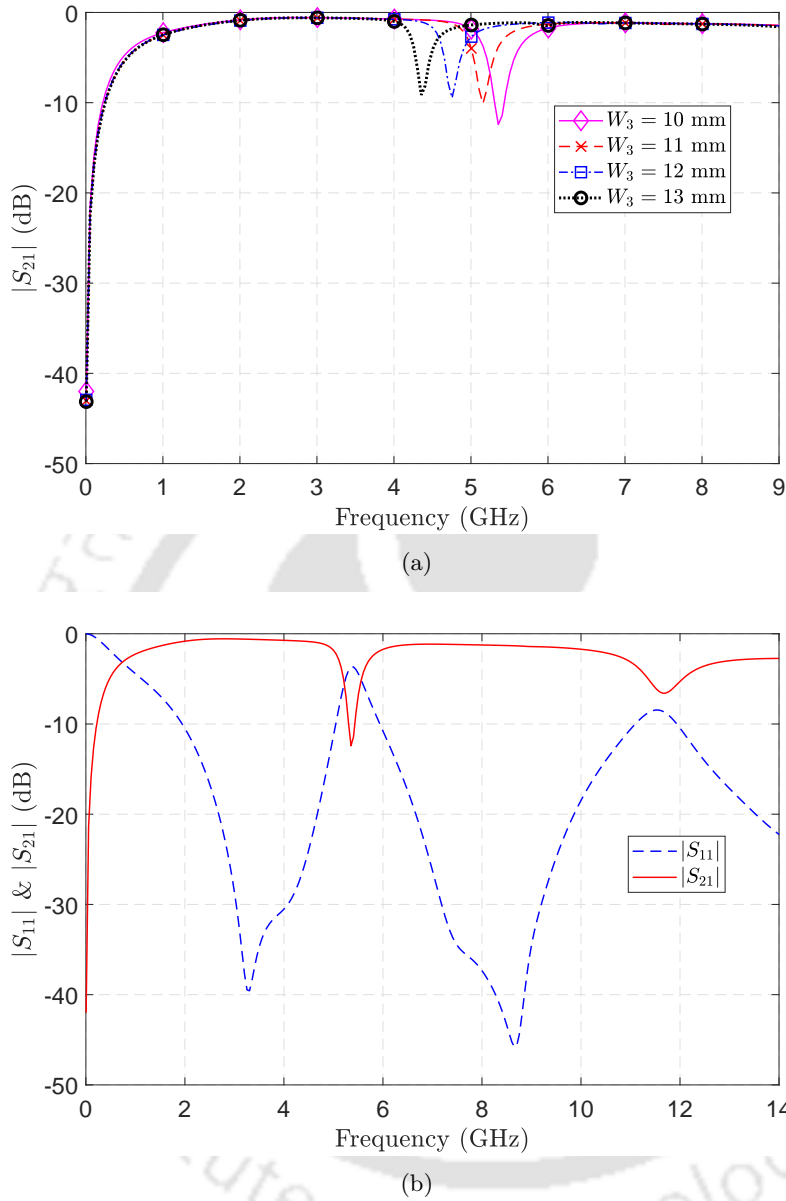


**Figure 2.8:** Simulated results for the notched-band design with single tapered SC stub (a)  $|S_{21}|$  for different tapered widths  $W_3$  and (b) S-parameters with  $W_3 = 10$  mm.

are listed in Table 2.2. All electrical parameters of this filter design are the same as initial UWB filter; only tapered sections and their dimensions are added. The dimensions of exponentially tapered impedance line sections are optimized so that the proposed filter with notch band around 5.5 GHz can effectively suppress the interference from WLAN devices. Figure 2.10 shows the simulated results for the notched-band UWB filter. The attenuation in the notch band region is about 32 dB which is also deep enough to suppress the interference from WLAN devices.

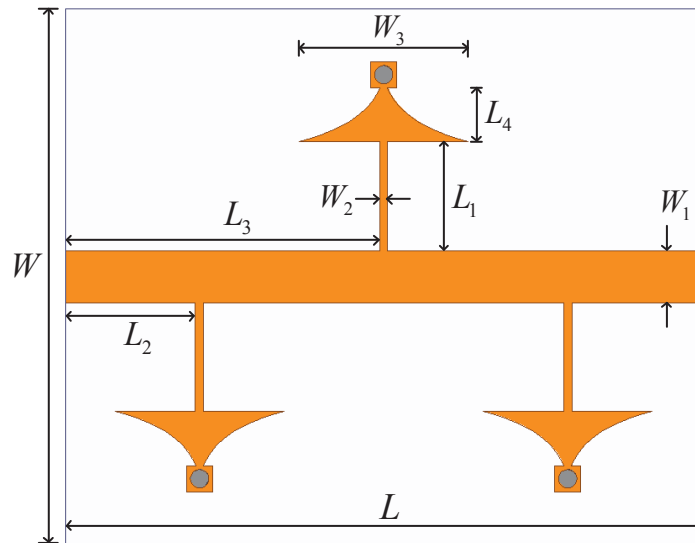


Figure 2.9: Proposed notched-band UWB filter structure.

Table 2.2: Design parameter values for the notched-band UWB filter

$L = 38$ mm	$W = 32$ mm
$L_1 = 6.5$ mm	$W_1 = 3.1$ mm
$L_2 = 7.75$ mm	$W_2 = 0.5$ mm
$L_3 = 18.75$ mm	$W_3 = 10$ mm
$L_4 = 3.25$ mm	

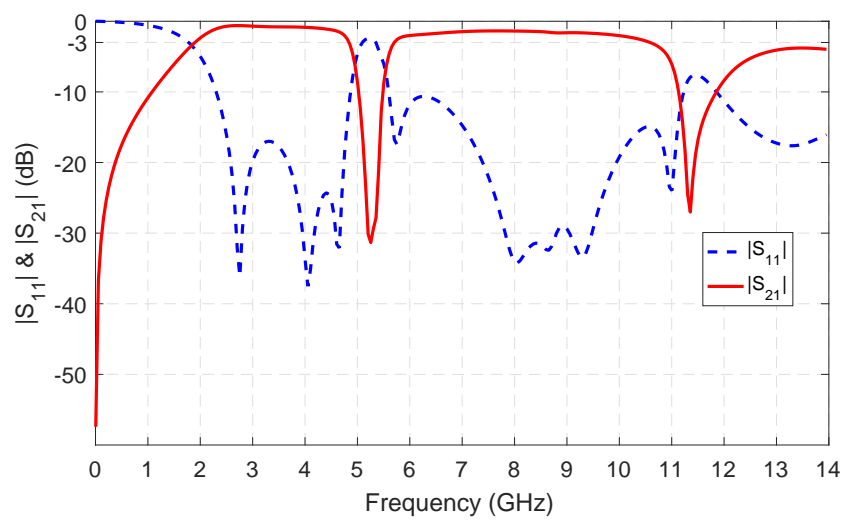


Figure 2.10: Predicted magnitude of S parameters for the notched-band UWB filter.

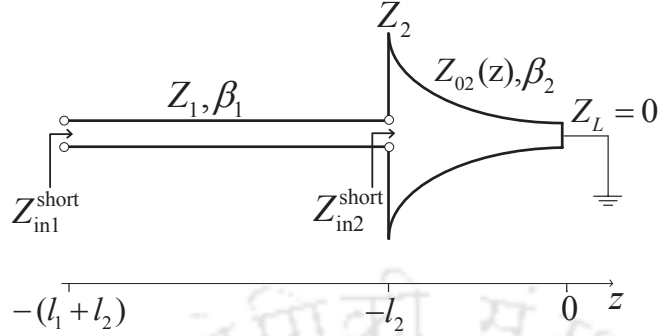


Figure 2.11: Proposed two-section short-circuited transmission line structure.

### 2.3.1 Theoretical analysis of notched-band UWB filter

If an exponential line is terminated with a load impedance of  $Z_L = 0$ , one can find the input impedance  $Z_{in2}^{short}$  of Figure 2.11 from [13] as

$$Z_{in2}^{short} = jX = jZ_2 \frac{1}{\sqrt{1 - \frac{\delta^2}{4\beta_2^2}} \cot\left(\beta_2 \sqrt{1 - \frac{\delta^2}{4\beta_2^2}} l_2\right) - \frac{\delta}{2\beta_2}} \quad (2.7)$$

So, the impedance (or, admittance) of proposed ETILSLMR, as shown in Figure 2.11, can be obtained as

$$\begin{aligned} Z_{in1}^{short} &= Z_1 \left[ \frac{Z_{in2}^{short} + jZ_1 \tan \beta_1 l_1}{Z_1 + jZ_{in2}^{short} \tan \beta_1 l_1} \right] \\ &= jZ_1 \left[ \frac{R_z + \tan \beta_1 l_1 \left\{ \sqrt{1 - \frac{\delta^2}{4\beta_2^2}} \cot\left(\beta_2 \sqrt{1 - \frac{\delta^2}{4\beta_2^2}} l_2\right) - \frac{\delta}{2\beta_2} \right\}}{\left\{ \sqrt{1 - \frac{\delta^2}{4\beta_2^2}} \cot\left(\beta_2 \sqrt{1 - \frac{\delta^2}{4\beta_2^2}} l_2\right) - \frac{\delta}{2\beta_2} \right\} - R_z \tan \beta_1 l_1} \right] \end{aligned} \quad (2.8)$$

$$Y_{in1}^{short} = -jY_1 \left[ \frac{\left\{ \sqrt{1 - \frac{\delta^2}{4\beta_2^2}} \cot\left(\beta_2 \sqrt{1 - \frac{\delta^2}{4\beta_2^2}} l_2\right) - \frac{\delta}{2\beta_2} \right\} - R_z \tan \beta_1 l_1}{R_z + \tan \beta_1 l_1 \left\{ \sqrt{1 - \frac{\delta^2}{4\beta_2^2}} \cot\left(\beta_2 \sqrt{1 - \frac{\delta^2}{4\beta_2^2}} l_2\right) - \frac{\delta}{2\beta_2} \right\}} \right] \quad (2.9)$$

where  $Z_{02}(z)$  is the impedance of exponentially tapered line with a positive rate of taper  $\delta$  and  $R_z$  is the lowest to highest impedance ratio of the stub line ( $R_z = \frac{Z_2}{Z_1}$ ). After defining the impedance (or, admittance) of the proposed ETILSLMR and their electrical parameters, one can find the S-parameters by using transmission line network analysis.

With the same assumptions as taken in the previous section and ignoring the effects of step discontinuities, an approximate theoretical analysis for notched-band UWB filter has also been carried out. The [U] and [W] matrices will remain same as equation (2.2) and (2.4), and only [V] matrix will

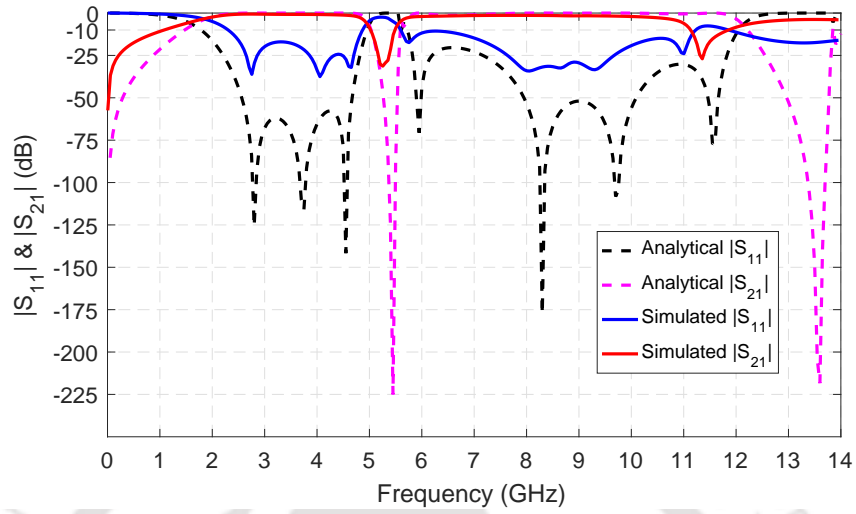


**Figure 2.12:** Comparison of simulation with analytical S-magnitudes for the notched-band UWB filter.

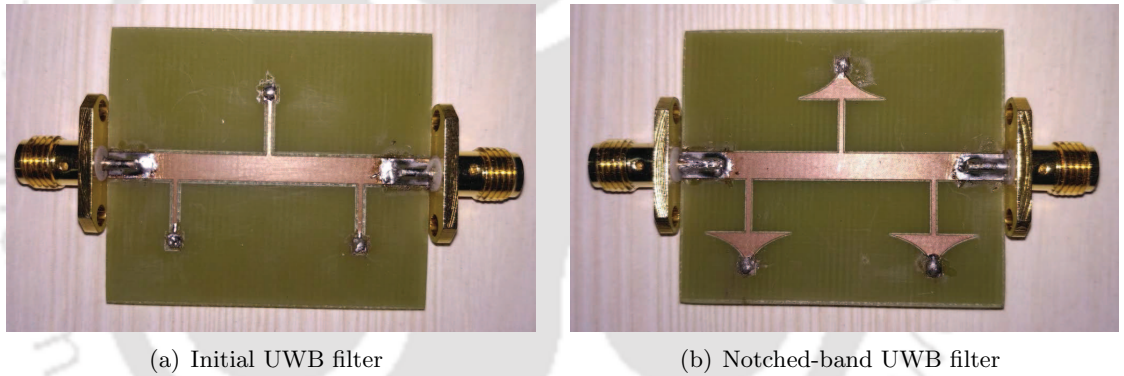
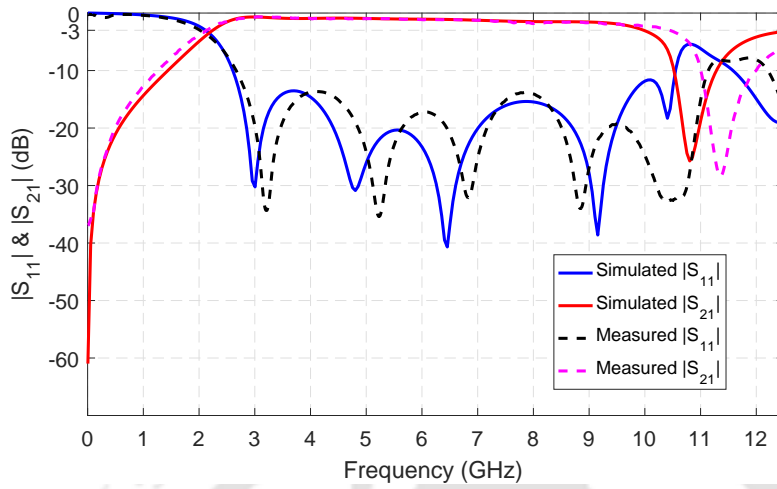


**Figure 2.13:** Photograph of the fabricated filters.

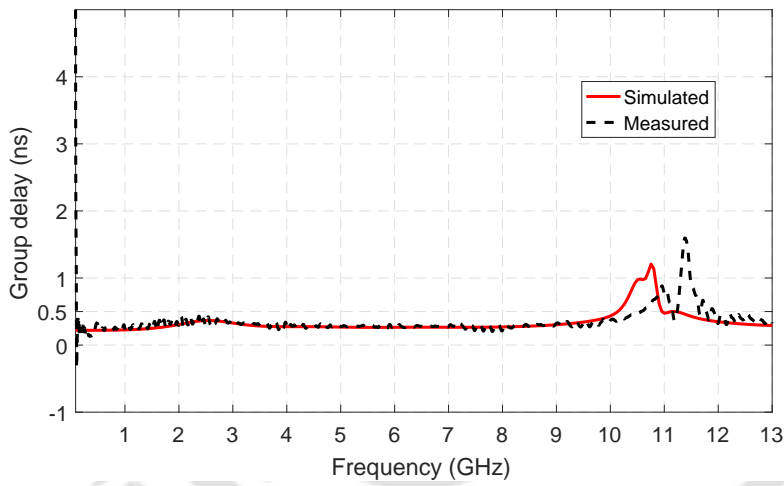
be changed as only each shunt short-circuited stubs of quarter wavelength are replaced by two-section exponentially tapered impedance short-circuited stubs for realizing the notched-band UWB filter, which can be written as

$$[V] = \begin{bmatrix} 1 & 0 \\ Y_{in1}^{short} & 1 \end{bmatrix} \quad (2.10)$$

where,  $Y_{in1}^{short}$  has already been derived in (2.9). The overall ABCD matrix of transmission line network for the proposed model is obtained from (2.1), and finally, S parameters are found from (2.5) and (2.6). The analytical and simulated results of the proposed notched-band UWB filter are compared in Figure 2.12. A good match between the two results is achieved except a slight shift at higher frequencies due



(a) S-magnitudes



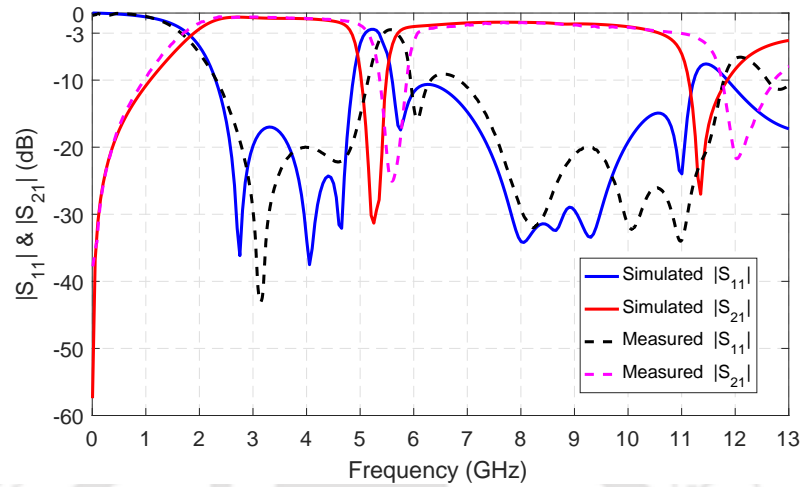
(b) Group delay

**Figure 2.14:** Comparison of measured and simulated results for the initial UWB filter.

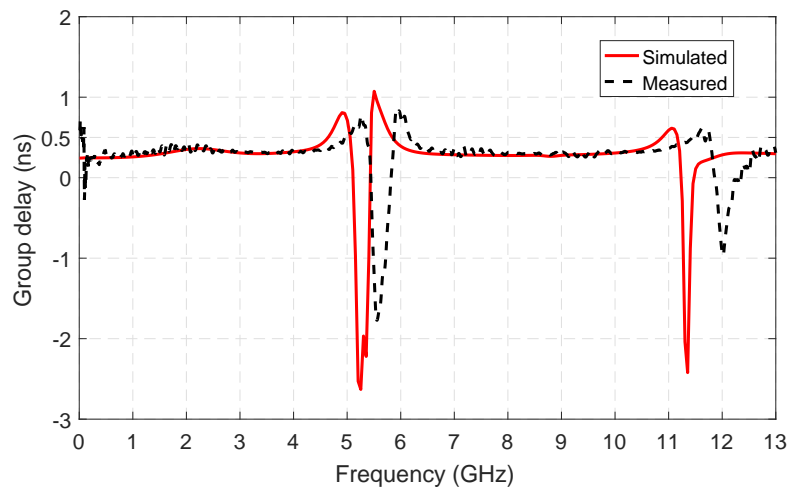
to simplified assumptions as mentioned in previous section.

## 2.4 Comparison with measured results

For experimental verification, two prototype filters with optimized electrical parameters are fabricated using a conventional PCB technology and measured using ZVA 24 VNA. The fabricated filters are shown in Figure 2.13. The via-hole grounds of 1.1 mm diameters are made through soldering and two SMA connectors at the input-output ports are connected for the measurement. The predicted and measured S-magnitudes and group delay for initial UWB filter, and notched-band UWB filter are plot-



(a) S-magnitudes



(b) Group delay

**Figure 2.15:** Comparison of measured and simulated results for the proposed UWB filter with notch function.

ted together in Figure 2.14 and Figure 2.15, respectively. A good agreement between the two results is achieved which validate the proposed filter designs. The measured 10 dB passband for initial UWB filter ranges from 2.7 GHz to 11 GHz with FBW of 121% at a center frequency of 6.85 GHz, whereas in case of the notched-band UWB filter, the measured sharp notch stopband is achieved between 5.3 GHz to 5.8 GHz and passband regions are covered in the two frequency bands, 2.3-5.3 GHz and 5.8-11.7 GHz, respectively. The maximum predicted and measured group delay variation in their passband is about 0.35 ns for both filters. The proposed filters do not incorporate any defected ground structures and can be fabricated easily. The shift towards higher frequencies in measured results are observed

## 2. Notched UWB filter using ETILSLMR

---

**Table 2.3:** Comparison of notch band characteristics with reported notched-band UWB filters

References	Notch frequency (GHz)	Notch-band rejection level (dB)	Notch-band 10-dB FBW (%)	Group delay (ns)	Size (Length×Width) ( $\lambda_g \times \lambda_g$ )
[52]	5.47	25	~ 6	<0.2	0.97×0.43
[53]	5.83	23, 34	4.6, 6.5	0.5	1.07×0.54
[54]	5.8	30	~ 5	–	1.11×0.79
[55]	5.5	32	9.09	–	1.47×0.21
[56]	5.6	39	15.6	<0.7	1.58×1.33
This work	~ 5.5	32	9	<0.35	1.58×1.33

primarily due to imprecise calibration set-up for the measurement, frequency-dependent losses of the dielectric material and the connectors, and unexpected tolerances in the fabrication similar to what has been reported in [47] and [53]. The inductive loading at the short-circuited point get increased when the diameter of vias becomes larger or when number of vias at the short circuited point will increase. This is due to increased inductive reactance at that points. The fabrication tolerances also add such reactive effects which causes slight shift of the frequency band.

The notch band characteristics of the proposed notched-band UWB filter is compared with the other reported filters, as depicted in Table 2.3. The rejection level of 25 dB with a good group delay (<0.2 ns) is achieved in [52], while in [53], two filters with better feasibility and narrower notch FBW of 4.6% and 6.5%, are developed. In [54], a narrow notch band of 30 dB attenuation with tight coupling gaps is observed. By placing CSSRR on the ground plane in [55], a good notch characteristic of 32 dB is obtained, while in [56], rejection level is 39 dB which is highest among all but suffers with wider notch band and higher group delay. In this work, a good rejection level of 32 dB, better notch band FBW of 9% and less than 0.35 ns group delay is achieved. Since the fractional bandwidth of notch band is lesser, the filter possesses higher selectivity as the selectivity of notch band filter is determined by its quality factor or, 10-dB fractional bandwidth (FBW). Higher the 10-dB FBW of notch band implies lesser its quality factor and lesser its selectivity. The selectivity of proposed notch band filter can be calculated as the ratio ( $f_0/(f_2 - f_1)$ ) in dB = 10.5 dB, where  $f_0$ ,  $f_1$  and  $f_2$  are the notch frequency, lower and upper 10-dB cut off frequencies of the notch band respectively. The roll-off rate or steepness of the proposed notch band filter at higher stopband transition is about 27.5 dB/GHz. This can further be improved by increasing number of such resonators. The proposed design does not

employ any defected ground structures or embedded structures and can be used in UWB technologies with some trade-offs in its design and performances.

## 2.5 Summary

In this chapter, we have proposed a novel exponentially tapered impedance line stub loaded microstrip resonator (ETILSLMR) to design a notched-UWB filter. Initially, an UWB filter with FBW of 121% at a center frequency of 6.6 GHz is designed by loading three identical quarter-wavelength short-circuited stubs to the main  $50 \Omega$  microstrip line. Later on, to suppress interference from IEEE 802.11a WLAN band, a notched-band UWB filter is designed by tapered inductive loading on quarter-wavelength high impedance lines. An approximate theoretical analysis has also been carried out for both filters, and consequently, two prototype filter designs are fabricated and measured for experimental verification. We have found good agreements among the analytical, EM simulated and measured results of the filters, which validate the proposed designs.



# 3

## Linear tapers: analysis, design and applications

### Contents

---

3.1	Introduction . . . . .	40
3.2	Linear impedance taper . . . . .	42
3.3	Comparison with different tapered lines . . . . .	44
3.4	Linearly tapered transition between microstrip line and SIW component	47
3.5	Linearly tapered coupled-line ultra-broadband bandpass filter . . . . .	51
3.6	Summary . . . . .	58

---

### 3. Linear tapers: analysis, design and applications

---

Linear tapers are the simplest type of tapers, used mainly for broadband impedance matching between the two transmission lines of different characteristic impedances and also in the design of filters, power dividers, antennas, etc. Surprisingly, they have not been theoretically characterized in the literature. By using theory of small reflections, the characteristics of linear impedance taper (generalized case) and linear width taper (approximate case) have been analyzed in terms of reflection coefficient, and their results are compared with the characteristics of other tapers. It has been found that the reflection coefficient response for the linear tapers is very close to exponential taper. For impedance and field pattern matching between microstrip line and substrate integrated waveguide (SIW) component, a linearly tapered transition has been designed and implemented at X-band. Moreover, using linear width taper, a novel linearly tapered coupled-line ultra-broadband bandpass filter is designed, fabricated and tested, which possesses a very compact size of  $0.20\lambda_g \times 0.26\lambda_g$  and wide 10 dB passband of 4.5 to 12 GHz.

#### 3.1 Introduction

The linear tapers, as shown in Figure 3.1, are the most common and simple tapers which are used for eliminating the step discontinuities between transmission lines, designing broadband impedance matching networks, couplers, filters, antennas etc. There are other types of tapers [2], like triangular taper, exponential taper, and Klopfenstein taper, whose reflection coefficient response  $\Gamma(\theta)$  and respective impedance variation  $Z(z)$  are well known. In their analysis,  $Z(z)$  is known and  $\Gamma(\theta)$  is found as a function of frequency. However, if  $\Gamma(\theta)$  is specified, then in principle  $Z(z)$  can be obtained but this procedure is very difficult and generally avoided [4]. An analytical solution and the exact linear two-port ABCD matrix in terms of Bessel functions for linearly varied nonuniform transmission line has been presented in [27] and a simplified analytical CAD model for linearly tapered microstrip line including losses has been developed in [28]. An approximate expression for reflection coefficient of a linear taper in rectangular waveguide has been examined for  $TE_{10}$  mode in [104]. To the best of my knowledge, linear width and linear impedance tapers have extensively used in the design of microwave devices but they have not been theoretically characterized and compared with the other tapers. In this work, we have tried to find-out impedance variation, width variation, and for the first time, resulting reflection coefficient response for the linear tapers in the simplest form. The impedance for linear impedance taper and width for linear width taper varies linearly along the line, as shown

in Figures 3.1 (a) and 3.1 (b) respectively. Based on the theory of small reflections, a generalized reflection coefficient response for linearly varying impedance taper  $Z(z)$  and an approximate reflection coefficient response for linear width taper has been derived and their characteristics are compared with the other tapers. From the reflection coefficient response, we can see that the behaviour of linear tapers is very similar to exponential taper. They are preferred over other tapers due to their simple design and easy fabrication.

The tapers have been extensively used in the design for impedance and field pattern matching between microstrip line and substrate integrated waveguide (SIW) component [85, 91, 94, 105]. A tapered transition from microstrip line to integrated rectangular waveguide on the same substrate has been proposed in [85] for the first time. In [91], the design equations for tapered transition between microstrip-to-SIW has been developed, which make it possible to design full bandwidth transitions without much optimization or full-wave simulations. A millimeter-wave broadband transition on high-to-low dielectric constant substrates for SIW technology has been implemented in [105], where a tapered high dielectric constant substrate is sandwiched between two SIWs. A new design procedure for tapered transition between microstrip line to SIW component has been presented in [94], following some error approximation method and different structures designed at different frequency bands. However in [94], the physical taper used for taper transition is linearly varied microstrip taper while in the design procedure they have used reflection coefficient response of a triangular taper. As we will see that linear tapers and triangular taper have different characteristics. Also, triangular taper is not easy to realize practically like linear tapers. In this work, a linearly varied tapered transition as well as different stepped transitions between microstrip-to-SIW have been realized at X-band, which shows much better performance than [94] in the desired band.

As we have discussed in the previous chapter, there are several techniques being developed to achieve a wideband, ultra-broadband or ultra-wideband (UWB) bandpass filters [33, 35–37, 39, 50, 106, 107]. In [37], very compact and broad-band filters have been developed owing to coupled-line sections and step impedance as an inverter circuits, and a coupled-line BPF with wide stopband by using DGS has been proposed in [108]. By utilizing hybrid microstrip/coplanar waveguide (CPW) structure, the desired tight coupling have been realized for designing UWB filters [39, 106], where the CPW resonators are one or half-wavelength long. In [50], an UWB bandpass filter with insertion loss of less than 1 dB for frequency band of 4.4 to 9.3 GHz has been proposed. The model consists a

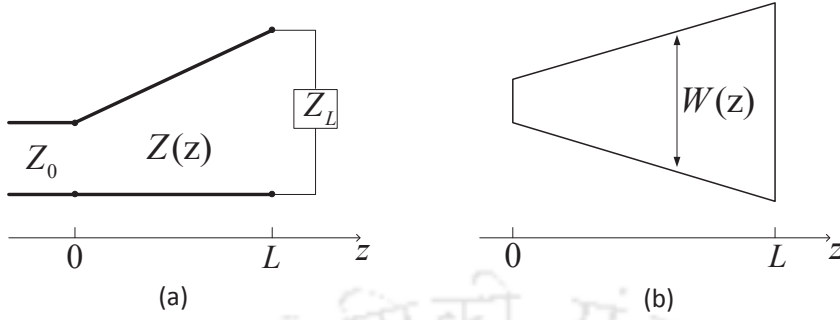


**Figure 3.1:** (a) Linear impedance taper and (b) Linear width taper.

coupled double-stepped structure and an open loop defected ground structure (DGS) on the ground for achieving UWB BPF characteristics. Also, six conventional DGSs, which work as a low pass filter, have been etched on the ground plane to achieve a very wide upper stopband of attenuation more than 30 dB in the range of 11.1 to 20 GHz at the cost of some increased size. In this work, a novel linearly tapered coupled-line ultra-broadband bandpass filter (BPF) has been proposed and examined. The filter comprises an open loop DGS on the ground which is coupled to quarter wavelength linearly tapered coupled-microstrip line open-circuited stubs on the main  $50 \Omega$  line (input-output feedlines). It shows wide 10 dB return loss bandwidth of 7.5 GHz from 4.5 to 12 GHz with a fractional bandwidth of more than 90% at the center frequency of 8.25 GHz.

### 3.2 Linear impedance taper

In this section, the reflection coefficient for linear impedance taper is derived. For a continuously varying tapered line of characteristic impedance  $Z(z)$ , the reflection coefficient is given using (1.10) as

$$\Gamma(\theta) = \frac{1}{2} \int_{z=0}^L e^{-2j\beta z} \frac{d}{dz} \left\{ \ln \left( \frac{Z(z)}{Z_0} \right) \right\} dz \quad (3.1)$$

The impedance variation for the linear impedance taper can be expressed as

$$Z(z) = az + Z_0 \quad (3.2)$$

where the constant  $a$  is

$$a = \frac{Z_L - Z_0}{L} \quad (3.3)$$

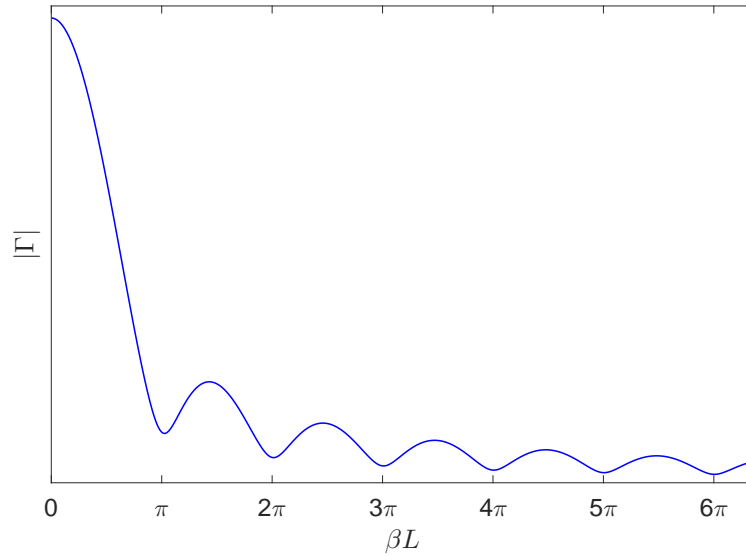


**Figure 3.2:** Reflection coefficient magnitude response for the linear impedance taper.

At  $z = 0$ ,  $Z(0) = Z_0$  and at  $z = L$ ,  $Z(L) = Z_L$  where  $L$  is the length of tapered line.

So, the reflection coefficient for linear impedance taper can be obtained from (3.1) as

$$\Gamma(\theta) = \frac{b}{2} \int_0^L e^{-2j\beta z} \cdot \frac{1}{bz + 1} dz$$

where,  $b = \frac{a}{Z_0}$ .

Let,

$$bz + 1 = y \Rightarrow dz = dy/b$$

For

$$z = 0, y = 1 \quad \text{and} \quad z = L, y = bL + 1$$

So,

$$\Gamma(\theta) = \frac{e^{\frac{2j\beta}{b}}}{2} \int_1^{bL+1} e^{\frac{-2j\beta y}{b}} \cdot \frac{1}{y} dy$$

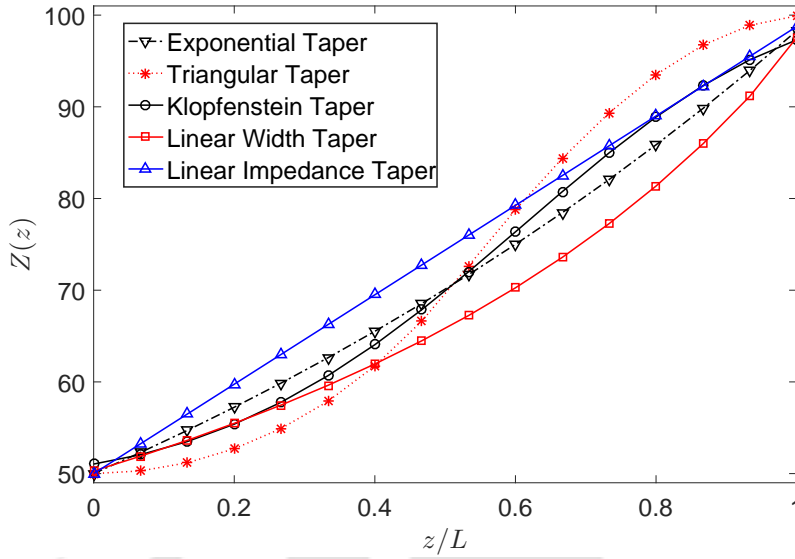


**Figure 3.3:** Impedance variations for the different tapers.

Since,

$$\int \frac{e^{ax}}{x} dx = \ln |x| + \sum_{n=1}^{\infty} \frac{(ax)^n}{n.n!} \quad (3.4)$$

Hence,

$$\Gamma(\theta) = \frac{e^{\frac{2j\theta}{bL}}}{2} \left( \ln |bL + 1| + \sum_{n=1}^{\infty} \left( \frac{-2j\theta}{bL} \right)^n \left[ \frac{(bL + 1)^n}{n.n!} - \frac{1}{n.n!} \right] \right). \quad (3.5)$$

The magnitude of this reflection coefficient is plotted in Figure 3.2. The minimum amplitude occurs at each multiple of  $\pi$  and decreases gradually without reaching zero, unlike exponential taper.

### 3.3 Comparison with different tapered lines

The characteristics of linear impedance taper have been validated by comparing them with the design of other tapers [2], a triangular taper, an exponential taper, a Klopfenstein taper (with  $\Gamma_m = 0.02$ ) and a linear width taper to match a  $100 \Omega$  load ( $Z_L = 100 \Omega$ ) to a  $50 \Omega$  line ( $Z_0 = 50 \Omega$ ). The impedance variations and width variations,  $W(z)$  in mm have been plotted in Figure 3.3 and Figure 3.4 respectively. In several cases, linear width taper has been taken as triangular taper in the literature. But triangular taper does not have linear width as depicted in Figure 3.4. For obtaining width variations from corresponding impedance variations using microstrip line equations,

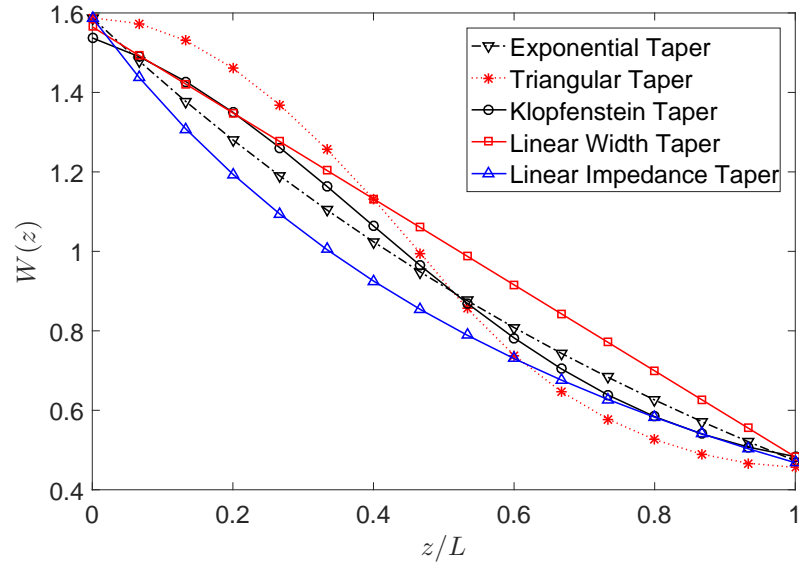


**Figure 3.4:** Width variations for the different tapers.

we have assumed the substrate with dielectric constant of 2.2 and height of 0.508 mm. To compare the reflection coefficient magnitude response of linear impedance taper with linear width taper and other tapers of known responses, we need to find reflection coefficient of linear width taper first, which will be carried-out in this section.

For designing a linearly tapered microstrip line, the width should vary linearly along the line which is named here as linear width taper. The reflection coefficient for linear width taper could be found if its impedance variation  $Z(z)$  is brought in the form so that when we apply it in (3.1), the integral operation can be performed. As in all other case of tapers, their impedance variations are known and (3.1) has been used for finding their reflection coefficient response but for linear width taper case, the impedance variation need to be found from its width variation followed by the complex equation of impedance for microstrip line [2], and hence to apply (3.1), it requires an approximation for this case. Subsequently, we have considered one of the substrate material to validate and compare it with linear impedance taper and others. However, in a general case of different substrate materials, the characteristics of reflection coefficient response for linear width taper would not change significantly as their derivation will be followed accordingly. Hence, for  $Z_L = 100 \Omega$ ,  $Z_0 = 50 \Omega$ ,  $L = 20$  mm and substrate with dielectric constant of 2.2 and height of 0.508 mm, an approximate closed form exponential expression of impedance variation for linear width taper is obtained from curve fitting

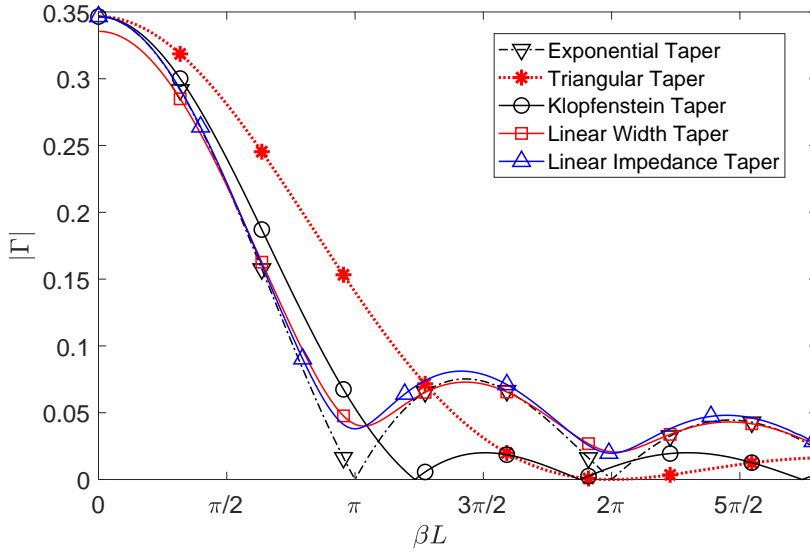


**Figure 3.5:** Reflection coefficient magnitude versus frequency for the different tapers.

technique by using Figure 3.3 of impedance variation plot for linear width taper as

$$Z(z) = 1.012074Z_0e^{(0.02055z+0.00065z^2)} \quad (3.6)$$

Hence, we can obtain the reflection coefficient for linear width taper line from (3.1) as

$$\Gamma(\theta) = \frac{1}{2}Le^{-j\beta L} \left( 0.02055 \times \frac{\sin \beta L}{\beta L} - jL \times 0.00065 \times \frac{\sin \beta L}{(\beta L)^2} + jL \times 0.00065 \times \frac{e^{-j\beta L}}{\beta L} \right). \quad (3.7)$$

The magnitude of this reflection coefficient is plotted in Figure 3.5 along with the other tapers. The reflection coefficient response of linear width taper almost coincide with linear impedance taper which implies that passband characteristics of the two remain nearly same. However, in both cases, the minima occur at each multiple of  $\pi$  and their amplitude is gradually decreasing without reaching zero, unlike exponential taper. So, the passband characteristic of exponential taper will be somewhat better than these two but it is not so significant as in case of higher frequency. Therefore, the linear tapers can be preferred over it due to their simple design and easy fabrication. The peaks of the triangular taper are lower than the corresponding peaks of exponential and linear tapers case but the first null for the triangular taper occurs at  $\beta L = 2\pi$ , whereas for the exponential taper it occurs at  $\beta L = \pi$ . It implies that at lower frequencies, the exponential and linear tapers will have better passband than triangular taper. For the given condition ( $\Gamma_m = 0.02$ ), the Klopfenstein taper provides better passband than all other tapers but its design consists of modified Bessel function which is very

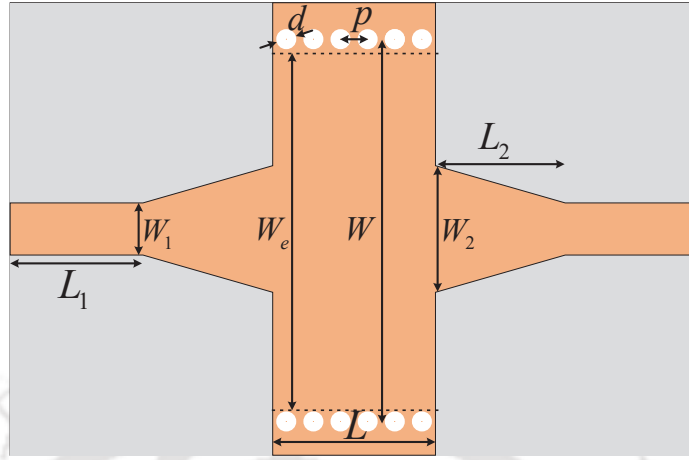


**Figure 3.6:** Schematic of the linearly tapered transition between microstrip line and SIW section.

complex to design practically and also it has step discontinuity at the junctions  $z = 0$  and  $L$  (the ends of the tapered section). The response of the Klopfenstein taper has equal-ripple lobes versus frequency in its passband.

### 3.4 Linearly tapered transition between microstrip line and SIW component

The schematic of linearly tapered transition between microstrip line and SIW component designed at X-band is shown in Figure 3.6. The design consists of two parts; one is SIW part and the other is microstrip taper part. The SIW part is designed following the theory and well-known design equations of [86, 87]. The effective width  $W_e$  of SIW can be found by

$$W_e = W - \frac{d^2}{0.95 \cdot p} \quad (3.8)$$

where  $W$  is the width of SIW,  $d$  is the diameter of metallic vias and  $p$  is the pitch. The pitch and via diameter should follow the two design rules to neglect the radiation loss

$$\begin{aligned} d &< \lambda_g/5 \\ p &\leq 2d \end{aligned} \quad (3.9)$$

where  $\lambda_g$  is the guided wavelength in the SIW. The initial width of microstrip taper ( $W_2$ ) can be found

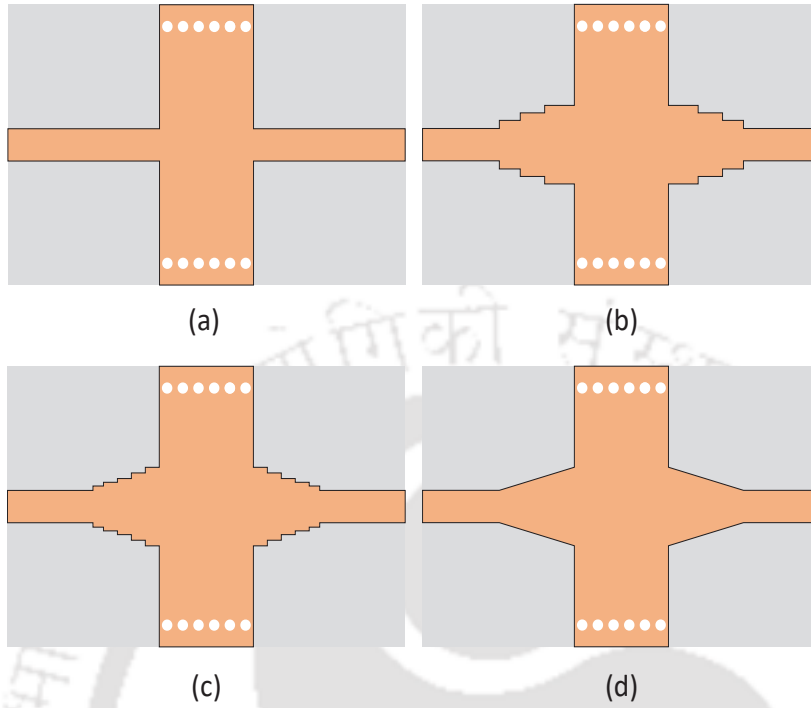


**Figure 3.7:** SIW model with different transitions (a) No transition (b) 3 steps transition (c) 5 steps transition and (d) Linearly tapered transition.

from [91] as

$$\frac{W_e}{X} = 0.38e^{-0.627 \frac{\epsilon_r + 1 + \frac{\epsilon_r - 1}{2}}{\epsilon_r - 1} \frac{1}{\sqrt{1 + 12h/W_2}}} \quad (3.10)$$

$$\frac{1}{X} = \begin{cases} \frac{60}{\eta h} \ln \left( \frac{8h}{W_2} + \frac{W_2}{4h} \right) & \left( \frac{W_2}{h} \leq 1 \right) \\ \frac{120\pi}{\eta h [W_2/h + 1.393 + 0.667 \ln(W_2/h + 1.444)]} & \left( \frac{W_2}{h} \geq 1 \right) \end{cases} \quad (3.11)$$

where  $\eta = (\mu_0/\epsilon_0)^{1/2}$ . For a given substrate ( $h$  and  $\epsilon_r$ ) and effective width of SIW ( $W_e$ ), we can equate (3.10) and (3.11), and solve it to find  $W_2$ , which is the width of microstrip taper. The length of taper ( $L_2$ ) should be an integral multiple of quarter wavelength ( $n\lambda_{g0}/4$ , where  $\lambda_{g0}$  is the guided wavelength at the design frequency).

To design an X-band SIW, the standard X-band rectangular waveguide WR-90 with dimensions of 22.86 mm  $\times$  10.16 mm is considered. The model is designed using Rogers 4350B substrate with a dielectric constant of 3.48, loss tangent of 0.0037 and thickness of 0.762 mm. The dimensions of SIW are calculated as:  $W_e = 12.25$  mm,  $d = 0.6$  mm,  $p = 0.9$  mm,  $W = 12.67$  mm and  $L = 5.4$  mm. The initial width of microstrip taper  $W_2$  is obtained from (3.10) and (3.11) and optimized using full-wave

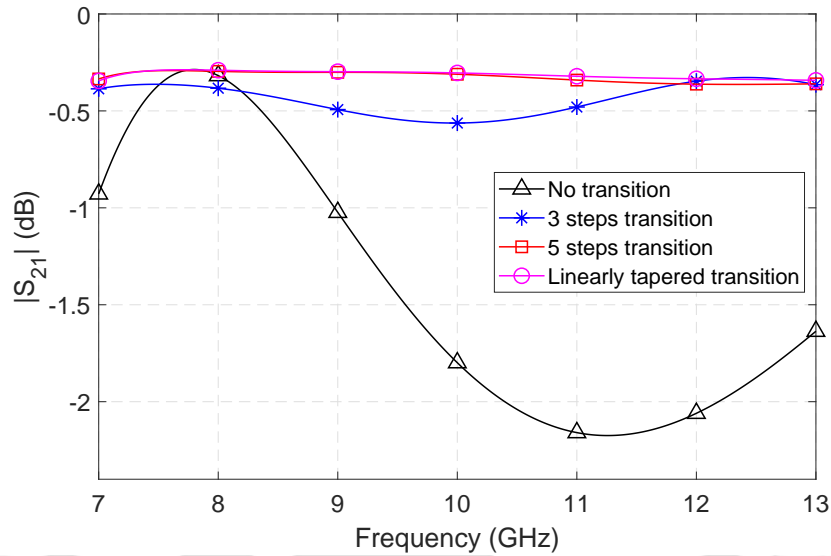


Figure 3.8:  $|S_{21}|$  for stepped vs. linearly tapered transition.

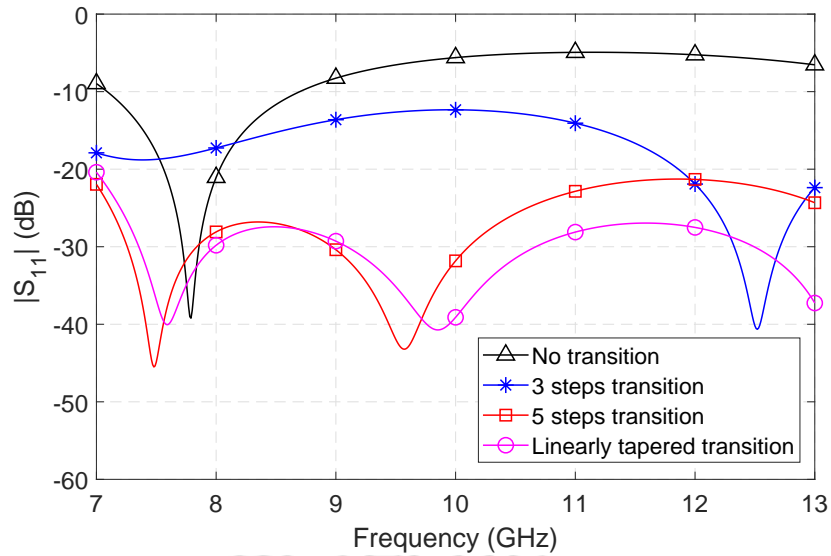
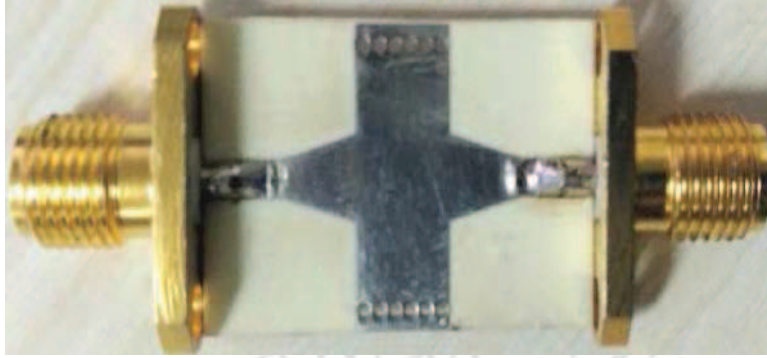


Figure 3.9:  $|S_{11}|$  for stepped vs. linearly tapered transition.

HFSS simulations. The optimized dimensions are: the width and length of  $50 \Omega$  line,  $W_1 = 1.73$  mm and  $L_1 = 8.7$  mm respectively, and the width and length of taper line,  $W_2 = 4.2$  mm and  $L_2 = 4.3$  mm respectively.

Moreover, it has been investigated that as the design shifts from no transition to a linearly tapered transition, as shown in Figure 3.7, their performances are gradually improved, as can be seen in Figures 3.8 and 3.9. The dimensions of each designs are kept same as for the design shown in Figure 3.6. Their

### 3. Linear tapers: analysis, design and applications



**Figure 3.10:** Prototype of fabricated linearly tapered transition between microstrip line and SIW component.

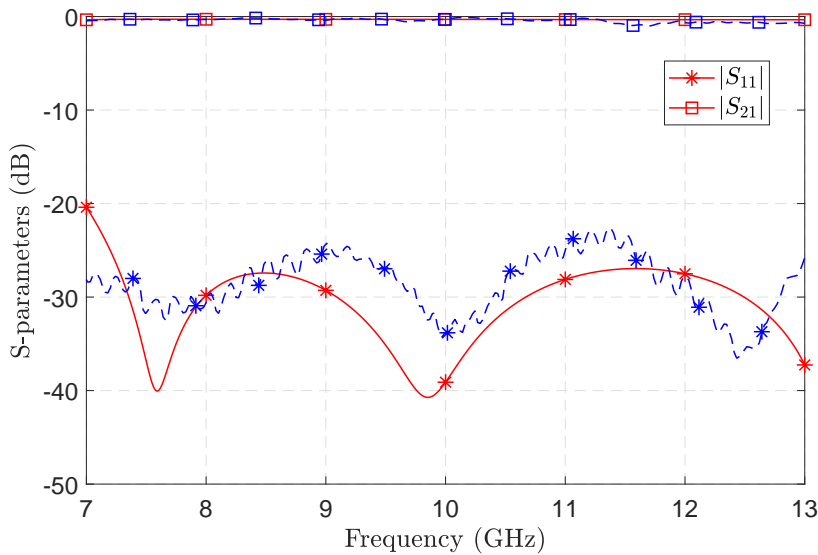


**Figure 3.11:** S-parameters of the linearly tapered transition (Solid lines represent simulated results and dashed lines represent measured results).

insertion loss (IL) and return loss (RL) are shown in Figures 3.8 and 3.9. The IL is highly improved from 2.2 dB for no transition to 0.35 dB for linearly tapered transition and the RL is considerably increased from 5 dB for no transition to 27 dB for linearly tapered transition, in their whole desired X-band of 8-12 GHz.

A prototype of linearly tapered transition between microstrip line and SIW section has been fabricated and tested, as shown in Figure 3.10. Their plots in Figure 3.11 show that the insertion loss is better than 1 dB and return loss is more than 22 dB in whole X-band of 8-12 GHz. The performances are quite better than [94], where the measured insertion loss is about 4 dB and return loss of only around 6 dB in their frequency band of 8.20-12.47 GHz.

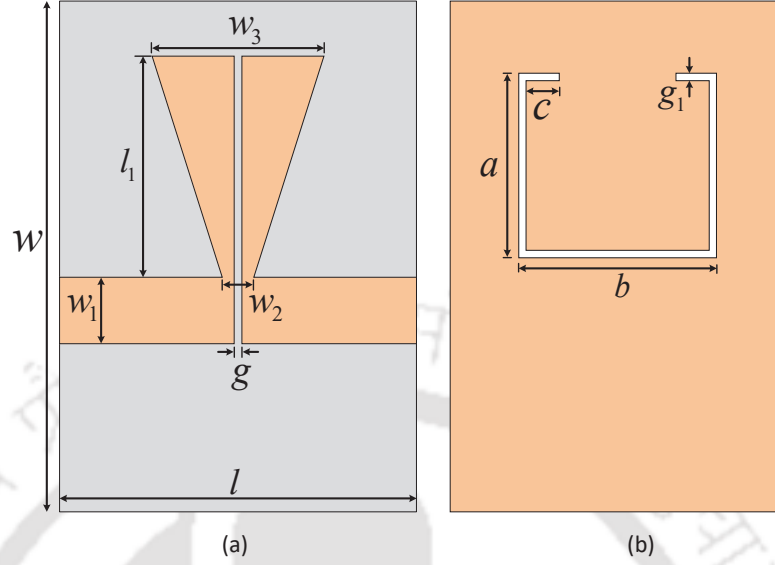


**Figure 3.12:** Schematic of the proposed ultra-broadband BPF design (a) Top view and (b) Bottom view (open loop DGS on the ground).

### 3.5 Linearly tapered coupled-line ultra-broadband bandpass filter

This section presents a novel ultra-broadband bandpass filter (BPF) using linearly tapered coupled-microstrip line and open loop defected ground structure (DGS). The filter structure consists of a quarter wavelength linearly tapered coupled-microstrip line open-circuited stubs and an open loop etched DGS on the ground. The quarter wavelength long linearly tapered and tightly coupled microstrip open-circuited stubs can function as two resonators, and with an associated enhanced coupling structure to open loop DGS, it leads to a very compact three-pole filter. The proposed filter also exhibits a quasi-elliptic function response, where two transmission zeros closer to each side of the passband to improve selectivity and one transmission zero at higher side of the upper stopband, can be observed. The simulated and measured results of the filter are in well agreement with each other, showing a wide 10 dB return loss (RL) bandwidth from 4.5 to 12 GHz, insertion loss better than 1.5 dB and group delay variation of lesser than 0.2 ns in the whole passband. Furthermore, it has a very compact size of  $0.20\lambda_g \times 0.26\lambda_g$  at the center frequency of 8.25 GHz.

#### 3.5.1 Filter structure and operation

Coupled microstrip line, microstrip line loaded with open circuited stubs and defected ground structure (DGS) are widely used in the design of microstrip BPF. In this work, we have proposed

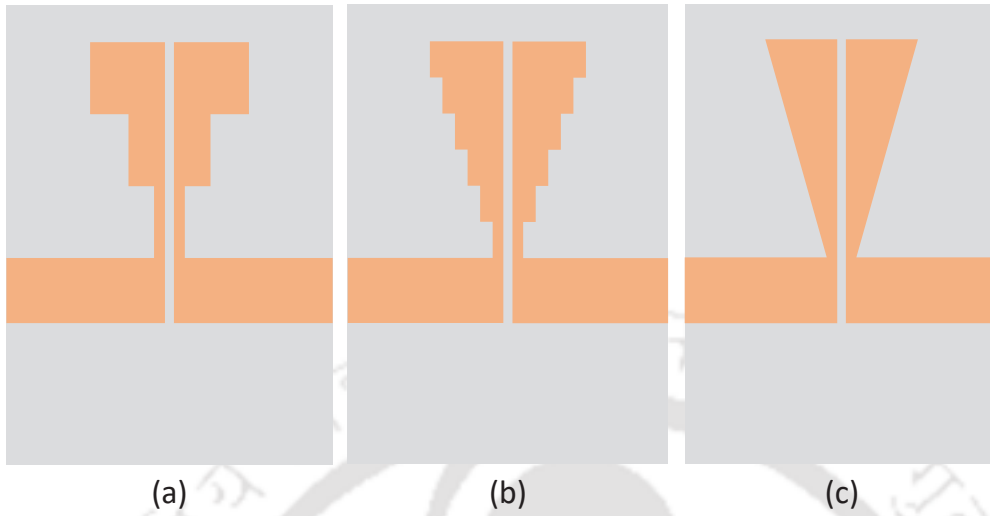


**Figure 3.13:** The model with different coupled-lines (a) 3 stepped (b) 6 stepped and (c) Linearly tapered coupled-line.

a compact linearly tapered coupled-microstrip line which is a hybrid of microstrip line loaded with open circuited stubs and coupled microstrip line and open loop-DGS to realize an ultra-broadband microstrip BPF. The BPF is highly compact because of the linearly tapered coupled-microstrip line with tight coupling in the microstrip plane and open loop-DGS in the ground plane. Figure 3.12 shows schematic of the proposed ultra-broadband BPF, where a linearly tapered coupled-microstrip line open-circuited stubs of about a quarter-wavelength long is loaded on the conventional  $50 \Omega$  input/output feedlines and an open loop DGS etched on the ground. The dielectric material used for the design is Rogers RT/Duroid 5880 substrate with a dielectric constant of 2.2, dielectric loss tangent of 0.0009 and thickness of 0.508 mm. The optimized dimensions of the filter are:  $l = 9.14$  mm,  $w = 16$  mm,  $w_1 = 1.565$  mm,  $w_2 = 0.86$  mm,  $w_3 = 4.45$  mm,  $l_1 = 5.187$  mm,  $g = 0.25$  mm,  $a = 4.95$  mm,  $b = 5.4$  mm,  $c = 0.905$  mm and  $g_1 = 0.25$  mm. The open loop DGS ensures high Q factor as compared to other types of DGSs and results in good out-of-band filter performances and reduced circuit size [50].

Firstly, we have designed multi-stepped coupled-line structures, which are about a quarter wavelength long, as shown in Figure 3.13, and wideband filtering is observed (see Figure 3.14). When the multi-stepped coupled lines are transformed into linearly tapered coupled-line, a wider and better filtering performance has been achieved. The HFSS simulated magnitude of  $S_{21}$  for 3-stepped, 6-stepped and linearly tapered coupled-lines without open-loop DGS on the ground are plotted in Figure 3.14. The in-band characteristics such as insertion loss and bandwidth are still very poor and hence an open

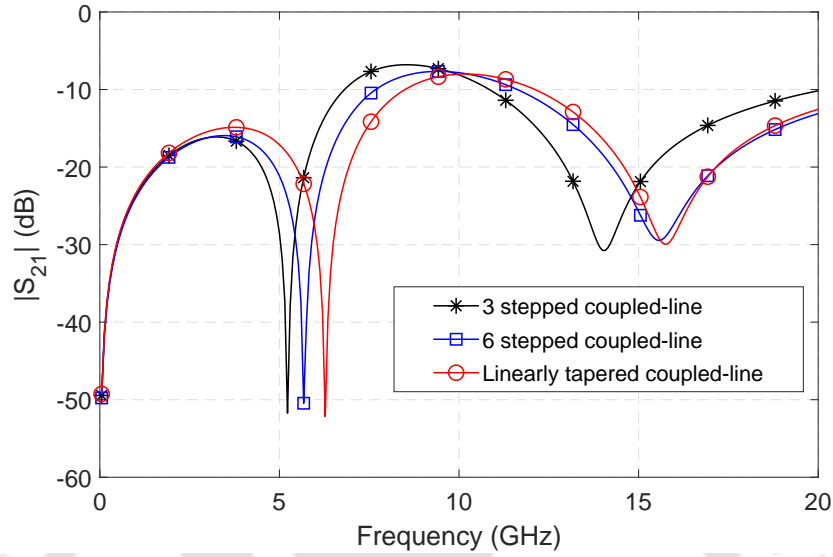


**Figure 3.14:** Simulated  $|S_{21}|$  of 3 stepped, 6 stepped and linearly tapered coupled-lines without open loop DGS.

loop DGS is etched on the ground, which further enhances performance of the filter.

Secondly, we have performed parametric study using EM simulations and varied the width  $w_3$  (see Figure 3.12(a)) from uniform width  $w_3 = w_2 = 0.86$  mm to tapered width  $w_3 = 4.45$  mm without open-loop DGS, and have observed their transmission response  $|S_{21}|$ , as shown in Figure 3.15(a). The broadening in bandwidth can be noticed when this quarter wavelength long coupled-microstrip line open-circuited stubs is linearly tapered towards open end of the line and reached maximum for  $w_3 = 4.45$  mm. It can also be seen from Figure 3.15(b) that by further tapering towards the open end or increasing the width  $w_3$  from 4.45 mm to 5.65 mm, the broadening in bandwidth towards the lower side of band became almost constant, and hence  $w_3 = 4.45$  mm is chosen as optimum value for the design.

Finally, the proposed filter is investigated by varying the gap width  $g$  and their frequency responses obtained from HFSS simulations are plotted in Figure 3.16. It can be seen from the transmission response  $|S_{21}|$  in Figure 3.16(a) that the filter exhibits a quasi-elliptic function filtering characteristic with two transmission zeros closer to each side of passband to enhance selectivity and one transmission zero at the upper side to improve upper stopband attenuation and its bandwidth. The location of transmission zeros can be controlled by varying the gap width. The smaller gap moves transmission zeros or attenuation poles towards the passband, resulting in a higher selectivity. This strongly

### 3. Linear tapers: analysis, design and applications

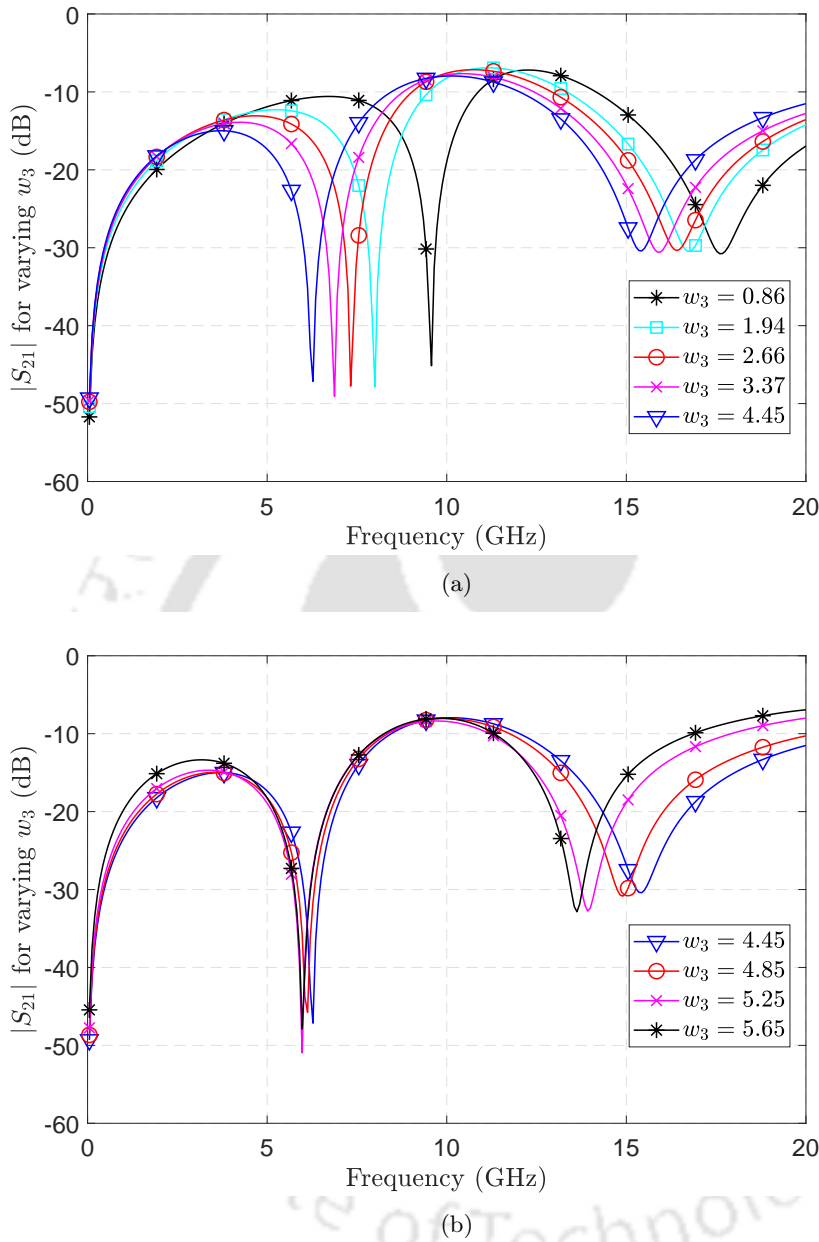
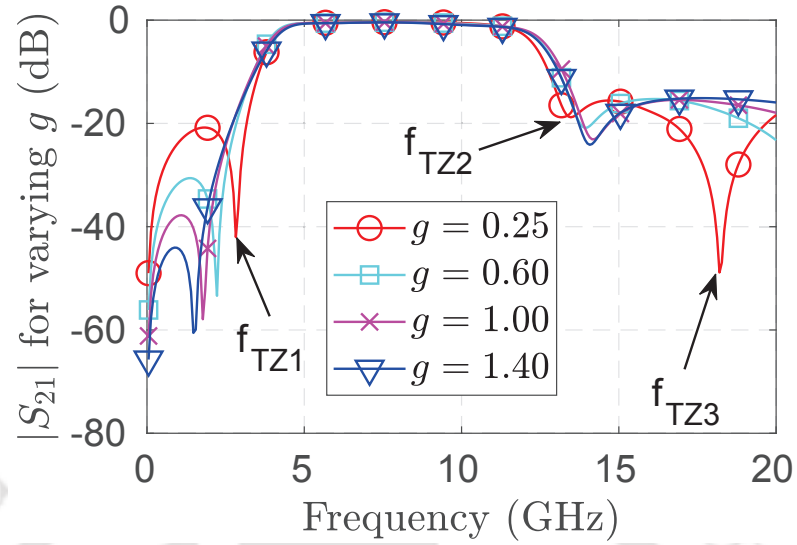
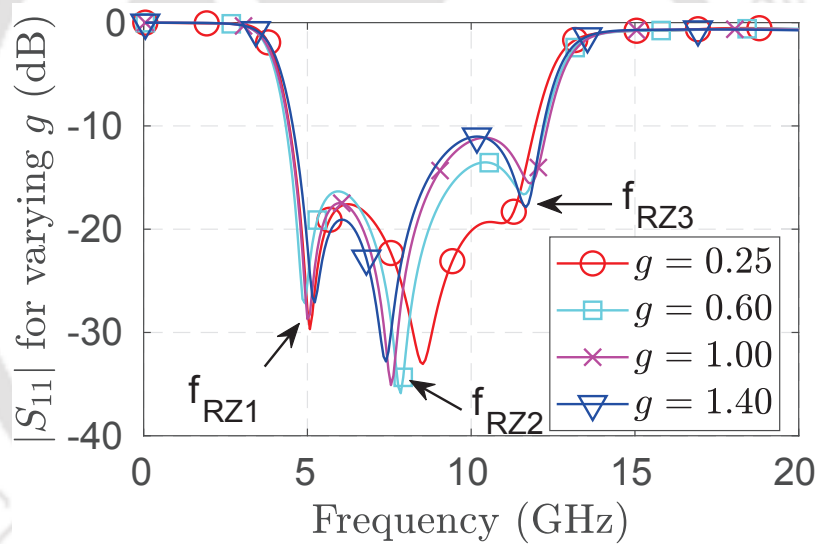


**Figure 3.15:** Simulated  $|S_{21}|$  for different tapered widths  $w_3$  in mm, without open loop DGS.

suggests that the finite-frequency transmission zeros could result from the cross-coupling between the linearly tapered coupled-microstrip open-circuited stubs and open loop DGS as well as between the input and output feed-lines. The effect of varying gap width on reflection response  $|S_{11}|$  is shown in Figure 3.16(b). Three transmission poles or reflection zeros (RZs) in passband of the filter can be observed by varying the gap width  $g$  from 0.25 mm to 1.4 mm, with best return loss in whole passband of the filter for  $g = 0.25$  mm. As an initial design,  $w$  and  $l$  can be chosen slightly less than  $\frac{c}{2f_r}$  and



(a)



(b)

**Figure 3.16:** Simulated S-parameters for different gap widths  $g$  in mm (with open loop DGS on the ground).

$\frac{c}{4f_r}$  respectively. Note that  $c$  is the speed of light in free space and  $f_r$  is the center frequency of the BPF which is also approximately equal to  $f_{RZ2}$ .  $l_1$  is slightly less than  $\frac{c}{4f_{TZ2}}$ . The length of open loop-DGS ( $2a + b + 2c$ ) can be also chosen slightly lesser than  $\frac{c}{f_{TZ3}}$ . The width of the taper  $w_3$  (in mm) can be calculated from  $f_{TZ1}$  (in GHz) as  $w_3 = 18.0967 - 6.2563f_{TZ1} + 0.5288(f_{TZ1})^2$ . The gap  $g$  (in mm) can be taken approximately as  $0.03f_r$ , where  $f_r$  is in GHz. The proposed design is simulated and examined using two different EM solvers (HFSS and CST microwave studio), as shown in Figure 3.17.

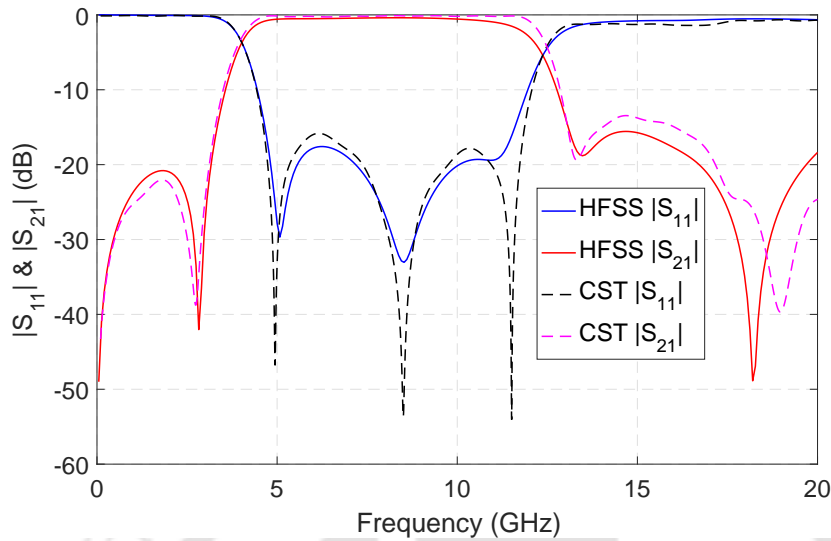


**Figure 3.17:** Simulated S-parameters (HFSS and CST) for the proposed ultra-broadband BPF.

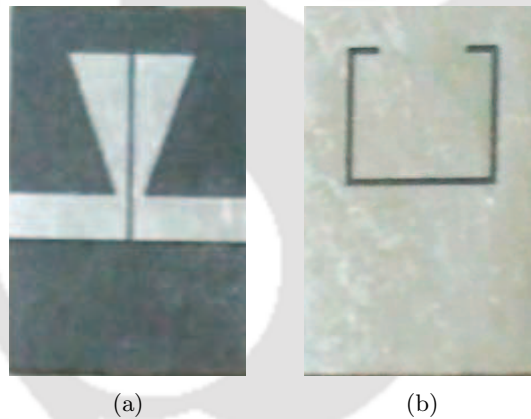


**Figure 3.18:** The photographs of fabricated prototype proposed BPF (a) Top view and (b) Bottom view.

#### 3.5.2 Implementation and experimental results

The proposed filter is implemented using the material and dimensions, as mentioned above. The fabricated prototype design is shown in Figure 3.18. The simulated and measured results are plotted in Figures 3.19 and 3.20, which validated the same. A slight shift in measured results and losses are incurred due to fabrication tolerances, some connector losses and frequency-dependent characteristic of dielectric material. It can be noted from the measured results that insertion loss is  $<1.5$  dB and return loss is  $>15$  dB in whole desired passband of the filter. The lower stopband attenuation is higher than 20 dB and the upper stopband attenuation is more than 13 dB upto 18 GHz, with a very good roll-off in both stopbands. The measured 10 dB return loss passband ranges approximately from 4.5

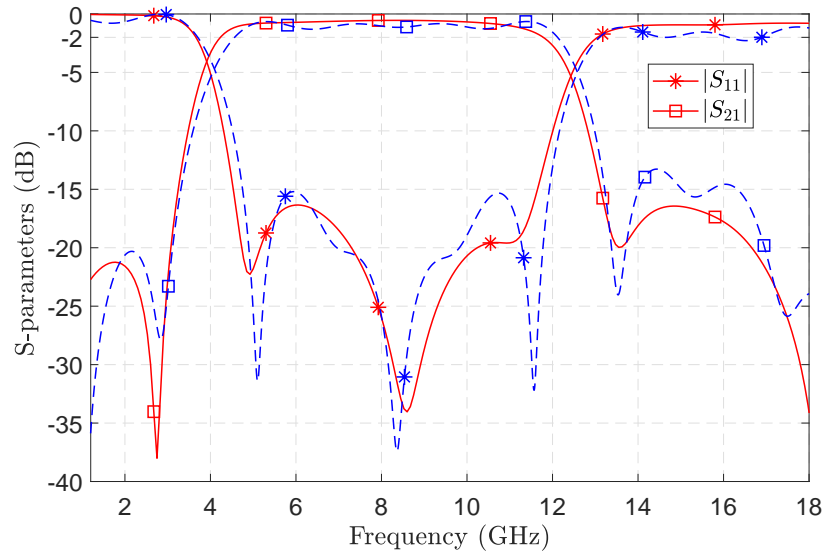


**Figure 3.19:** S-parameters of the proposed BPF (Solid lines represent simulated results and dashed lines represent measured results).

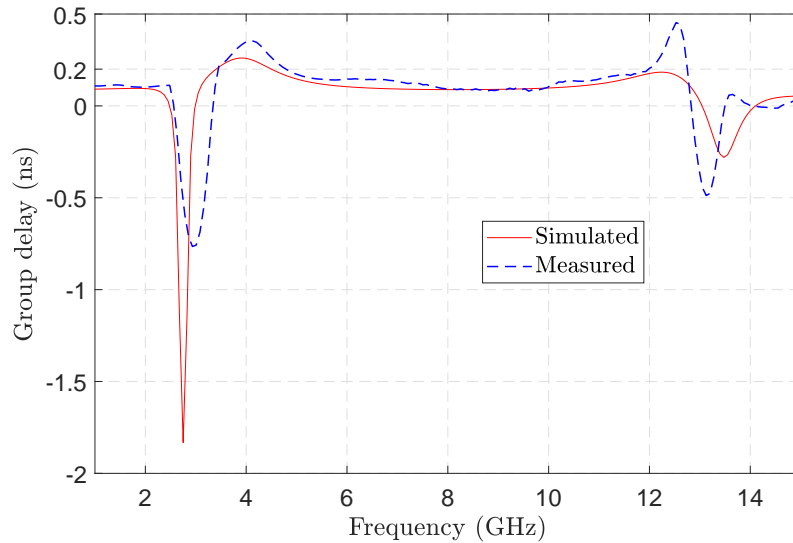


**Figure 3.20:** Group delay of the proposed BPF.

to 12 GHz with fractional bandwidth (FBW) of about 91%. The group delay variation is less than 0.2 ns in the whole passband, which is much better than [50] (0.4 ns). Upon using a DGS on the ground plane, which functions as a band stop filter, the upper stopband characteristics can further be improved as in [50]. However, the size of the filter might need to be increased, as in our case, the length of proposed filter is nearly half of the design proposed in [50]. The other wideband BPFs can be designed following this design method, like a filter for ultra-wideband (UWB) (3.1-10.6 GHz)

applications.

## 3.6 Summary

By using theory of small reflections, the reflection coefficient response for linear tapers have been derived and their response are compared with the other tapers. The linear tapers are very simple to design and easy to fabricate and hence have wide-range of applications such as impedance matching networks, filters, antennas, etc. Although linear width taper has been used in the design of several microwave devices, theoretical characterization of such taper is not available in the literature. In several cases, linear width taper has been taken as triangular taper. But triangular taper does not have linear width as depicted in Figure 3.4. The reflection coefficient response of linear impedance taper almost coincides with linear width taper which implies that their passband response remains the same and their response is very close to the exponential taper. However, in both cases, the minima occur at each multiple of  $\pi$  and their amplitude is gradually decreasing without reaching zero, unlike exponential taper. To match the impedance and field patterns, a linearly tapered line transition between the microstrip line and SIW component is designed, which exhibits RL of more than 22 dB and IL of less than 1 dB in whole X-band (8-12 GHz).

Also, an ultra-broadband BPF using quarter wavelength long linearly tapered coupled-microstrip line open-circuited stubs and open-loop DGS is presented. The proposed three-pole filter exhibits a quasi-elliptic response with two finite-frequency transmission zeros closer to each side of passband enhancing the selectivity and one at the upper side of stopband improving its attenuation and bandwidth. The filter size is  $0.20\lambda_g \times 0.26\lambda_g$  only at the center frequency of 8.25 GHz and achieved a wide 10 dB return loss passband from 4.5 to 12 GHz with fractional bandwidth (FBW) of about 91%. The insertion loss is less than 1.5 dB, and group delay variation is well below 0.2 ns within the passband of the filter. Both EM simulation and experiment show reasonable agreement between them.

# 4

## Broadband T-junction power dividers using linear taper

### Contents

---

4.1	Introduction . . . . .	60
4.2	Design and analysis . . . . .	61
4.3	Simulation and experimental results . . . . .	66
4.4	Summary . . . . .	72

---

## 4. Broadband T-junction power dividers using linear taper

---

In this chapter, T-junction power dividers using linearly tapered microstrip lines (MSLs) have been proposed; where the line to port 3 has also been tapered for achieving higher power dividing ratio between the output ports (ports 2 and 3). A method for approximate theoretical analysis of the power divider is developed. The simulated (HFSS and CST) and measured results of the power divider are in good agreement with each other, which show an average power dividing ratio of nearly 11 dB over a broad frequency range of 1.7-5 GHz. Also, a super wideband (SWB) power divider is designed, where the power dividing ratio of more than 10 dB in the whole SWB bandwidth of 0.5-6 GHz is achieved.

### 4.1 Introduction

Power dividers are the passive microwave components used in microwave systems for equal or unequal division of power into the output ports. Such components are commonly realized in the form of microstrip line (MSL) due to simple design, lower cost and easier fabrication. The T-junction power divider is a three-port network, which can be used as an equal or unequal division of power, like in antenna array design and some other applications. The power dividers like Wilkinson type, are most commonly used in the planar stripline or microstrip line technology. An ultra-broadband equal split tapered Wilkinson-type power divider has been developed in [19], and a broadband unequal multisection Wilkinson power divider with arbitrary power split ratio is presented in [59]. The disadvantage of Wilkinson dividers is that they require an additional component selection like resistor. T-junction power dividers with prescribed response characteristics and detailed theory have been presented in [18, 60–63], which can be used as an equal or unequal, narrowband and broadband T junction circuits. In many cases, T-junction power dividers are preferred to be used as an unequal power division where most of the power is desired in one of the output port and least power in the other output port over a very broad frequency range [18, 21, 22]. In [18], three distinct geometrical configurations of T-junctions have been realized: asymmetrical tee (narrowband circuit), 2-step tee and linearly tapered tee (broadband circuit). Different empirical models have been employed to realize these geometrical configurations but they do not provide much physical insight about the device operation.

Nowadays it is highly desirable to design a circuit which can operate in a system over a broad range of frequency for applications like in broadband, ultra-wideband or super-wideband systems. An analytical method has been developed in [21] to find the port parameters of exponentially tapered broadband T-junction power divider. This theoretical method can be employed to achieve power

dividing ratios from 2-10 dB over broad range of frequency. However, the cut-off wavelength definition adopted in this paper is incorrect and the analysis with correction has been presented in [22]. A uniform transmission line (UTL) has been used for output port-3 in [18, 21, 22], which further can be investigated for achieving even higher power dividing ratio between the output ports.

In this work, the transmission line to port 3 has also been tapered for achieving higher power dividing ratio of more than 10 dB over a very broad range of frequency. As it is evident from the previous chapter, the reflection coefficient response for linear taper is almost similar to exponential taper, where the minima in both cases occurs at each multiple of  $\pi$ . Also, the design and fabrication of linear taper is relatively easier than exponential taper. Hence, a T-junction power divider using linearly tapered MSLs has been proposed which exhibits power dividing ratio of more than 10 dB over a broad frequency range of 1.7-5 GHz. An approximate theoretical analysis of the linearly tapered power divider has also been developed; where each of linearly tapered lines are divided into N uniform lines and their ABCD parameters are found and subsequently S-parameters have been obtained [109]. The electromagnetic (EM) simulation of the power divider has been carried-out using two different EM solvers (HFSS and CST). The power divider is fabricated and measured for experimental verification of the predicted results. Furthermore, a super wideband (SWB) power divider is designed following the same procedure, where power dividing ratio of more than 10 dB in whole SWB bandwidth of 0.5-6 GHz is achieved.

## 4.2 Design and analysis

The proposed power divider design consists of three linearly tapered transmission lines as shown in Figure 4.1(a). The first two tapered sections are joined at the point where the characteristic impedance is lowest,  $Z_{\min}$  and at the same point the characteristic impedance of third tapered line is set to maximum,  $Z_{\max}$ . All ports are terminated with the system characteristic impedance of  $Z_0$ .

The equivalent model is shown in Figure 4.1(b). To analyze the model, we need to find the ABCD parameters of each sections first so that we can get the S parameters subsequently.

### 4.2.1 An approximate theoretical analysis

This section will describe an approximate theoretical analysis of the proposed power divider. It has been assumed that transmission lines are lossless and ignore the effects of step discontinuities at

#### 4. Broadband T-junction power dividers using linear taper

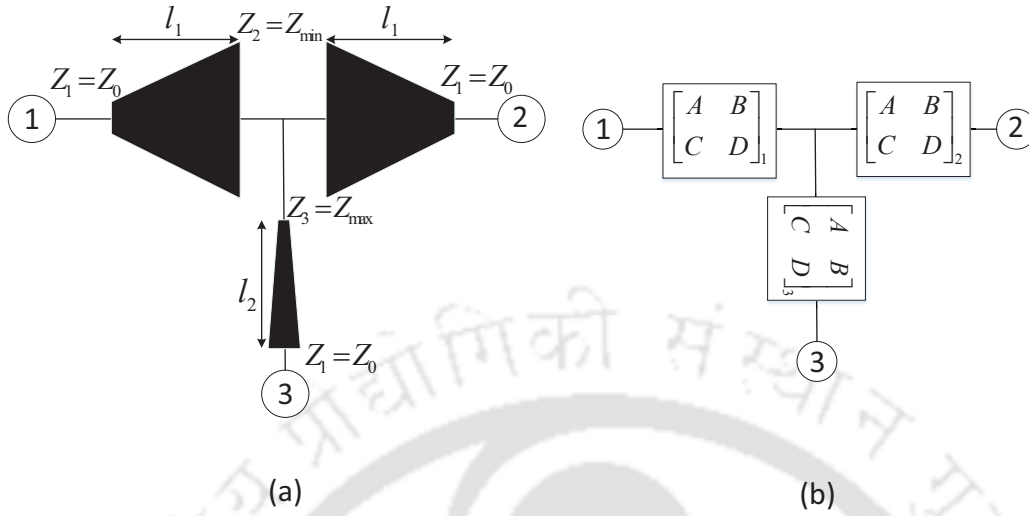


**Figure 4.1:** (a) Layout of the proposed unequal T-junction power divider and (b) Equivalence of (a) in terms of ABCD parameters of elementary block.

the junctions. The analysis model is shown in Figure 4.2, where each of the three linearly tapered lines are divided into  $N$  uniform transmission lines with small length of  $\Delta l_1$  and  $\Delta l_2$  ( $\Delta l_1 = l_1/N$  and  $\Delta l_2 = l_2/N$ ).

The ABCD matrix of a lossless uniform transmission line is given as [2]

$$\begin{bmatrix} A & B \\ C & D \end{bmatrix} = \begin{bmatrix} \cos(\beta l) & jZ_0 \sin(\beta l) \\ j\frac{\sin(\beta l)}{Z_0} & \cos(\beta l) \end{bmatrix} \quad (4.1)$$

Hence, the ABCD matrix for  $i^{\text{th}}$  section in Figure 4.2 can be written as

$$[T_i] = \begin{bmatrix} \cos(\beta_i \Delta l) & jZ_{0i} \sin(\beta_i \Delta l) \\ j\frac{\sin(\beta_i \Delta l)}{Z_{0i}} & \cos(\beta_i \Delta l) \end{bmatrix} \quad (4.2)$$

where  $\Delta l = \Delta l_1$  or  $\Delta l_2$ ,  $Z_{0i}$  is the characteristic impedance of  $i^{\text{th}}$  uniform MSL element and  $\beta_i$  is their phase constant. They can be calculated using (1.5) & (1.3) as

$$Z_{0i} = \begin{cases} \frac{60}{\sqrt{\epsilon_{e,i}}} \ln \left( \frac{8h}{w_i} + \frac{w_i}{4h} \right) & \left( \frac{w_i}{h} \leq 1 \right) \\ \frac{120\pi}{\sqrt{\epsilon_{e,i}} [w_i/h + 1.393 + 0.667 \ln(w_i/h + 1.444)]} & \left( \frac{w_i}{h} \geq 1 \right) \end{cases} \quad (4.3)$$

$$\beta_i = \frac{2\pi}{\lambda_{e,i}} \quad (4.4)$$

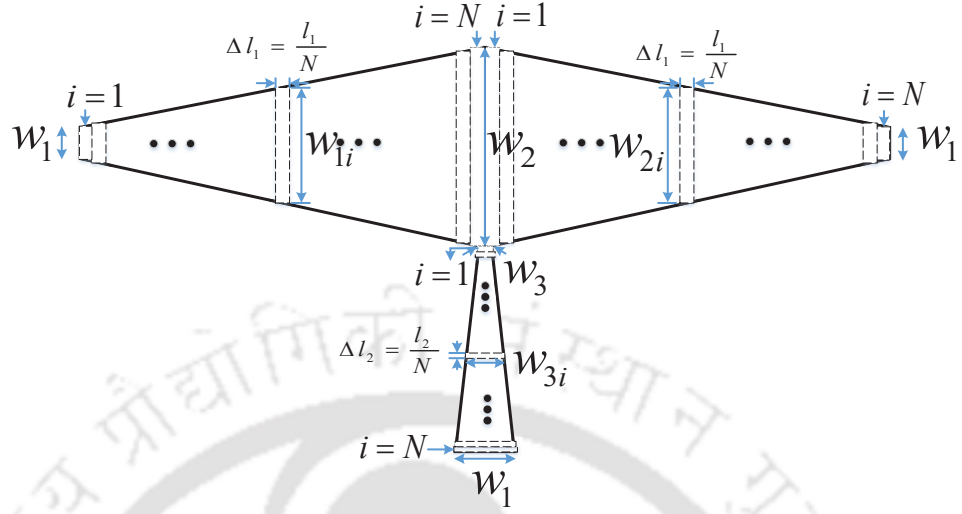


**Figure 4.2:** Analysis model of the design.

where  $h$  is thickness of the dielectric material,  $w_i$ ,  $\varepsilon_{e,i}$  and  $\lambda_{e,i}$  are the width, effective dielectric constant and guided wavelength of the  $i^{\text{th}}$  uniform MSL element respectively. The  $\varepsilon_{e,i}$  and  $\lambda_{e,i}$  can be expressed using (1.2) & (1.1) respectively as

$$\lambda_{e,i} = \frac{c}{f_0 \sqrt{\varepsilon_{e,i}}} \quad (4.5)$$

$$\varepsilon_{e,i} = \frac{\varepsilon_r + 1}{2} + \frac{\varepsilon_r - 1}{2} \frac{1}{\sqrt{1 + 12h/w_i}} \quad (4.6)$$

The width of  $i^{\text{th}}$  small uniform line  $w_i$  (for  $1 \leq i \leq N$ ) can be written in a linear function as

$$w_i = \begin{cases} w_{1i} = w_1 + \frac{(i-1)(w_2-w_1)}{(N-1)} \\ w_{2i} = w_2 - \frac{(i-1)(w_2-w_1)}{(N-1)} \\ w_{3i} = w_3 + \frac{(i-1)(w_1-w_3)}{(N-1)} \end{cases} \quad (4.7)$$

where  $w_{1i}$ ,  $w_{2i}$  and  $w_{3i}$  are the width of  $i^{\text{th}}$  small uniform line element of first, second and third linearly tapered MSL respectively, see Figure 4.2.  $w_1$ ,  $w_2$  and  $w_3$  are the width of corresponding impedances  $Z_0$ ,  $Z_{\min}$  and  $Z_{\max}$  respectively.

The ABCD matrices of left-side (1<sup>st</sup>), right-side (2<sup>nd</sup>) and middle (3<sup>rd</sup>) tapered MSL can be represented

#### 4. Broadband T-junction power dividers using linear taper

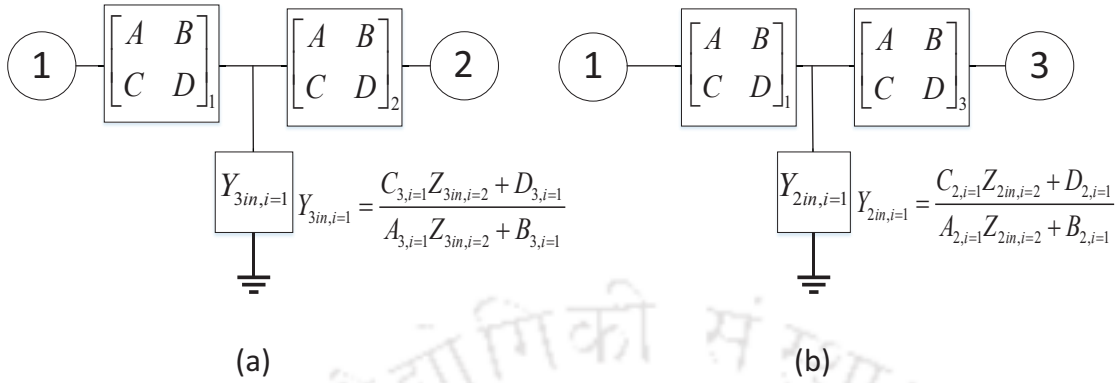


**Figure 4.3:** Equivalent 2-port network of Figure 1 when (a) Port-3 is terminated with the matched load  $Z_0$  and (b) Port-2 is terminated with the matched load  $Z_0$ .

using (4.8)-(4.10) as

$$\begin{bmatrix} A & B \\ C & D \end{bmatrix}_1 = [T]_L = [T_1]_1 [T_2]_1 \dots [T_i]_1 \dots [T_N]_1 \quad (4.8)$$

$$\begin{bmatrix} A & B \\ C & D \end{bmatrix}_2 = [T]_R = [T_1]_2 [T_2]_2 \dots [T_i]_2 \dots [T_N]_2 \quad (4.9)$$

$$\begin{bmatrix} A & B \\ C & D \end{bmatrix}_3 = [T]_M = [T_1]_3 [T_2]_3 \dots [T_i]_3 \dots [T_N]_3 \quad (4.10)$$

The input impedance of a uniform transmission line terminated with a load impedance  $Z_L$  can be obtained as [22]

$$Z_{in} = \frac{AZ_L + B}{CZ_L + D} \quad (4.11)$$

where A, B, C and D represent the ABCD parameters of the uniform transmission line.

The ABCD parameters between port-1 and port-2 of the power divider shown in Figure 4.1 can be obtained by terminating port-3 with matched load  $Z_0$ . The equivalent 2-port network for this case is shown in Figure 4.3(a). Their ABCD matrix can be expressed as

$$\begin{bmatrix} A & B \\ C & D \end{bmatrix}_{12} = \begin{bmatrix} A & B \\ C & D \end{bmatrix}_1 \begin{bmatrix} 1 & 0 \\ Y_{3in,i=1} & 1 \end{bmatrix} \begin{bmatrix} A & B \\ C & D \end{bmatrix}_2 \quad (4.12)$$

where

$$Y_{3in,i=1} = \frac{C_{3,i=1}Z_{3in,i=2} + D_{3,i=1}}{A_{3,i=1}Z_{3in,i=2} + B_{3,i=1}}. \quad (4.13)$$

The  $A_{3,i=1}$ ,  $B_{3,i=1}$ ,  $C_{3,i=1}$  and  $D_{3,i=1}$  represent the ABCD parameters of first small uniform line of third (or, middle) linearly tapered line, see Figure 4.2.  $Z_{3in,i=2}$  and  $Y_{3in,i=1}$  are the input impedance and input admittance of second and first small uniform line of third linearly tapered line respectively.  $Y_{3in,i=1}$  can be obtained following the technique explained here as: The tapered section ( $3^{rd}$ ) is divided into  $N$  small uniform sections with port-3 terminated with matched load  $Z_0$ . For  $i = N$ ,  $Z_L = Z_0$  and ABCD is found from (4.1) for a very small length uniform line  $\Delta l_2 = l_2/N$ . Using these ABCD parameters,  $Z_{in}$  for  $i = N$  can be obtained from (4.11) which in turn becomes  $Z_L$  for  $i = N - 1$ , and similarly  $Z_{in}$  for  $i = N - 1$  can be obtained. Finally, following these iterations we can obtain  $Z_{in}$  for  $i = 1$  and hence  $Y_{3in,i=1}$ .

Similarly, the ABCD parameters between port-1 and port-3 of the power divider shown in Figure 4.1 can be obtained by terminating port-2 with matched load  $Z_0$ . The equivalent 2-port network for this case is shown in Figure 4.3(b). Their ABCD matrix can be expressed as

$$\begin{bmatrix} A & B \\ C & D \end{bmatrix}_{13} = \begin{bmatrix} A & B \\ C & D \end{bmatrix}_1 \begin{bmatrix} 1 & 0 \\ Y_{2in,i=1} & 1 \end{bmatrix} \begin{bmatrix} A & B \\ C & D \end{bmatrix}_3 \quad (4.14)$$

where

$$Y_{2in,i=1} = \frac{C_{2,i=1}Z_{2in,i=2} + D_{2,i=1}}{A_{2,i=1}Z_{2in,i=2} + B_{2,i=1}} \quad (4.15)$$

which can be calculated following the above technique for  $Y_{3in,i=1}$ .

Finally, S-parameters can be obtained from ABCD parameters of (4.12) and (4.14) as [22]

$$S_{ii} = \frac{B_{ij} - Z_0^2 C_{ij} + Z_0 (A_{ij} - D_{ij})}{B_{ij} + Z_0^2 C_{ij} + Z_0 (A_{ij} + D_{ij})} \quad (4.16)$$

$$S_{jj} = \frac{B_{ij} - Z_0^2 C_{ij} - Z_0 (A_{ij} - D_{ij})}{B_{ij} + Z_0^2 C_{ij} + Z_0 (A_{ij} + D_{ij})} \quad (4.17)$$

$$S_{ji} = S_{ij} = \frac{2Z_0}{B_{ij} + Z_0^2 C_{ij} + Z_0 (A_{ij} + D_{ij})} \quad (4.18)$$

where  $i, j \in \{1, 2, 3\}$ . This process completes the analytical analysis of the model approximately.

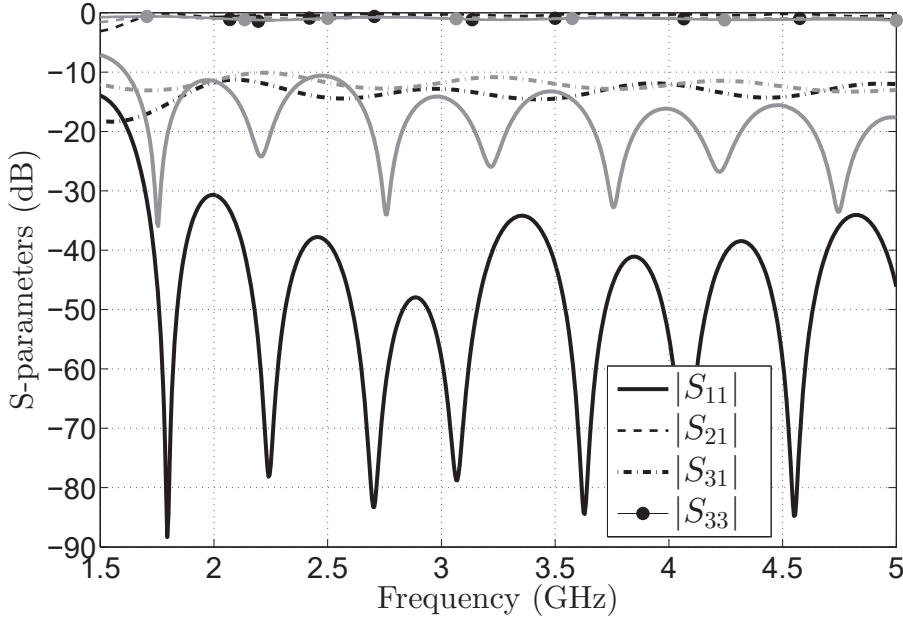


**Figure 4.4:** Theory and simulated S-parameters of the power divider. Black lines → theory & gray lines → HFSS results.

### 4.3 Simulation and experimental results

Using linearly tapered MSLs, a very broadband and unequal T-junction power divider has been designed and investigated. The model is designed using Rogers RO4350B substrate with a dielectric constant of 3.48, thickness of 0.762 mm and loss tangent of 0.0037. As it can be seen from Figure 3.5, the first minima or first null in accordance to first resonance frequency  $f_0$  in each case of linear and exponential taper occur at a half wavelength or electrical length of  $\pi$ . Hence, initially we can assume the length  $l_1$  for linearly varying transmission line same as of [22]

$$l_1 = \frac{c}{2f_0} \sqrt{1 + \left( \frac{\ln(Z_{\min}/Z_0)}{2\pi} \right)^2} \quad (4.19)$$

where  $c$  is the velocity of light. The first resonance frequency is chosen as  $f_0 = 1.7$  GHz and the characteristic impedance of each port as  $Z_0 = 50 \Omega$ , the lowest impedance as  $Z_{\min} = 9 \Omega$  and the maximum impedance of  $Z_{\max} = 115 \Omega$ . The initial value of length  $l_1$  using (4.19) is 91.5 mm and the final optimized length of each tapered lines are 84.88 mm ( $l_1 = l_2 = 84.88$  mm). The approximate theoretical results using (4.16)-(4.18) for the design are plotted using MATLAB and compared with HFSS results, as shown in Figure 4.4. The results show the power dividing ratio between the output ports (ports 2 and 3) of about 11.5 dB in whole broadband frequency range of 1.7-5 GHz. Note that

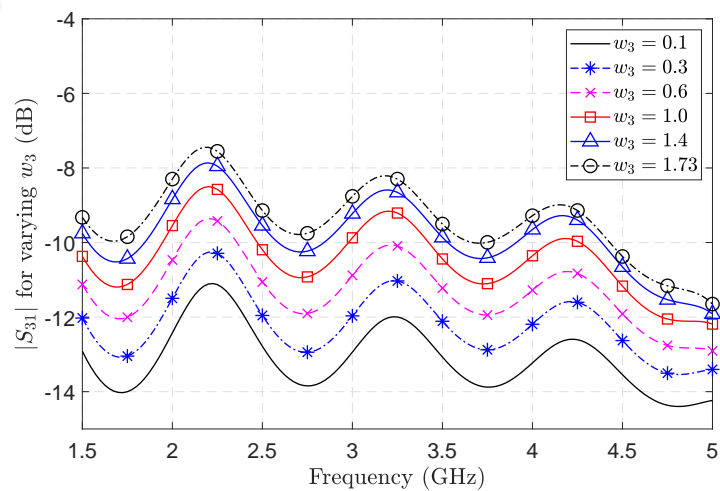
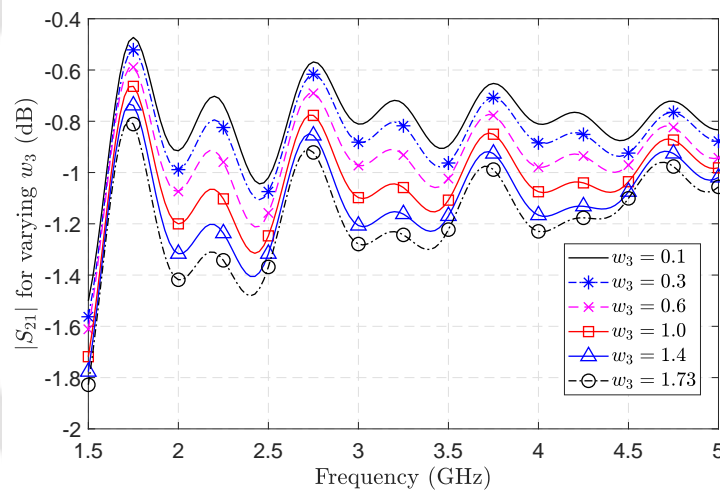
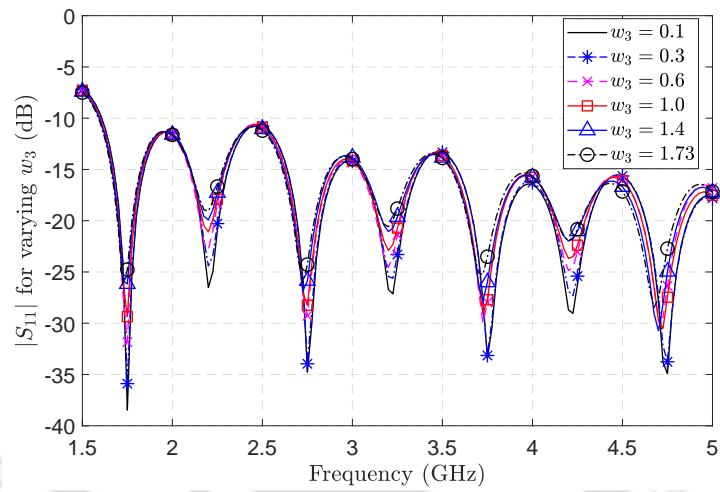
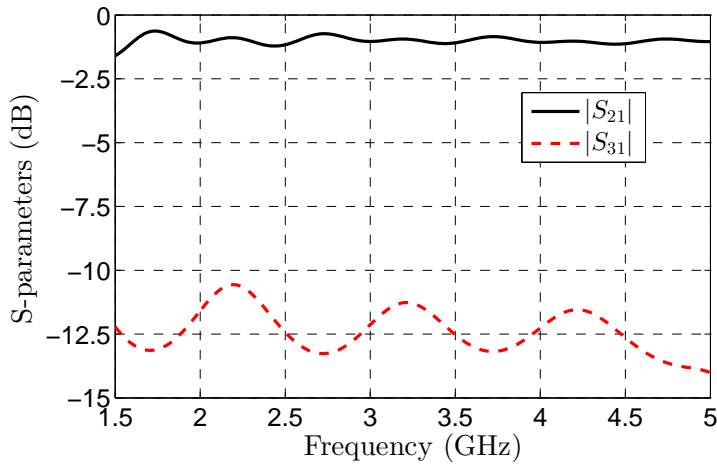
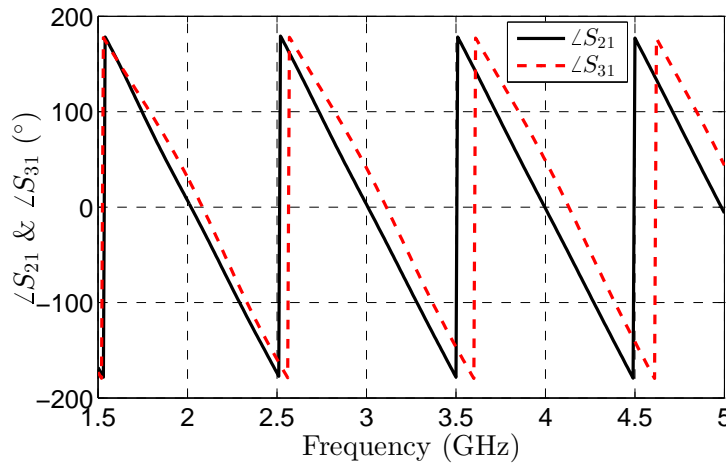


Figure 4.5: Simulated S-parameters of the power divider for varying  $w_3$  in mm.

#### 4. Broadband T-junction power dividers using linear taper



(a) Amplitude response

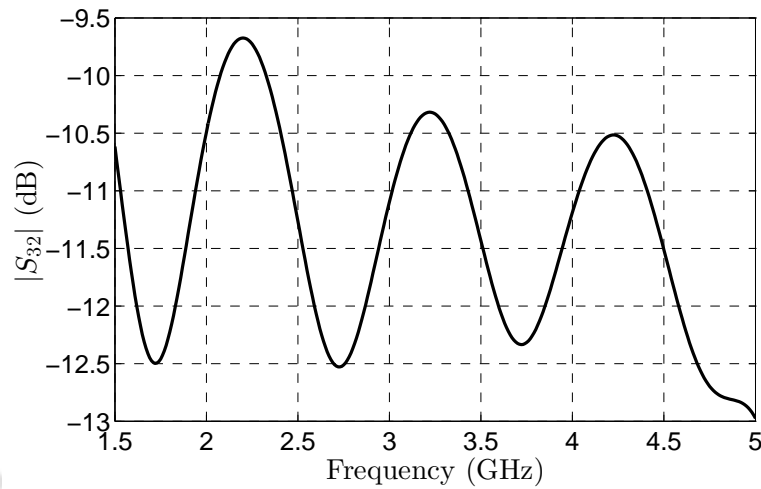


(b) Phase response

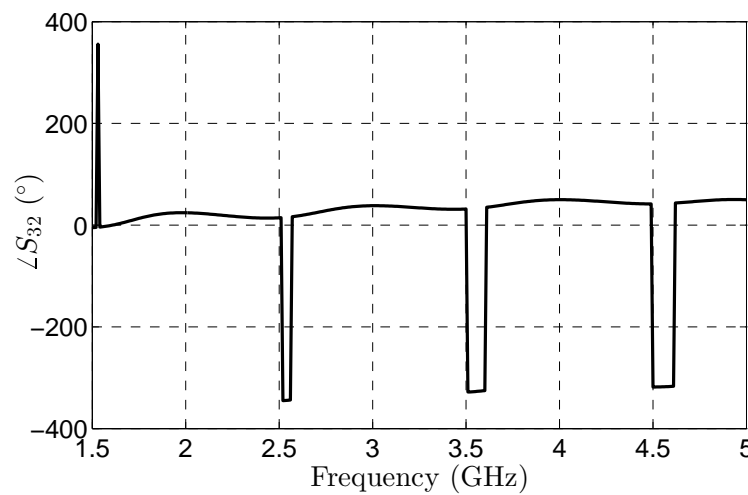
**Figure 4.6:** Simulated amplitude and phase response of  $S_{21}$  &  $S_{31}$  for the power divider.

we have assumed that transmission lines are lossless as well as ignored the dielectric and other losses in case of approximate theoretical analysis, hence there is some difference in the HFSS simulated and analytical results. But the reflection zeros are located at approximately same frequencies for both HFSS simulation and analytical results.

By using HFSS software, a parametric study of the design has been carried-out, in which the width of third transmission line at the junction is varied from 1.73 mm (for a uniform  $50 \Omega$  line) to 0.3 mm (for  $Z = Z_{\max} = 115 \Omega$ ) and their S-parameters have been observed as shown in Figure 4.5. It can be noted that the power dividing ratio ( $|S_{21}| - |S_{31}|$ ) is greatly improved when the rate of taper for the third line is increased towards the junction, without much affect on matching at port-1.



(a) Amplitude response



(b) Phase response

**Figure 4.7:** Simulated amplitude and phase response of  $S_{32}$  for the power divider.

Simulated amplitude and phase of  $S_{21}$ ,  $S_{31}$  and  $S_{32}$  for the power divider is plotted in Figures 4.6 and 4.7 respectively. It can be seen from Figure 4.6 that fluctuations in their amplitude response cause a slight shift in their phase response from each other, which have also been reported in unequal power dividers of very large bandwidth [18, 21, 22]. A sharp  $-360^\circ$  phase change at the frequencies such as 2.5, 3.5, 4.5 GHz etc. from the flat line in the phase response of  $S_{32}$  (see Figure 4.7(b)) is due to the sharp change in phase of  $S_{21}$  and  $S_{31}$  ( $-180^\circ - 180^\circ = -360^\circ$ ) at the corresponding frequencies, as shown in Figure 4.6(b).

The two EM simulations (HFSS and CST) of the design are plotted in Figure 4.8. The average

#### 4. Broadband T-junction power dividers using linear taper

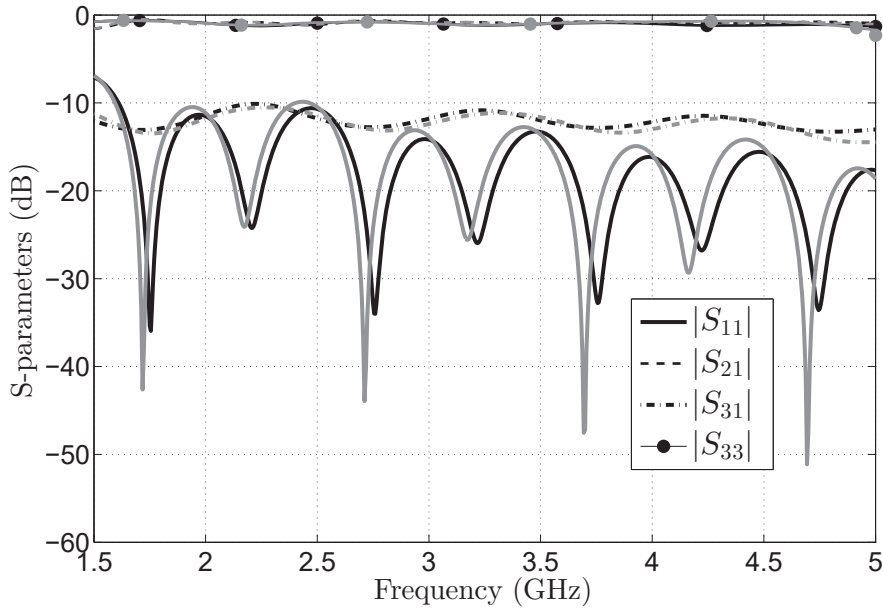


**Figure 4.8:** Simulated S-parameters of the power divider. Black lines → HFSS results and gray lines → CST results.

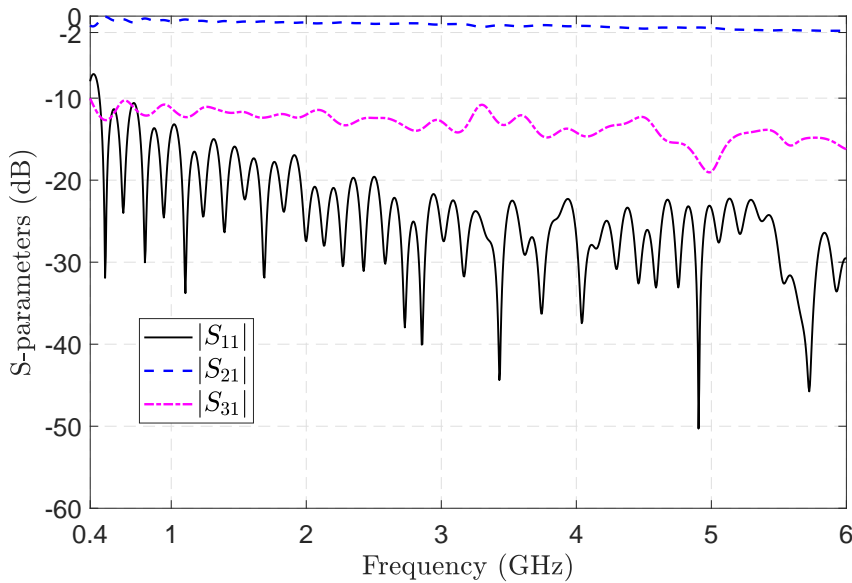


**Figure 4.9:** Simulated S-parameters of the SWB T-junction power divider.

power dividing ratio between the output ports are around 11.5 dB in whole frequency band of 1.7-5 GHz and both (HFSS and CST) results are in well agreement with each other which validate the same.

Furthermore, this technique can be extended to the design of SWB T-junction power divider, where the ratio bandwidth ( $f_H/f_L$ , highest to lowest frequency ratio) of more than 10:1 and a power



Figure 4.10: Photograph of the prototype fabricated T-junction power divider.

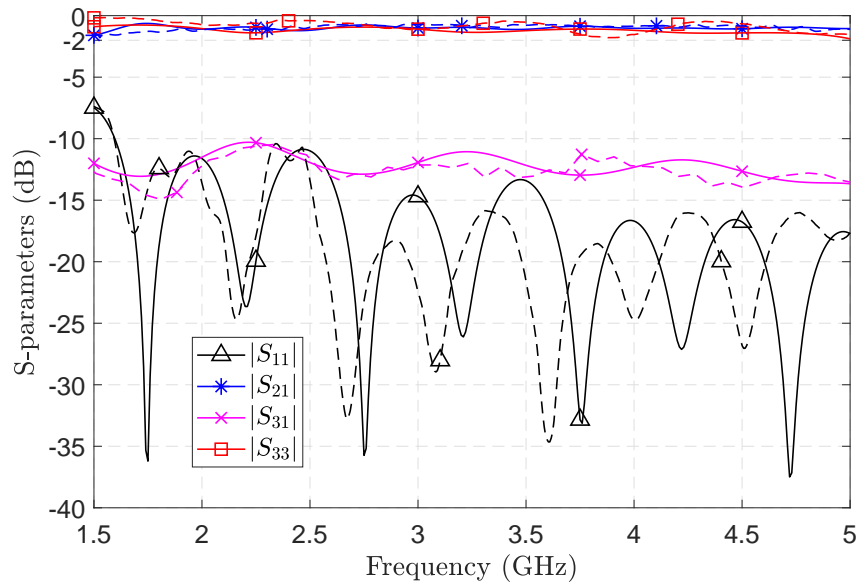


Figure 4.11: S-parameters of the T-junction power divider (Solid lines represent HFSS simulated results and dashed lines represent measured results).

dividing ratio of more than 10 dB simultaneously can be achieved. To design such a SWB power divider, here the first resonance frequency is chosen as  $f_0 = 500$  MHz ( $Z_0 = 50 \Omega$ ,  $Z_{\min} = 9 \Omega$  and  $Z_{\max} = 115 \Omega$ ). The optimized length of each tapered lines are 288.68 mm ( $l_1 = l_2 = 288.68$  mm). The simulated results for the design are plotted in Figure 4.9. The power dividing ratio is more than 10 dB in whole SWB bandwidth of 500 MHz to 6 GHz, which can be a good candidate for SWB applications.

A prototype model of the power divider for  $f_0 = 1.7$  GHz, has been fabricated and tested, as shown in Figure 4.10. The simulated and measured results of the design are plotted in Figure 4.11.

#### 4. Broadband T-junction power dividers using linear taper

---

**Table 4.1:** Performance comparison of the power divider with existing unequal T-junction power dividers

References	Power dividing ratio ( $ S_{21}  -  S_{31} $ ) (dB)	Frequency range (GHz)	Isolation (dB)	Size (Length $\times$ Width) ( $\lambda_0 \times \lambda_0$ )
[18]	<6	1-8	<6	0.20 $\times$ 0.086
[21]	9.3	1.75-3.5	9.3	0.57 $\times$ 0.086
[22]	6.5	1.7-5	6.5	0.96 $\times$ 0.566
This work	11	1.7-5	11	0.96 $\times$ 0.566

The average power dividing ratio between the output ports are around 11 dB in whole frequency band of 1.7-5 GHz and they are in well agreement with each other which validate the same. The third port can just only be used for reception or monitoring of the signal propagating between primary ports, the matching at port-3 is not of interest like in [18, 21, 22].

Table 4.1 shows the performance comparison of power divider with existing literature [18, 21, 22]. The first two lines in [18] are linearly tapered while in [21, 22], they are exponentially tapered and third line in each of them is considered of 50  $\Omega$  uniform line. As in our case, each of three lines are linearly tapered and hence a higher power dividing ratio has been achieved. Such a simple power divider design could be very useful for a passive signal cancelation in a system where coupling ratio of more than 10 dB are desired over a very broad range of frequency.

#### 4.4 Summary

An unequal T-junction power divider has been designed and tested where the line to port 3 has also been tapered linearly for achieving higher power dividing ratio of more than 10 dB over a broad frequency range of 1.7-5 GHz. An approximate theoretical analysis of the power divider has also been presented. It has been observed that a SWB unequal T-junction power divider can be designed by using the same method. For example, in this work a SWB power divider is designed which shows a power dividing ratio of more than 10 dB in whole SWB bandwidth of 0.5-6 GHz.

# 5

## Dual-port, aperture coupled and linearly tapered fed full-duplex antenna

### Contents

5.1	Introduction . . . . .	74
5.2	Antenna design . . . . .	76
5.3	Results and discussion . . . . .	78
5.4	Summary . . . . .	84

## 5. Dual-port, aperture coupled and linearly tapered fed full-duplex antenna

---

Dual-port, aperture coupled and linearly tapered fed patch antenna with high isolation is proposed for full-duplex 2.4 GHz ISM applications. Two different types of feeding mechanism are used in this antenna topology to excite dual polarization. One of the ports is excited by a quarter wavelength linearly tapered microstrip line feed to match the impedance between the port and edge of the patch smoothly and another by aperture coupled feeding technique to achieve better isolation between the ports. The proposed antenna can achieve a measured isolation of around 60 dB at 2.4 GHz and more than 59.5 dB in the band of 2.3-2.6 GHz.

### 5.1 Introduction

Full duplex radios allow simultaneous transmission and reception of signals with a single antenna. It has numerous advantages over the traditional Frequency division duplex (FDD)/ Time division duplex (TDD) radios like higher spectral efficiency. One of the major issues with in-band full duplex radios is the crosstalk of the transmitter and receiver ports when employing a single antenna. Single polarized antenna in full duplex communication system degrades the sensitivity of the system and does not able to discriminate between the transmitting and receiving signal. These issues can be addressed by employing dual polarized antenna which utilizes different polarization for transmitting and receiving signal. It also minimizes interference between transmitter and receiver. Low cross polarization of the antenna is achieved using orthogonal polarization for transmitting and receiving signal. To tackle the crosstalk between transmitter and receiver in a in-band full duplex radio, a dual-port antenna with high isolation between port 1 and port 2 can be employed. A lot of research works have been carried out to achieve low cross polarization and high isolation microstrip patch antenna employing different feeding mechanisms such as aperture-coupled feed, microstrip line feed or coaxial probe feed.

The aperture-coupled technique for feeding microstrip patch antennas is first proposed in [64], which consists two substrates separated with a common ground plane, where one substrate contains the radiating patch and the other substrate containing the feed network, with a small aperture in the ground plane, located under the patch. The numerical analysis of aperture-coupled microstrip patch antennas have been developed in [65,66]. Parametric study of their different feed sizes and aperture positions are performed in [67]. A design procedure following the parametric study of the critical antenna dimensions and other parameters is developed in [68], where the operating frequency, VSWR, percent bandwidth, polarization ratio, and broadside gain were observed for different configuration.

A dual-port, dual aperture-coupled and dual or circular polarized microstrip square patch antenna is proposed [69], where each aperture is coupled with the radiating patch to the two microstrip feed lines which are placed on the same side of the dielectric material. The similar approach is employed in [70], where dual slot-coupled microstrip circular patch antenna is developed for dual frequency operation.

Dual-port dual-polarized antennas with high isolation and low cross polarization are proposed in [75–78] for full-duplex 2.4 GHz ISM band applications. In [75], the dual orthogonal linear polarizations are generated by a new dual-hybrid-feed structure comprised of a pair of meandering strips with a phase difference of  $180^\circ$  and a full-wavelength annular-ring coupling slot. The isolation between the two feeding ports is below 40 dB over a 10 dB input impedance bandwidth of 14%. Following the similar approach, a simple antenna structure with a wide input impedance bandwidth (23.25% for Port 1 and 35% for Port 2) and ports isolation of better than 40 dB is presented in [76]. A dual linearly polarized aperture coupled patch antenna with dual ports of good impedance matching and ports isolation of 35 dB over the desired band is proposed in [77] for RFID ISM band (2.4-2.48 GHz) applications. The antenna uses four symmetric coupling apertures to excite two orthogonal modes for dual polarized operation. The dimensions and offset position of the apertures are optimized to achieve the better isolation and return loss in the desired band. A dual-polarised patch antenna utilising a modified ring hybrid feeding structure is presented in [78] for in-band full-duplex systems. The isolation between the ports is better than 50 dB in the band of 2.4-2.5 GHz with a centre frequency of 2.45 GHz. A method to prevent the degradation in the isolation between the orthogonal polarization ports caused by beam forming network routing in combined edge/aperture fed dual-polarized microstrip-patch planar array antennas is proposed in [80]. The ports isolation of 50 dB at the center frequency, and better than 40 dB over a 4% input impedance bandwidth is achieved. A coax-feed dual-polarised patch antenna with low cross-polarisation and high port-to-port isolation of more than 40 dB in the whole bandwidth is presented in [82] for WiMAX applications. An ACS-fed dual-band antenna for 2.4/5.8 GHz WLAN applications have been proposed in [84], which size is very compact and has omnidirectional radiation patterns. Diplexer with high isolation [110] is used in conjunction with a single antenna for transmission and reception of radio signals. But the transmission and reception frequency bands are different. Isolation improvements for patch antenna are reported in [111, 112]. But such isolation improvements are meant for reducing mutual coupling in antenna arrays.

In this chapter, we present a dual-port microstrip patch antenna whose port 1 is aperture coupled

## 5. Dual-port, aperture coupled and linearly tapered fed full-duplex antenna

---

fed and port 2 is linearly tapered fed. Such a compact antenna can achieve maximum measured isolation of 67.5 dB around 2.3 GHz. It has measured isolation more than 59.5 dB in the frequency band of 2.3-2.5 GHz. This antenna can be used for full duplex ISM operations.

### 5.2 Antenna design

The configuration of the proposed antenna is shown in Figures 5.1(a) and 5.1(b). As it can be seen from Figure 5.1(a) that the two different types of feeding mechanism are used in this antenna topology to excite dual polarization; port 1 is excited by a quarter wavelength linearly tapered microstrip line feed to match the impedance between the port and edge of the patch smoothly and port 2 by aperture coupled feeding technique which exhibits reduced transmission line radiation, enhanced antenna radiation and better co- to cross-pol performances. Note that we have not used inset fed microstrip antenna since the cross-pol components would be higher for such feed lines. For edge fed antenna, the antenna impedance at the edge is much higher than  $50 \Omega$ , which need to be transferred to  $50 \Omega$  impedance at the port end for impedance matching, in order to perform the measurement using SMA connectors. Hence, a linearly tapered feed line has been used for matching such a high impedance at the edge to  $50 \Omega$  line as shown in Figure 5.1. Basically two orthogonal polarizations are excited viz. horizontal and vertical polarizations for better isolation. Besides, the two feedlines are separated by two ground planes of the two FR4 boards. As usual, ground plane reflects the wave incident on it. Double ground planes of two FR4 boards will reflect even better than a single ground plane; therefore high isolation between the ports can be achieved.

The antenna is designed using FR4-epoxy substrate with a dielectric constant of 4.4, loss tangent of 0.02 and thickness of 1.6 mm. The dimensions of the antenna are  $L = 60$  mm,  $W = 62$  mm,  $L_p = 26.5$  mm,  $W_p = 29$  mm,  $L_f = 42.75$  mm,  $L_t = 12$  mm,  $W_{f1} = 3$  mm,  $W_{f2} = 3$  mm and  $W_{f3} = 1$  mm. The slot length and width are chosen as  $L_s = 13$  mm and  $W_s = 0.9$  mm respectively. Layer by layer illustration of the proposed antenna is shown in Figure 5.1(b). From bottom to top, the layers are: microstrip feed line (1<sup>st</sup> layer), FR4 substrate (2<sup>nd</sup> layer), ground planes 1-2 with slot (3<sup>rd</sup> layer), FR4 substrate (4<sup>th</sup> layer) and radiating patch with microstrip feed line (5<sup>th</sup> layer). The fabricated prototype of the antenna is shown in Figure 5.1(c). Since there are two FR4 layers, the total thickness of the proposed antenna is 3.2 mm. This antenna is very compact and its overall size amounts only  $60 \times 62 \times 3.2$  mm<sup>3</sup>. The full wave simulator HFSS is used to design and simulate the proposed antenna.

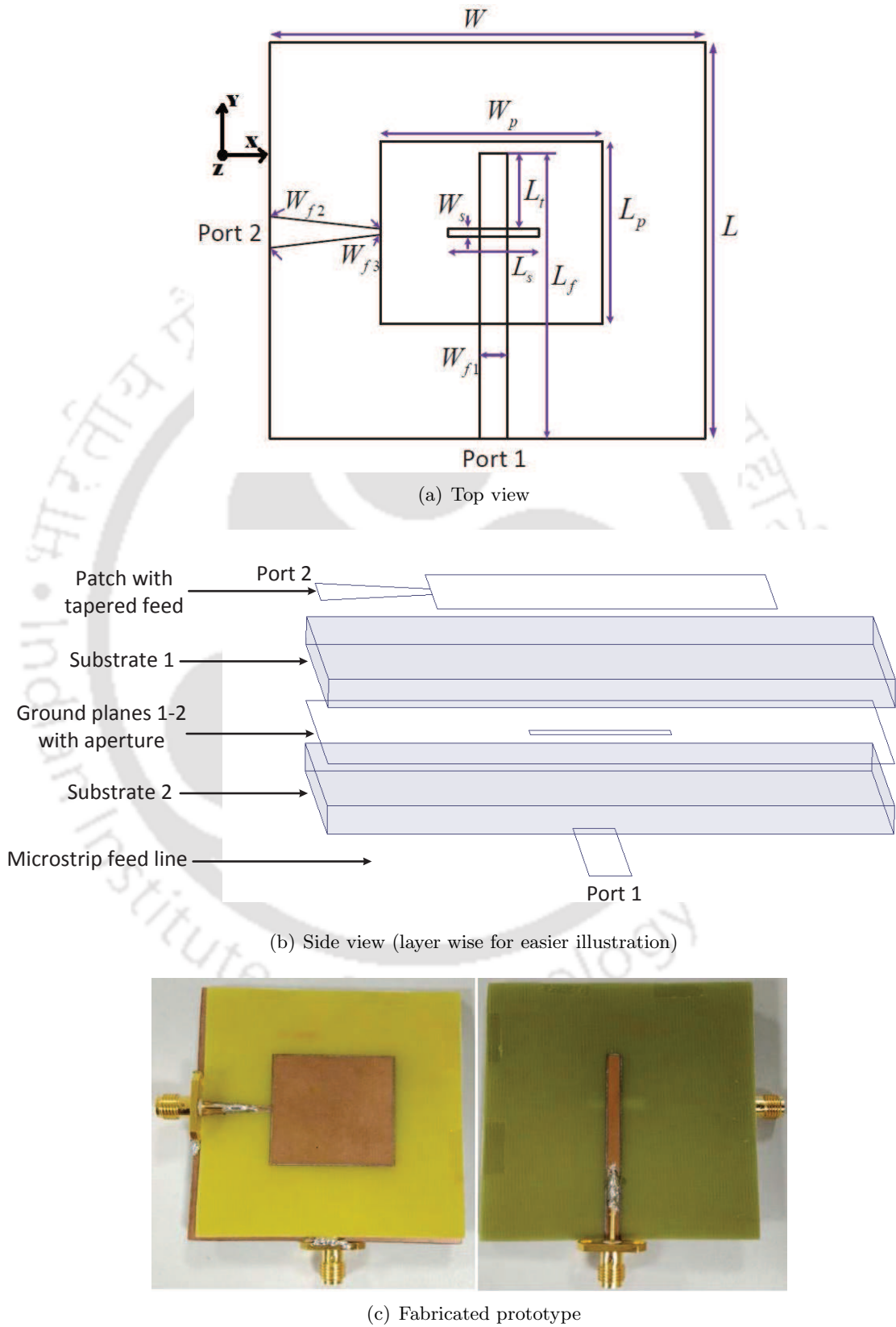


Figure 5.1: Geometry of the proposed antenna.

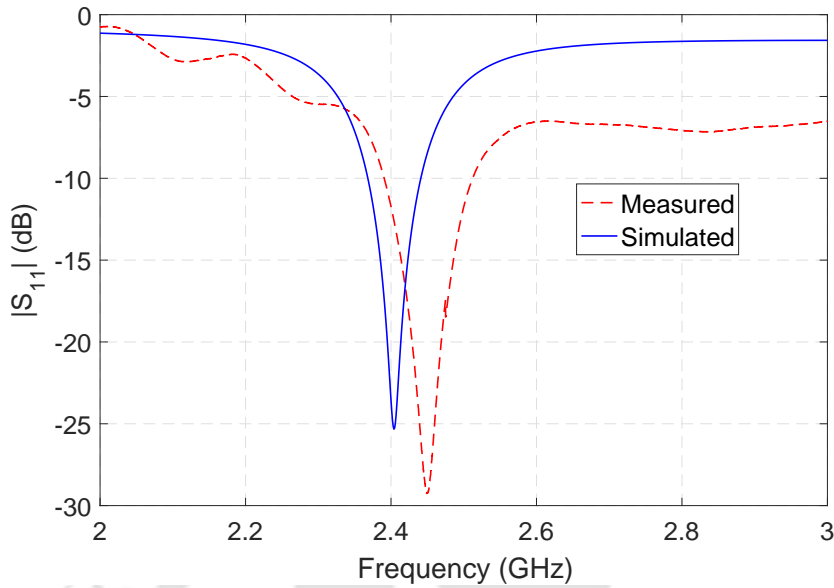


Figure 5.2:  $|S_{11}|$  vs frequency of dual-port patch antenna.

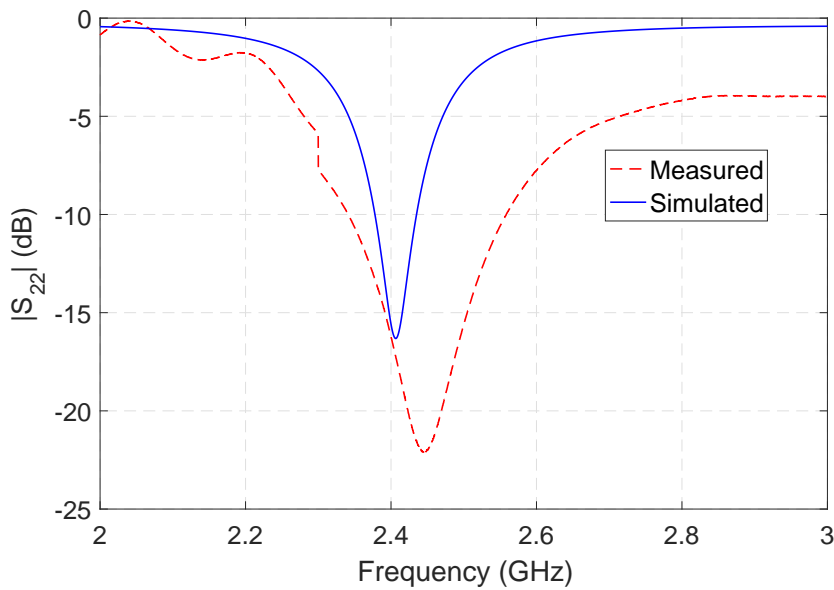
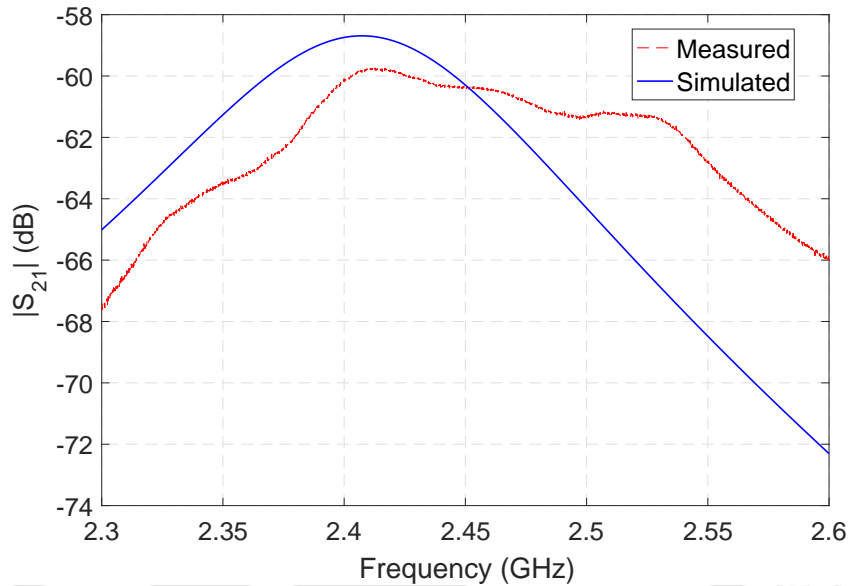


Figure 5.3:  $|S_{22}|$  vs frequency of dual-port patch antenna.

### 5.3 Results and discussion

The HFSS simulated and measured frequency response of dual-port patch antenna,  $|S_{11}|$  and  $|S_{22}|$ , are plotted in Figures 5.2 and 5.3 respectively. The measured 10 dB bandwidth for  $|S_{11}|$  and  $|S_{22}|$  are approximately 2.4-2.5 GHz and 2.33-2.55 GHz respectively. There is a minor frequency shift

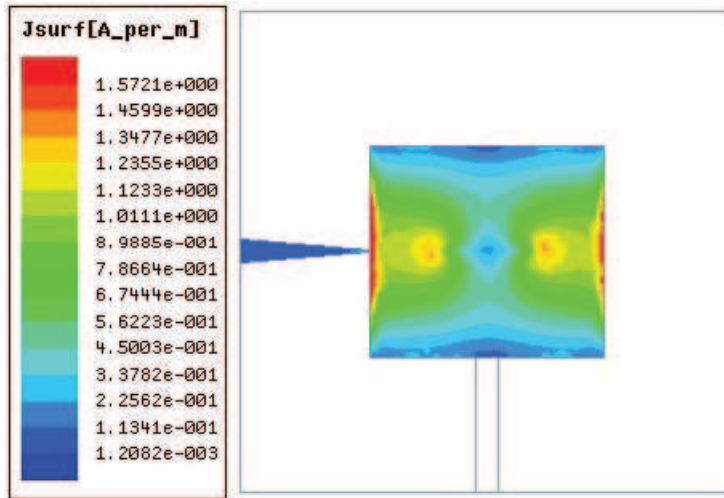


**Figure 5.4:**  $|S_{21}|$  vs frequency of dual-port patch antenna.

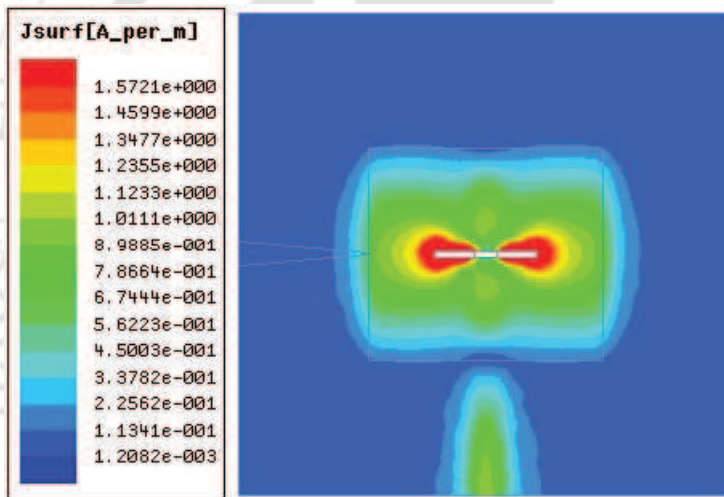
between the HFSS simulated and measured results. This is mainly due to imprecise calibration set-up for measurement, connector losses and fabrication tolerances which were not included in the HFSS simulation. Besides, the ground plane size has been slightly increased in order to connect the SMA connectors to the two ports (see Figure 5.1(c)).

The measured and HFSS simulated results of  $|S_{21}|$  vs frequency is shown in Figure 5.4. There are some difference between the simulation and experimental results. Such differences are due to measurement performed in a real laboratory environment, where interference from nearby signals, reflections and scattering from surroundings and addition of ambient noises which are more pronounced at such low values of  $|S_{21}|$  as also reported in [75], which cause a rapid variations in their amplitude. The measured ports isolation ( $|S_{21}|$ ) is greater than 59.5 dB from 2.3 to 2.6 GHz which is suitable for ISM band antennas for full duplex operations. The maximum measured isolation ( $|S_{21}|$ ) is 67.5 dB at 2.3 GHz.  $|S_{12}|$  vs frequency has very similar performance. The surface current distributions at all three metallic surfaces upon excitation of Ports 1 and 2 at 2.4 GHz are shown in Figures 5.5 and 5.6 respectively. It is obvious from these patterns that the current maxima appear in a mutually orthogonal direction upon excitation of Port 1 and Port 2 confirming the excitation of horizontal and vertical polarization. This is the reason for high isolation between the ports. For port 1, E-plane, H-plane and for port 2, E-plane, H-plane radiation patterns (both simulation and experimental) of the dual-port

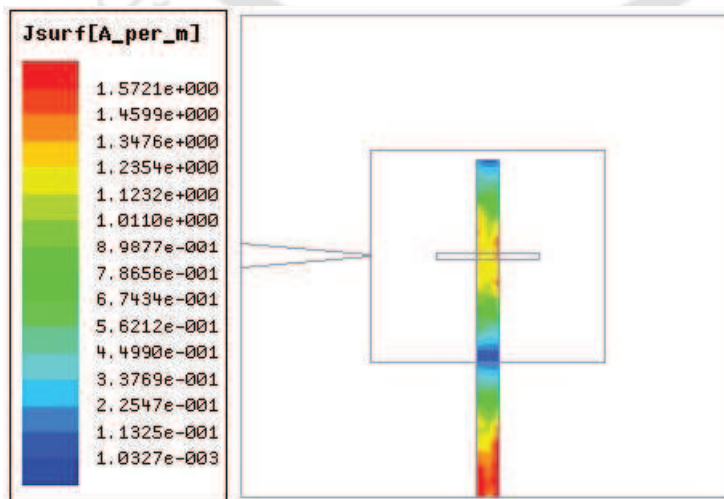
5. Dual-port, aperture coupled and linearly tapered fed full-duplex antenna



(a) Top

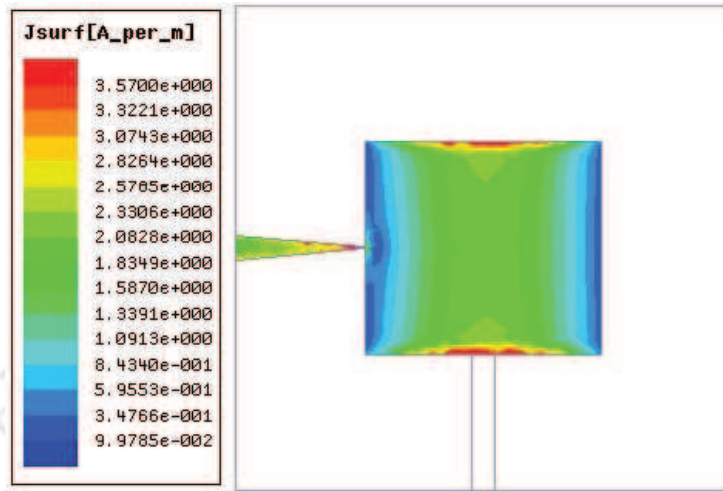


(b) Ground

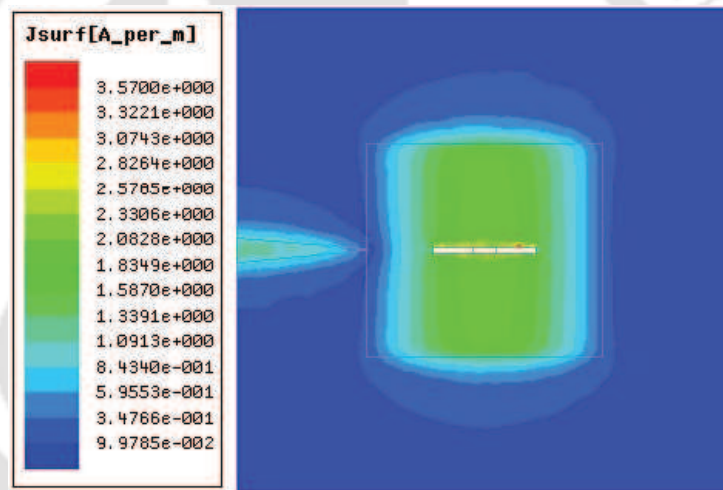


(c) Bottom

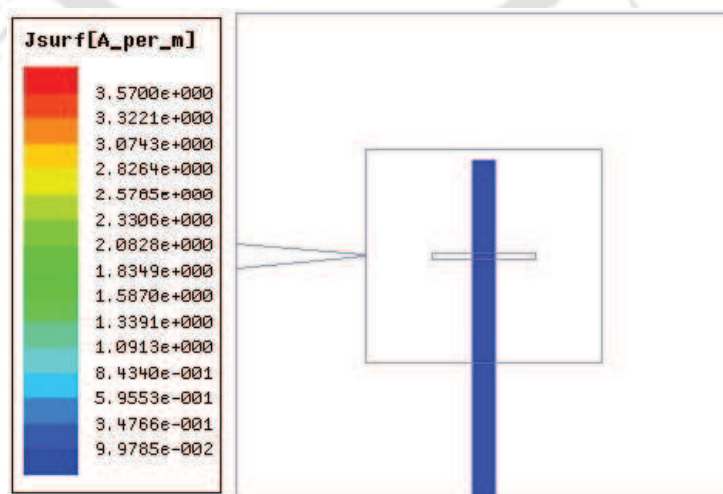
Figure 5.5: Surface current distributions at all three metallic surfaces when Port-1 is excited.



(a) Top



(b) Ground



(c) Bottom

Figure 5.6: Surface current distributions at all three metallic surfaces when Port-2 is excited.

5. Dual-port, aperture coupled and linearly tapered fed full-duplex antenna

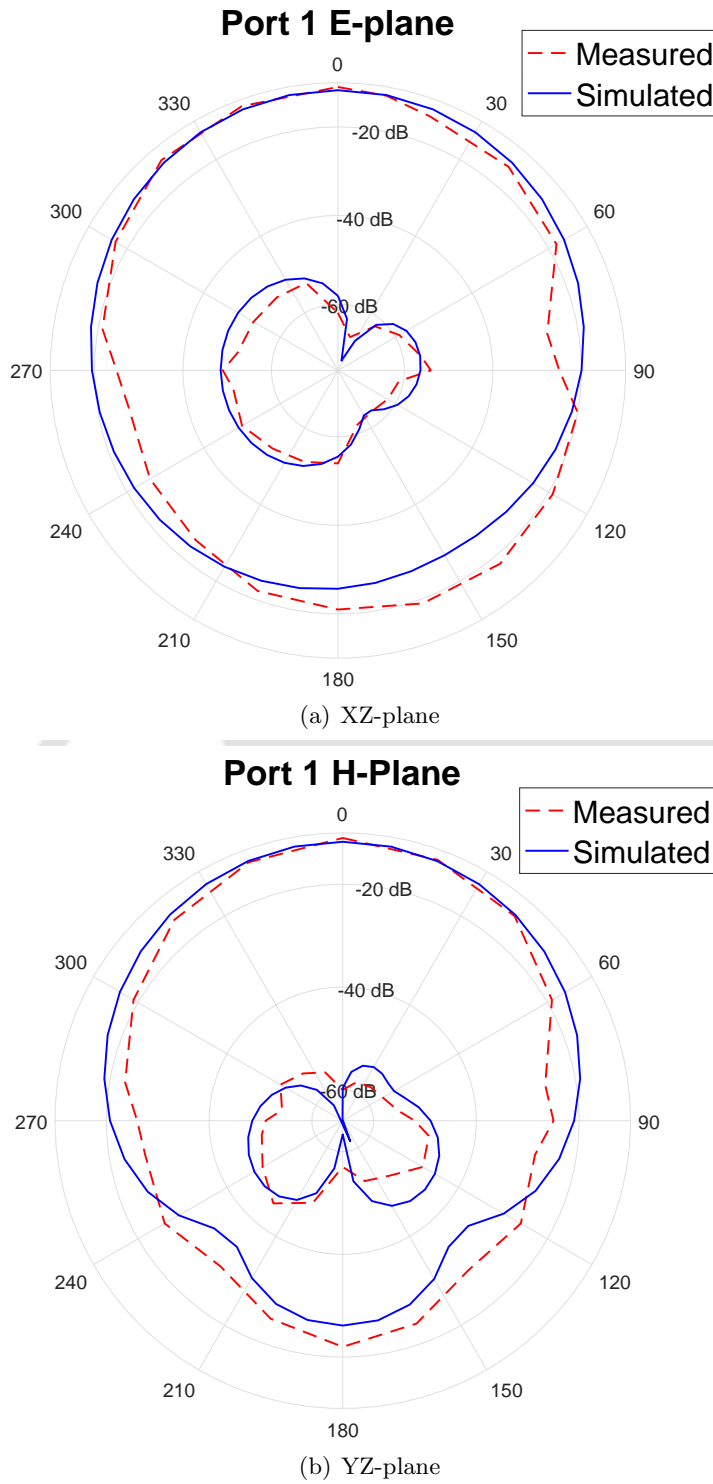
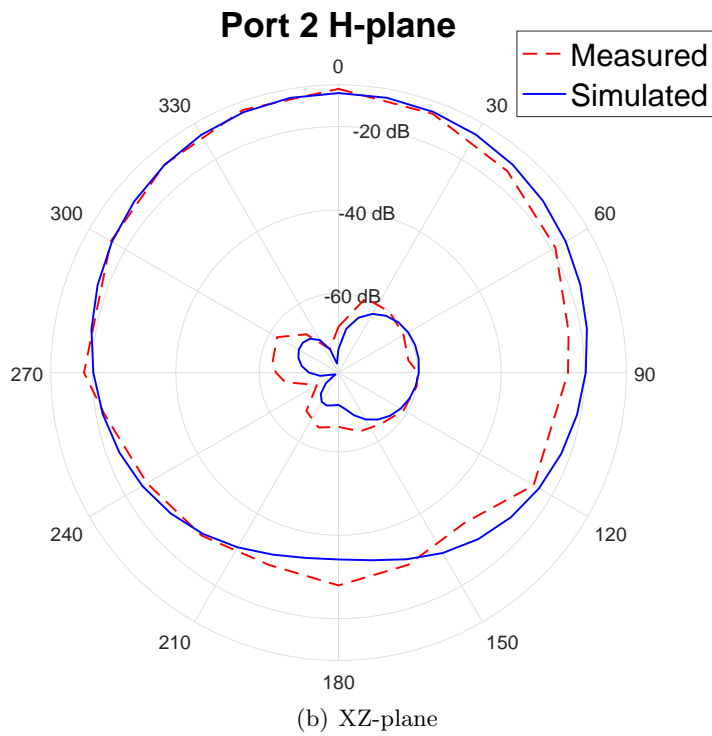
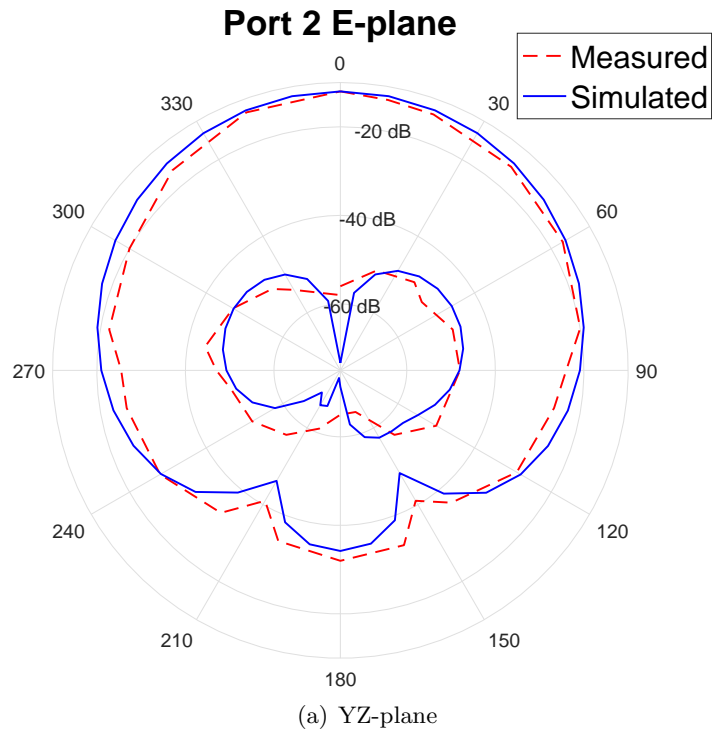


Figure 5.7: Radiation pattern (port 1) of the dual-port patch antenna at 2.4 GHz.

antenna at 2.4 GHz are shown in Figures 5.7(a), 5.7(b) and Figures 5.8(a), 5.8(b) respectively. It can be seen that co-polar radiation patterns are mostly oval in shape and the cross-polar components are



**Figure 5.8:** Radiation pattern (port 2) of the dual-port patch antenna at 2.4 GHz.

well below  $-40$  dB for all of the above cases. Hence, the cross-polarization components are sufficiently low. The experimental and simulation results are well agreement with each other.

## 5. Dual-port, aperture coupled and linearly tapered fed full-duplex antenna

---

**Table 5.1:** Performance comparison (experimental) of the proposed antenna with the antennas available in the literature

References	Matching band (RL > 10 dB)	Isolation Band	Maximum Isolation	Size
[77]	2.33-2.52 GHz	2.34-2.5 GHz (isolation > 28 dB)	42 dB at 2.4 GHz	$80 \times 80 \times 5.1 \text{ mm}^3 = 32,640 \text{ mm}^3$
[82]	2.15-2.72 GHz	2.15-2.72 GHz (isolation > 40 dB)	50 dB at 2.4 GHz	$120 \times 120 \times 25 \text{ mm}^3 = 3,60,000 \text{ mm}^3$
This work	2.4-2.5 GHz	2.3-2.6 GHz (isolation > 59.5 dB)	67.5 dB at 2.3 GHz	$60 \times 62 \times 3.2 \text{ mm}^3 = 11,904 \text{ mm}^3$

Table 5.1 compares the performance of the proposed dual-port antenna with antennas available in the literature in terms of matching band ( $|S_{11}| < -10$  dB), isolation band, maximum isolation and size. It can be seen that the proposed antenna can achieve the best isolation in terms of maximum isolation and isolation band. Besides, the size of the proposed antenna is much smaller than the other reported antennas. It may be noted all the antennas compared in Table 5.1 are fabricated on FR4 substrate. Hence the comparison of size is fair.

### 5.4 Summary

A dual-port, orthogonal polarized patch antenna with high isolation and low cross polarization has been designed, fabricated and tested. This antenna can achieve a maximum isolation of 67.5 dB at 2.3 GHz and more than 59.5 dB in the band of 2.3-2.6 GHz. Such a simple and compact antenna can be efficiently used for in-band full-duplex ISM operations. The same antenna geometry with the two feed lines (tapered feed and aperture coupled feed) can be tuned and used for designing antennas for in-band full-duplex radios such as for WiMAX applications.

# 6

## Filters design using SIW, SSPP and linear taper

### Contents

---

6.1	Iris SIW bandpass filter for V-band applications . . . . .	86
6.2	Hybrid SSPP-SIW bandpass filters for X-band applications . . . . .	92
6.3	Comment on “ [1]” . . . . .	107
6.4	Summary . . . . .	109

---

This chapter presents the approximate design equation for iris width calculation of iris substrate integrated waveguide (SIW) bandpass filter. The design equation has been derived by using curve fitting technique followed by de-embedding method. It is valid for designing narrowband iris SIW bandpass filter whose fractional bandwidth (FBW) should not be more than 10%. A generalized procedure has been presented to calculate the inverter parameters of the iris window and a design equation is developed at 60 GHz for its validation. The theoretical and calculated normalized reactance values are in good agreement. An iris SIW bandpass filter at 60 GHz has also been designed using the same procedure.

Two bandpass filters based on hybrid spoof surface plasmon polariton (SSPP) and substrate integrated waveguide (SIW) has been proposed for X-band applications. The dispersion and transmission characteristics of the proposed hybrid SSPPs-SIW structures are analyzed, and influence on the variation of their structural parameters are investigated. The proposed dumbbell-shaped SSPP shows more slow-wave effects than rectangle-shaped SSPP for the same height of grooves, and hence could be a good choice in the design of compact, low loss and highly integrated microwave and terahertz devices. The lower and upper cutoff frequencies of hybrid SSPP-SIW bandpass filters can be adjusted independently by varying the structural parameters of SIW and SSPP units, respectively. The proposed two filters exhibit excellent passband (8-13.15 GHz for filter I & 8-13.5 GHz for filter II) and wide upper-band rejection (>42.5 dB from 14.1-20 GHz for filter I & >41 dB from 14.2-19.5 GHz for filter II) simultaneously. Their size are very compact, amounts to only about  $1\lambda_g \times 0.7\lambda_g$ , where  $\lambda_g$  is the guided wavelength in the SIW at the center frequency.

### 6.1 Iris SIW bandpass filter for V-band applications

#### 6.1.1 Introduction

Substrate integrated waveguide (SIW) is relatively a new type of transmission line, which has the merits of both metallic rectangular waveguide and planar transmission line, like low insertion loss, low radiation loss and compact size. In other words, it provides bridge between bulky metallic waveguide and lossy planar technology. Hence, SIW technology has emerged as a very promising candidate for designing microwave and millimeter wave components like filters, couplers and antennas [88, 90, 92]. The SIW filters design based on iris cavity are equivalent to shunt-inductance-coupled waveguide filters design [93]. In recent years, iris SIW filters have been reported for narrowband applications

where the width of iris is calculated from equivalent K-inverter. But it has not been reported in the literature how one can find the width of the iris from the K-inverter parameters for a given order. In this work, a generalized procedure has been presented which can be utilized to design any narrowband iris SIW filters with FBW not more than 10%. Finally, for 60 GHz band, the design equation of iris width calculation is derived using curve fitting technique. Also, an iris SIW filter at 60 GHz has been designed following the same procedure.

### 6.1.2 Design techniques

Substrate integrated waveguide is made of two periodic arrays of metal cavity which connects the top and ground plane and works as side walls of conventional metallic waveguide. The longitudinal spacing between them is kept below a certain limit so that radiation leakages are minimized [113]. The characteristics of electromagnetic fields in SIW structure and its equivalent rectangular waveguide are similar. Hence, a relation has been developed between the width of SIW and the effective width of the equivalent rectangular waveguide in terms of diameter and pitch of metallic vias, which is expressed in chapter 3 as (3.8).

After defining the dimensions of SIW structure, now it is equivalent to a conventional waveguide, so we can use the iris structure of waveguide to design iris SIW band pass filter. The resonators of band pass filter are cascaded via K-inverters where each iris is equivalent to a K-inverter; the normalized impedances of the inverters can be calculated from [89] as

$$\frac{K_{0,1}}{Z_0} = \sqrt{\frac{\pi}{2} \frac{\omega_\lambda}{g_0 g_1}} \quad (6.1)$$

$$\frac{K_{j,j+1}}{Z_0} = \frac{\pi}{2} \frac{\omega_\lambda}{\sqrt{g_j g_{j+1}}} \quad (6.2)$$

$$\frac{K_{n,n+1}}{Z_0} = \sqrt{\frac{\pi}{2} \frac{\omega_\lambda}{g_n g_{n+1}}} \quad (6.3)$$

where  $Z_0$  is the waveguide impedance and  $\omega_\lambda$  is the guided-wavelength fractional bandwidth at the edges  $\lambda_{g1}$ ,  $\lambda_{g2}$  and mid-band  $\lambda_{g0}$ , which is defined as below

$$\omega_\lambda = \frac{\lambda_{g1} - \lambda_{g2}}{\lambda_{g0}} \quad (6.4)$$

The low pass prototype element values  $g$  for a given order is found from [33]. Thus, one can find the

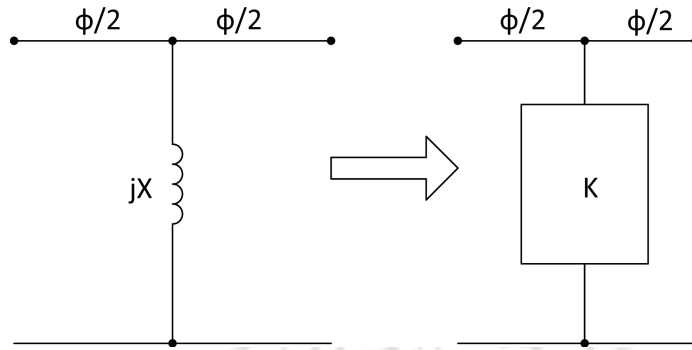


Figure 6.1: Model of inductive window and its equivalent circuit.

K-inverters theoretically.

Using the theoretically calculated values of K-inverters, we can find the shunt reactance  $X_{j,j+1}$  for purely lumped inductance discontinuities as follow [89]

$$\frac{X_{j,j+1}}{Z_0} = \frac{\frac{K_{j,j+1}}{Z_0}}{1 - \left(\frac{K_{j,j+1}}{Z_0}\right)^2} \quad (6.5)$$

### 6.1.3 Approximate design equation

Once the normalized impedances of the inverters are calculated, the physical dimensions of corresponding irises need to be found. Since each iris is equivalent to K-inverter with corresponding reactance X as shown in Figure 6.1. The K-inverters can be found from S parameters (from the simulation results) approximately as [93]

$$j\frac{X}{Z_0} = \frac{2S_{21}}{(1 - S_{11})^2 - S_{21}^2} \quad (6.6)$$

$$\phi = -\tan^{-1}\left(\frac{2X}{Z_0}\right) \quad (6.7)$$

$$\frac{K}{Z_0} = \left|\tan \frac{\phi}{2}\right| \quad (6.8)$$

Once the inverter parameters are known from (6.6)-(6.8), the distance between each iris windows ( $l_i$ ) for filter design can be found as

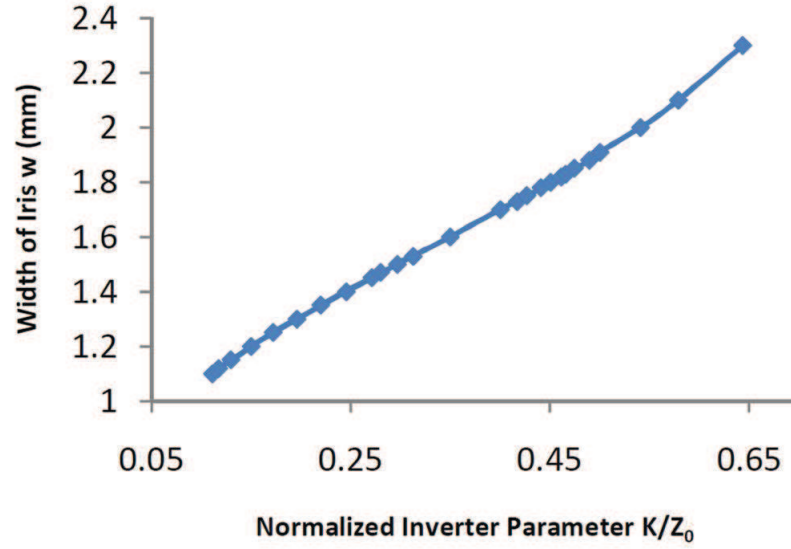


**Figure 6.2:** Plot of iris width variation corresponding to normalized inverter parameter  $K$ .

$$l_i = \frac{\theta_i \lambda_{g0}}{2\pi} \quad (6.9)$$

$$\theta_i = \pi + \frac{1}{2}(\phi_i + \phi_{i+1}) \quad (6.10)$$

*Steps followed for iris width calculation:*

*Step 1:* De-embedding: Using full wave simulator like HFSS, we can chose de-embedding technique to find out S parameters for different values of iris width instead of moment method [114]. The length of the SIW section is chosen about half to one wavelength or twice the width of the equivalent waveguide from each side of the iris. Then, the reference plane is moved to the centre of the iris for each port in order to de-embed the phase changes occurred in the waveguide. Finally, extract the S parameters at the mid-frequency.

*Step 2:* Substitute the S parameters in (6.6) and get the inverter parameters.

*Step 3:* Repeat the procedure for different values of the iris width.

*Step 4:* Applying curve-fitting technique, plot the graph between inverter parameters ( $K, \phi$ ) and iris width ( $w$ ).

*Step 5:* Obtain the approximate iris width corresponding to normalized inverter parameters.

The specifications for the design are:

## 6. Filters design using SIW, SSPP and linear taper

**Table 6.1:** Calculated and theoretical normalized inverter parameters for different iris width

Calculated $\frac{X}{Z_0}$	Calculated $\frac{K}{Z_0}$	Calculated $\phi$ (radians)	Iris width $w$ (mm)	Theoretical $\frac{X}{Z_0}$
0.1125	0.1111	0.2213	1.1	0.1125
0.12	0.11723	0.2356	1.12	0.1189
0.1324	0.13	0.259	1.15	0.1322
0.1541	0.15	0.3	1.2	0.1535
0.1774	0.172	0.341	1.25	0.1772
0.204	0.196	0.3874	1.3	0.2038
0.23128	0.22	0.43325	1.35	0.2312
0.261	0.2453	0.4811	1.4	0.2610
0.2923	0.271	0.529	1.45	0.2925
0.3043	0.2804	0.5467	1.47	0.3043
0.325	0.2965	0.574	1.5	0.3251
0.34625	0.3124	0.6057	1.53	0.3426
0.39868	0.35	0.673	1.6	0.3989
0.4777	0.4	0.7626	1.7	0.4762
0.5042	0.41667	0.78958	1.73	0.5042
0.521736	0.42673	0.80667	1.75	0.5217
0.548	0.4413	0.8312	1.78	0.5480
0.5658	0.451	0.847	1.8	0.5662
0.5858	0.4612	0.86425	1.82	0.5858
0.5944	0.4656	0.87144	1.83	0.5945
0.6131	0.4749	0.8867	1.85	0.6132
0.644	0.4896	0.9106	1.88	0.6440
0.6723	0.5	0.931	1.91	0.6667
0.765	0.541	0.992	2	0.7649
0.8712	0.579	1.05	2.1	0.8710
1.0986	0.6436	1.1437	2.3	1.0987

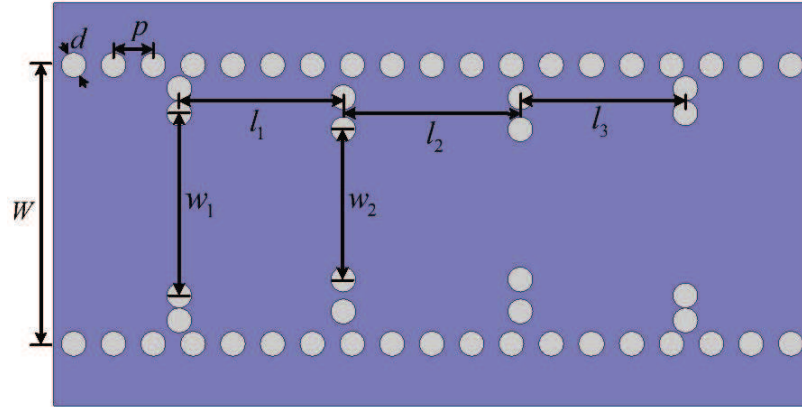
- Solution Frequency : 60 GHz
- Substrate: Taconic TacLamPLUS ( $\epsilon_r = 2.1, h = 0.2$  mm).

The diameter of each metal cavity is set to 0.25 mm and spacing between adjacent via holes is 0.4 mm. The width of SIW is 2.8 mm.

By using curve fitting technique (Figure 6.2), an approximate 3<sup>rd</sup> order polynomial equation has been derived for iris width calculation (in mm) corresponding to each normalized K-inverter

$$w = 0.7734 + 3.4266 \frac{K}{Z_0} - 4.6881 \left( \frac{K}{Z_0} \right)^2 + 4.7287 \left( \frac{K}{Z_0} \right)^3 \quad (6.11)$$

However, the accuracy of the above proposed design equation can be improved at the cost of higher order polynomial and non-linear approximations.



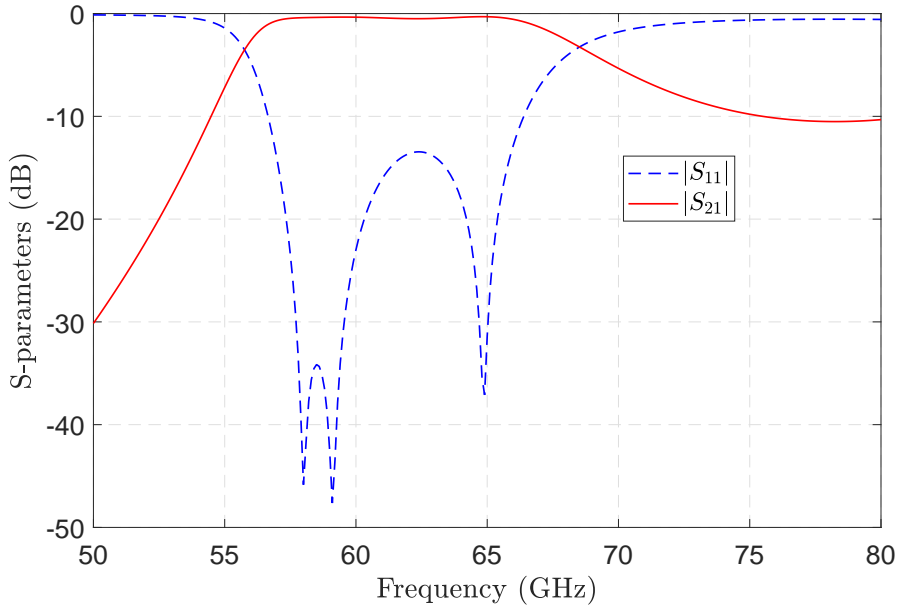
**Figure 6.3:** 3<sup>rd</sup> order iris SIW bandpass filter design.

Table 6.1 lists the calculated and theoretical normalized inverter parameters and also the approximate iris width corresponding to them. The theoretical normalized reactance values obtained from (6.5) are very close to calculated normalized reactance from simulation, (6.6), validating the above procedure and approximate design equation. However, the design procedure is valid only for narrow-band filter but can be applied for any desired frequency band. In case of wideband applications (FBW greater than 10%), the theoretically calculated width of each irises will not remain enough accurate and simulation requires more number of tuning to achieve desired dimensions.

#### 6.1.4 Iris SIW bandpass filter design

Following the above procedure, a 3<sup>rd</sup> order Chebyshev filter with 0.1 dB insertion loss and 15 dB return loss in 57-66 GHz passband [93] has been designed for V-band applications. The normalized inverter values are calculated first from (6.1)-(6.3) theoretically as  $K_{01} = K_{34} = 0.48$  and  $K_{12} = K_{23} = 0.28$ . Then dependencies of normalized inverter parameters ( $K, \phi$ ) with iris width ( $w$ ) from (6.11) are used. The iris width values corresponding to the calculated K-values are obtained as  $w_1 = 1.87$  mm and  $w_2 = 1.47$  mm. Using the phase change occurred ( $\phi_i$ ) from (6.7) into (6.10), the distance between each iris windows from (6.9) can be calculated as  $l_1 = l_3 = 1.68$  mm and  $l_2 = 1.81$  mm. These values are considered as a first approximation for filter design and then tuned to achieve optimum passband return loss.

The schematic design of the filter has been shown in Figure 6.3. Their final dimensions are  $l_1 = l_3 = 1.65$  mm,  $l_2 = 1.78$  mm,  $w_1 = 1.83$  mm and  $w_2 = 1.51$  mm. The design has been simulated using FEM based HFSS software. The frequency response of the designed iris SIW BPF is shown in Figure



**Figure 6.4:** Simulated frequency response of the designed iris SIW BPF.

6.4. The insertion loss of the filter is less than 0.5 dB and its return loss is better than 13.5 dB in whole designated passband. The performance of the filter is in good agreement with [93]. However, there is very poor rejection and roll-off rate at the higher frequencies which can be improved by employing the method as proposed in [93].

## 6.2 Hybrid SSPP-SIW bandpass filters for X-band applications

### 6.2.1 Introduction

Surface plasmon polaritons (SSPs) are highly localized surface electromagnetic waves that propagate along the dielectric-metal interface and decay exponentially in the directions perpendicular to the surface [115,116]. The most important characteristic of SSPs is the electromagnetic field confinement in the near vicinity of the interface in subwavelength scales, but they only exist in the optical regime. In 2004, Pendry *et al.* [117] proposed a new structure by perforating conductor surfaces to mimick the SSPs behaviour at lower frequencies like microwave or terahertz (THz) bands, called as designer surface plasmon polaritons or spoof surface plasmon polaritons (SSPPs). After that, many efforts have been performed to design plasmonic metamaterial structures [118–121], broadband transition from guided waves to SSPP [122–124], in the microwave or THz bands. A comb-shaped SSPP structure

loaded with two H-shaped cells in the center forms a non-periodic SSPP [125], and a highly selective wideband bandpass filter (BPF) is realized by using spiral-shaped defected ground structure on coplanar waveguide (CPW). Due to inimitable advantages such as high field confinement, slow-wave characteristic and flexible planar structure, SSPPs has inspired a lot of research works in the design of microwave, millimeter-wave and THz devices.

The traditional SIW filters often suffer with narrow passband and poor stopband attenuation [88, 92]. There are some efforts have been made in [126–129], to broaden the passband bandwidth of SIW filters. By using electromagnetic bandgap (EBG) periodic structure, super-wide bandpass SIW filters are designed [126], and fractional bandwidth (FBW) of up to 61.5% have been reported. In [127], a folded SIW is integrated with compact resonant cell, and a wide FBW of 77% has been achieved, but it has not been accounted the stopband performances. An ultra-wideband BPF using hybrid half-mode T-septum SIW and EBG has been presented in [128], but it suffers with an insertion loss of more than 2.2 dB in the desired passband. A compact wideband BPF using U-slotted SIW cavities with 3-dB FBW of 42% has been presented in [129], where out-of-band rejection of only 15 dB up to 20 GHz being reported.

The concept of designing broadband bandpass filters using low-pass characteristics of SSPP and high-pass characteristics of SIW is termed as hybrid SSPP-SIW filters [1, 95–100]. The first hybrid SSPP-SIW filter was proposed in [95], where the SSPPs structure were connected in series with SIW section. Since, the two structures are separated, resulting in a larger size, as well the conversion of the fields add more complication. In [96], a hybrid SSPP-SIW transmission line for designing broadband BPFs have been proposed, where SSPPs propagate through arrays of transverse metallic blind holes that were designed inside the SIW. Although, it requires a thicker substrate to achieve larger slow-wave characteristics, and hence not a right choice for compact circuit applications. A planar bandpass filter based on a hybrid SSPP-SIW transmission line is presented in [97], but only simulation results have been shown. Hybrid half-mode substrate integrated waveguide (HMSIW) SSPP structures have been proposed in [98, 99], which overcome shortcomings of large size. However, their transmission characteristics further need to be improved. Also, none of the above hybrid SSPP-SIW filters considers out-of-band rejection. A broadband BPF using hybrid SSPP-SIW structure has been proposed in [1], which showed wide out-of-band rejection but suffers from poor in-band performances. Recently, a bandpass filter based on half-mode SIW and double-layer SSPPs has been developed [100], which

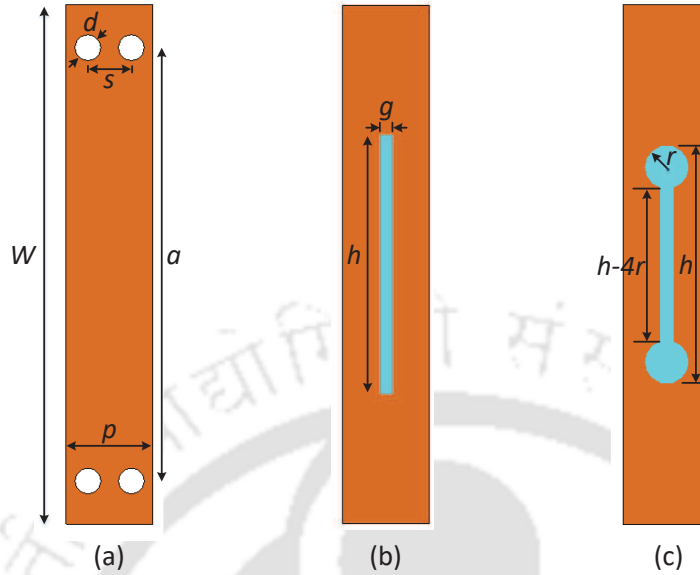


**Figure 6.5:** Configuration of unit cells (a) SIW unit (b) Rectangle-shaped SSPP unit and (c) Dumbbell-shaped SSPP unit.

features wider bandwidth, smaller size and lower loss than previously reported structures.

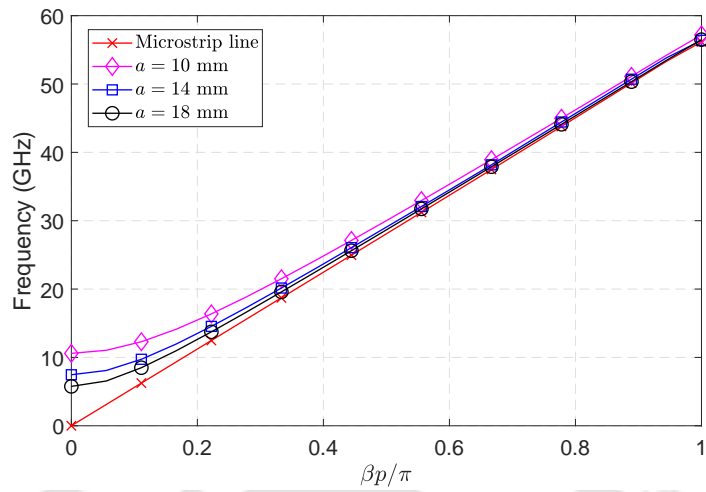
In this work, we propose two hybrid SSPP-SIW filters, one using rectangle-shaped and the other using dumbbell-shaped SSPPs, for X-band applications. Firstly, the dispersion and propagation characteristics of SSPPs and SIW units are investigated. It is found that the dumbbell-shaped SSPP shows much and better slow-wave characteristics than rectangle-shaped SSPP for the equal height of grooves. By tuning the structural parameters of SIW and SSPPs, the lower and upper cutoff frequencies of bandpass filters can be obtained independently. The proposed filters show excellent broadband passband and wide out-of-band rejection simultaneously.

### 6.2.2 Dispersion characteristics of SIW and SSPPs

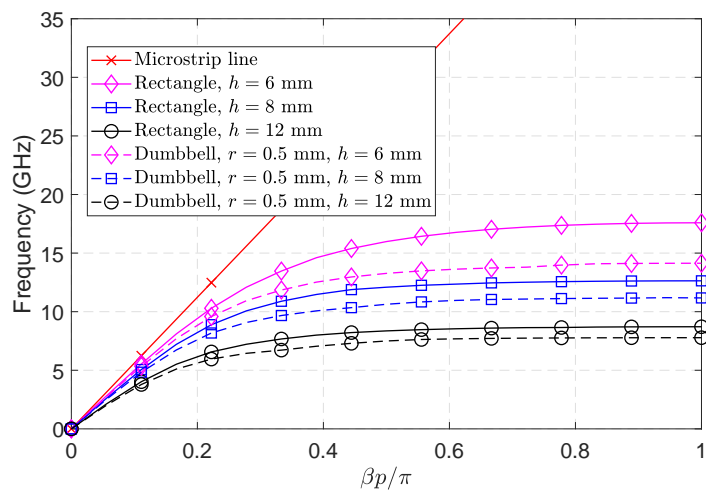
Figure 6.5 shows the configurations of SIW, rectangle-shaped SSPP and dumbbell-shaped SSPP units. The dispersion relation for fundamental  $TE_{10}$  mode of SIW is derived as [130]

$$\beta = \sqrt{\mu_r \epsilon_r \left(\frac{\omega}{c}\right)^2 - \left(\frac{\pi}{a}\right)^2} \quad (6.12)$$

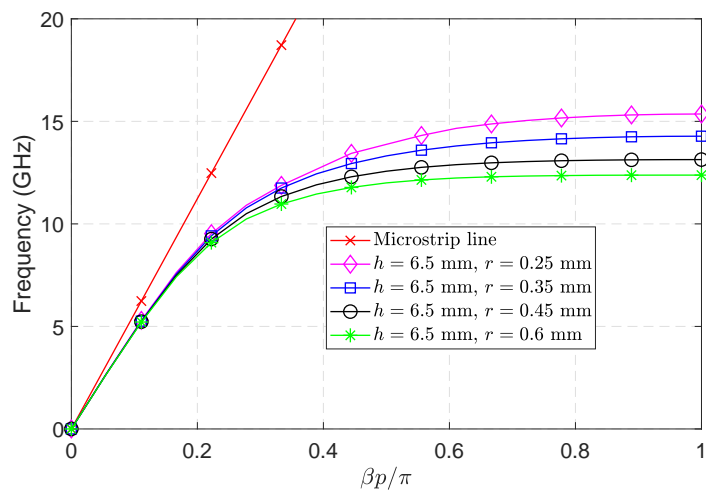
where  $\beta$  is the propagation constant of fundamental  $TE_{10}$  mode of SIW and  $a$  is the width of SIW. The grooves are corrugated in a metal conductor to construct a SSPP structure, where  $g$  and  $h$  are the width and height of grooves, respectively, and  $p$  is the period of SSPP unit. It has been shown that



(a)



(b)



(c)

**Figure 6.6:** Dispersion diagrams (a) SIW unit (b) Rectangle-shaped & dumbbell-shaped SSPP units and (c) Different radii of dumbbell-shaped SSPP unit.

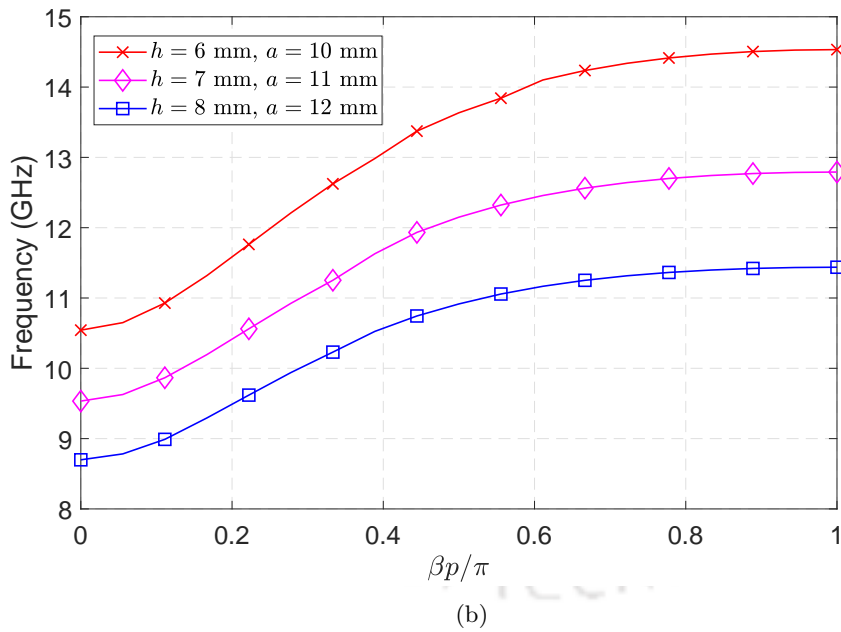
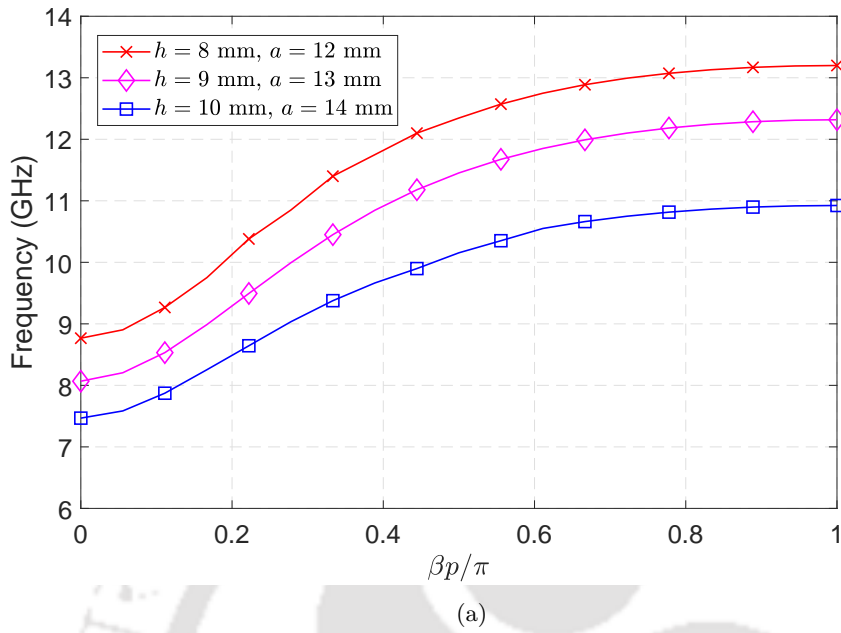


**Figure 6.7:** Dispersion diagrams of hybrid SSPP-SIW units (a) Rectangle-shaped and (b) Dumbbell-shaped with fixed  $r = 0.41$  mm.

such periodic metallic grooves can support and propagate a SSPP mode at microwave frequencies, when  $g$  and  $p$  are much less than the wavelength of light at the design frequency. The dispersion

relation of SSPP is given by [118]

$$\beta = \frac{\omega}{c} \sqrt{1 + \frac{g^2}{p^2} \tan^2 \left( \frac{\omega}{c} h \right)} \quad (6.13)$$

where  $\beta$  is the propagation constant of SSPPs mode. The initial width of SIW and SSPP design parameters (width, height and period) can be analytically determined using these equations and then can be fine-tuned with the help of full-wave EM field solvers.

The structures are designed using Rogers RT/Duroid 5880 substrate with a dielectric constant of 2.2, dielectric loss tangent of 0.0009, dielectric thickness of 0.508 mm and metal (copper) thickness of 0.018 mm. The parameters are set as:  $d = 0.6$  mm,  $s = 0.9$  mm,  $p = 1.8$  mm, and  $g = 0.2$  mm. Eigen-mode solver of CST microwave studio is used for analyzing dispersion characteristics of the unit cells. The dispersion curves of pure SIW, pure rectangle- and dumbbell-shaped SSPPs are plotted in Figures 6.6(a) and 6.6(b), respectively. It can be observed that SIW unit has a low cutoff frequency which decreases with the increase in width of SIW ( $a$ ), and falls under the fast-wave region as expected. The SSPPs have a high cutoff frequency which decreases as the height of groove ( $h$ ) increases and shows slow-wave characteristics with the increase in frequency. It is found that the dispersion curves of SSPPs with the same height of  $h$  on the dumbbell grooves are much lower than that of with rectangle grooves. When working at the same frequencies, wave vectors of SSPPs on the proposed dumbbell-shaped structure are larger than the rectangle-shaped structure, which means that stronger confinement of SSPP can be achieved based on a dumbbell-shaped structure in such a case. Hence, a more compact structure with higher slow-wave characteristics can be achieved using dumbbell-shaped SSPPs. The dispersion curves of dumbbell-shaped SSPPs with different radii are plotted in Figure 6.6(c), where it can be observed that bigger the radii, lower the dispersion curves, for the same height of  $h$ . So, it is also possible to independently determine the upper cutoff frequency of the structure by just manipulating the radius and keeping the height of groove fixed.

The proposed hybrid SSPP-SIW structures exhibit the dispersion features of both SIW and SSPP, supporting a hybrid fast-wave and slow-wave modes. Their dispersion curves, as shown in Figure 6.7, start at the low cutoff frequencies at the fast-wave region and then enter into the slow-wave region and cut off at asymptotic (high cutoff) frequencies. Their behaviour is like a SIW at low frequencies and like an SSPP at high frequencies. Therefore, the slow-wave effect can be achieved by applying such sub-wavelength corrugation to the SIW.

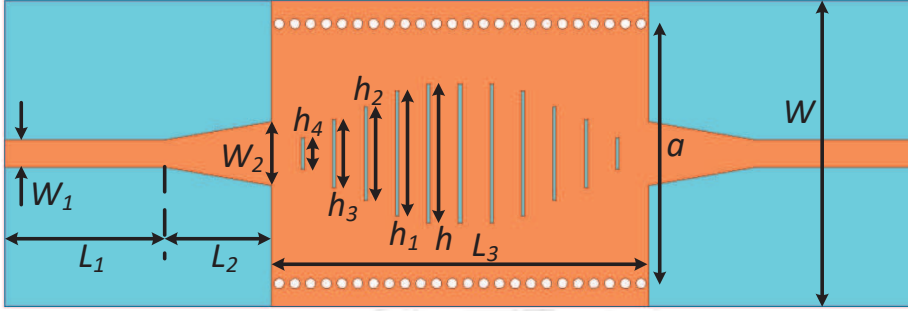


**Figure 6.8:** Configuration of the hybrid SSPP-SIW structure with graded rectangular slots heights of  $h_i$  ( $i = 1, 2, 3, 4$ ) ( $a = 14.85$  mm,  $h = 6.5$  mm,  $W = 17.5$  mm,  $L_1 = 9.25$  mm,  $W_1 = 1.565$  mm,  $L_2 = 6$  mm,  $W_2 = 3.625$  mm and  $L_3 = 21.6$  mm).

### 6.2.3 Demonstration of hybrid SSPP-SIW bandpass filters

Initially, the hybrid SSPP-SIW structure, as shown in Figure 6.8, is investigated by varying the graded rectangular slots heights of  $h_i$  ( $i = 1, 2, 3, 4$ ). The simulated S-parameters are plotted in Figure 6.9, where it can be observed that the performances are optimum for the linearly graded slots with same slope of the microstrip taper. This is due to the optimum conversion of  $TE_{10}$  mode of SIW to the mode of SSPP.

The configurations of proposed hybrid SSPP-SIW filters are depicted in Figure 6.10. The proposed structures consist of three regions: microstrip to SIW transition (Region I), SIW to SSPP transition (Region II) and hybrid SSPP-SIW part (Region III). The linearly tapered microstrip line [85, 91] is employed for broadband impedance matching of  $50 \Omega$  input/output feedline to SIW; as can be seen in Region I. It enables a smooth transition of quasi-TEM mode of microstrip to fundamental  $TE_{10}$  mode of SIW. To match the momentum of conventional SIW to the hybrid SSPP-SIW, we propose a transition using linearly graded rectangular slots to produce gradient momentum, as shown in Region II. It can also be noted that the rectangular slots are made to be tapered at the ends and matched with the same slope of microstrip taper. This has been done so that broadband impedance matching with least reflections, to smoothly convert fundamental  $TE_{10}$  mode of SIW to the mode of SSPP, can be achieved.

The transmission characteristics of proposed hybrid SSPP-SIW structures have been investigated by varying the parameters such as width of SIW  $a$ , height of groove  $h$  and radius of dumbbell  $r$ , as shown in Figure 6.11. The width and length of  $50 \Omega$  microstrip lines are  $W_1 = 1.565$  mm and  $L_1 = 9.25$  mm. The initial width and length of linearly tapered microstrip lines are calculated from

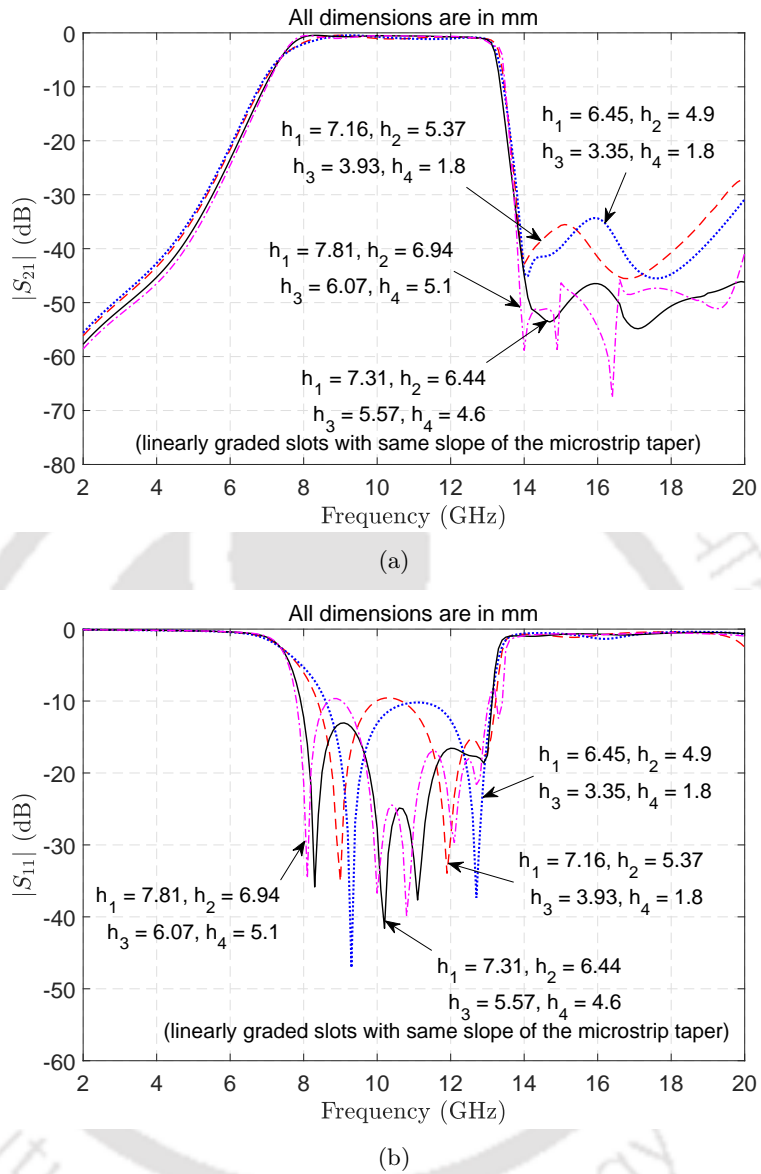


**Figure 6.9:** Simulated S-parameters of the hybrid SSPP-SIW structure with varied graded rectangular slots heights,  $h_i$  ( $i = 1, 2, 3, 4$ ).

[27]. They are optimized using EM simulations, and the parameters are set as  $W_2 = 3.625$  mm and  $L_2 = 6$  mm. The length of SIW section  $L_3$  is 21.6 mm. The variation in width of SIW of a rectangle-shaped SSPP-SIW structure with the groove height of 8 mm are depicted in Figure 6.11(a), where it is evident that the lower cutoff frequency of the passband can be controlled independently with a very less or no influence on the upper cutoff frequency. Figure 6.11(b) illustrates that the upper cutoff frequency can be adjusted independently by varying the height of rectangle-shaped groove and keeping the width of SIW fixed as 14.85 mm, but has a little influence on the lower cutoff frequency

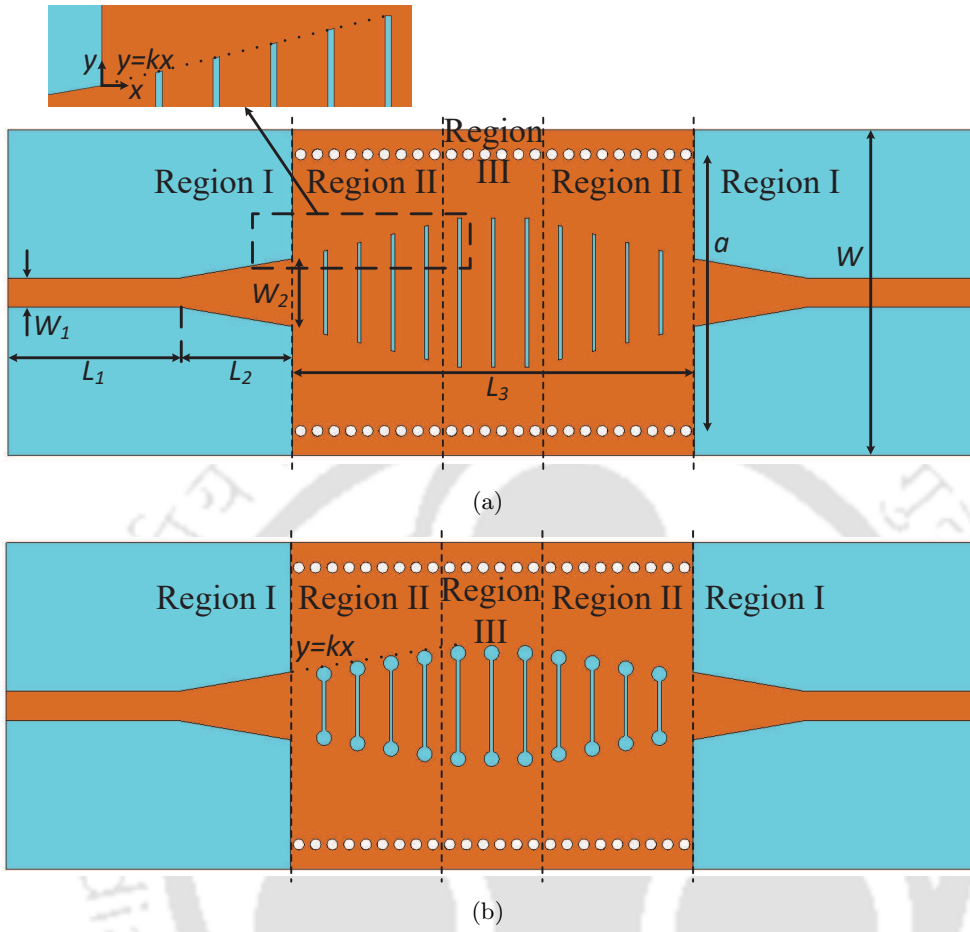
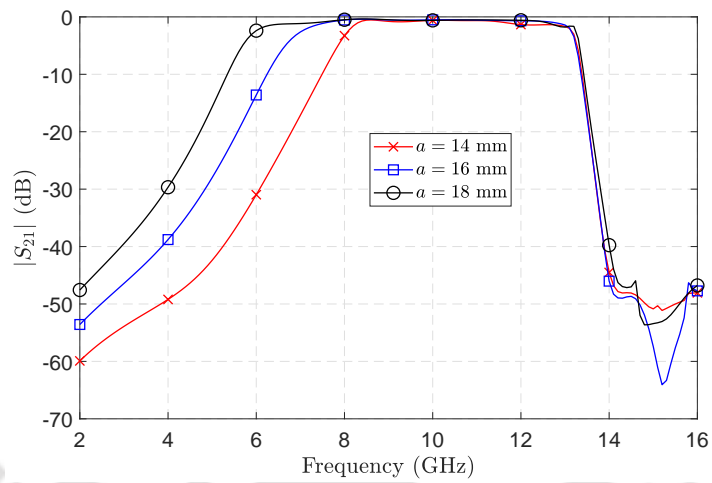


**Figure 6.10:** Configurations of the proposed hybrid SSPP-SIW filters (a) Rectangle-shaped and (b) Dumbbell-shaped.

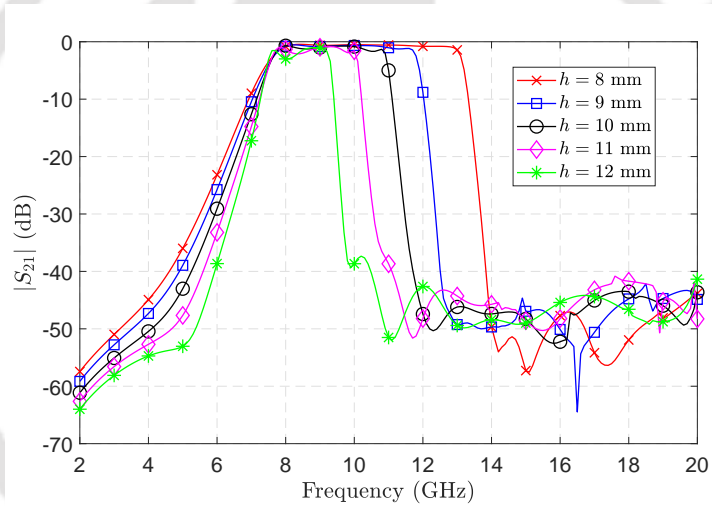
**Table 6.2:** Design parameters of rectangle-shaped hybrid SSPP-SIW filter (Units: mm)

$a$	$d$	$s$	$p$	$g$	$h$
14.85	0.6	0.9	1.8	0.2	8
$W$	$L_1$	$W_1$	$L_2$	$W_2$	$L_3$
17.5	9.25	1.565	6	3.625	21.6

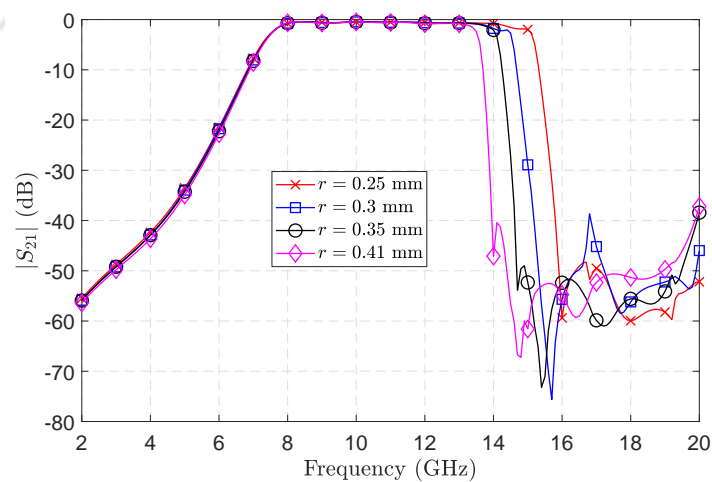
mainly due to the attenuated coupling between SIW and SSPP units. The similar characteristics for varying width of SIW and groove height of a dumbbell-shaped SSPP-SIW case can be obtained. Transmission coefficients for different radii of dumbbell-shaped hybrid SSPP-SIW structure with a fixed groove height of 6.5 mm are plotted in Figure 6.11(c). By increasing the radius of dumbbell, the upper cutoff frequency independently can be shifted towards the right with no influence on the lower cutoff frequency. The lower and upper cutoff frequencies in transmission coefficients of Figure 6.11 agree well with the dispersion curves of unit cells in Figure 6.6, which validates them.



(a)



(b)



(c)

**Figure 6.11:** Simulated transmission coefficients of the proposed hybrid SSPP-SIW structures (a) Different widths of SIW with rectangle-shaped SSPP (b) Different heights of rectangle-shaped SSPP and (c) Different radii of dumbbell-shaped SSPP with fixed  $h = 6.5$  mm.

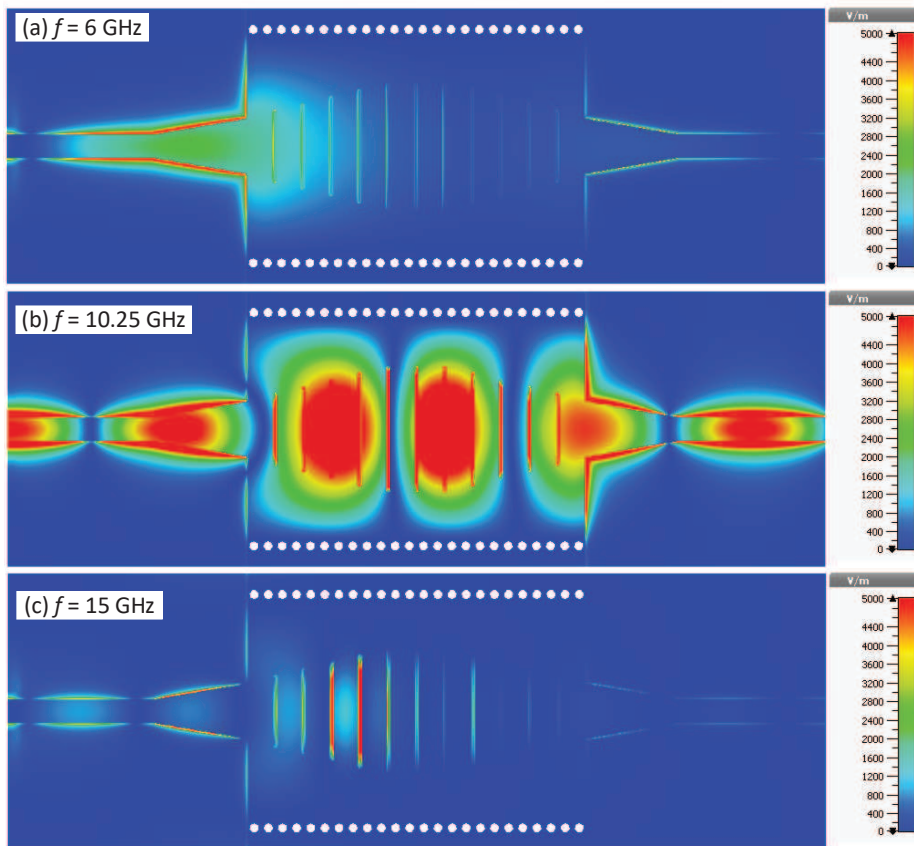


**Figure 6.12:** Electric field distributions of the rectangle-shaped SSPP-SIW bandpass filter (a) At the lower frequency stopband (b) At the passband and (c) At the upper frequency stopband.

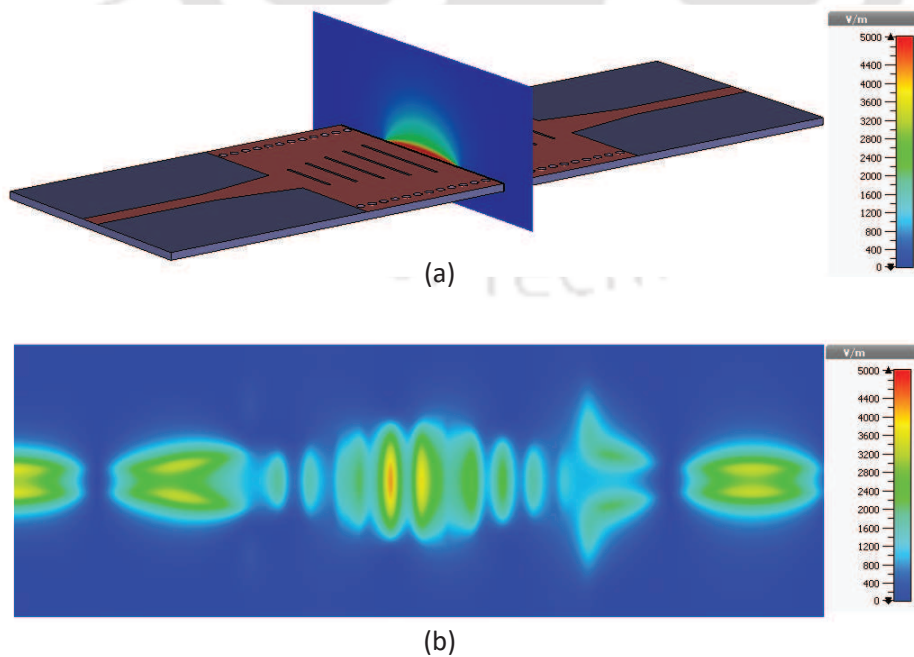


**Figure 6.13:** Electric field distributions of the rectangle-shaped SSPP-SIW bandpass filter (a) Across the cross-sections at 10.25 GHz and (b) 0.5 mm above the top surface at 10.25 GHz.

To demonstrate the proposed hybrid SSPP-SIW structures, two filters are designed and analyzed for X-band applications. Their schematic configurations are shown in Figure 6.10. The material parameters for the filters are the same as presented above. The design parameters of the rectangle-shaped hybrid SSPP-SIW filter are given in Table 6.2. For dumbbell-shaped hybrid SSPP-SIW filter, the design parameters are the same as for rectangle-shaped case, only the height of groove  $h$  is changed to 6.5 mm and the radius of dumbbell  $r$  is chosen as 0.41 mm. Their simulated electric-field distributions at different frequencies are shown in Figures 6.12-6.15. As can be seen in Figures 6.12(a), 6.12(c), 6.14(a) and 6.14(c), the electromagnetic (EM) waves cannot propagate through the structures when frequency lies in the stopband regions. In the passband, the EM waves are propagating intensively and exhibit efficient mode conversion, as shown in Figures 6.12(b) and 6.14(b). It can also be noted that the electric fields are highly confined in the corrugated surface of hybrid SSPP-SIW structures. Their electric field distributions across the cross-sections and 0.5 mm above the top surface at the passband frequency of 10.25 GHz are shown in Figures 6.13(a), 6.15(a) and Figures 6.13(b), 6.15(b) respectively. It can be observed that fields are highly localized, propagate along the dielectric-metal interface and decay exponentially in the transverse directions, similar to the natural SPPs.

The proposed hybrid SSPP-SIW filters are fabricated and tested for experimental verification. Photographs of the fabricated prototype rectangle- and dumbbell-shaped SIW-SSPP filters are shown in Figures 6.16 and 6.17 respectively. The simulated and measured S-parameters of the rectangle-shaped hybrid SSPP-SIW bandpass filter are plotted in Figure 6.18. The bandwidth (BW) ranges from 8 to 13.15 GHz for  $|S_{11}| < -10$  dB and  $|S_{21}| > -1$  dB, covering the whole X-band of 8-12 GHz. A very good return loss (RL) of more than 13 dB in the whole passband has been achieved. The upper out-of-band rejection is better than 42.5 dB from 14.1 to 20 GHz. Figure 6.19 shows the simulated and measured S-parameters of the dumbbell-shaped SSPP-SIW filter. Its 10-dB passband ranges from 8-13.5 GHz with a return loss of better than 12 dB and insertion loss (IL) less than 1 dB in the whole passband. The stopband attenuation is more than 41 dB from 14.2 to 19.5 GHz. The roll-off rate of the filters is also very high. It is important to note that at the transition edges of proposed bandpass filters (stopband to passband and passband to stopband transition phases), the transmission and reflection coefficients have been very smooth transitions as compared to previously reported SSPP based filters. The proposed filters possess very compact size and can be an excellent candidate for X-band applications.

## 6. Filters design using SIW, SSPP and linear taper

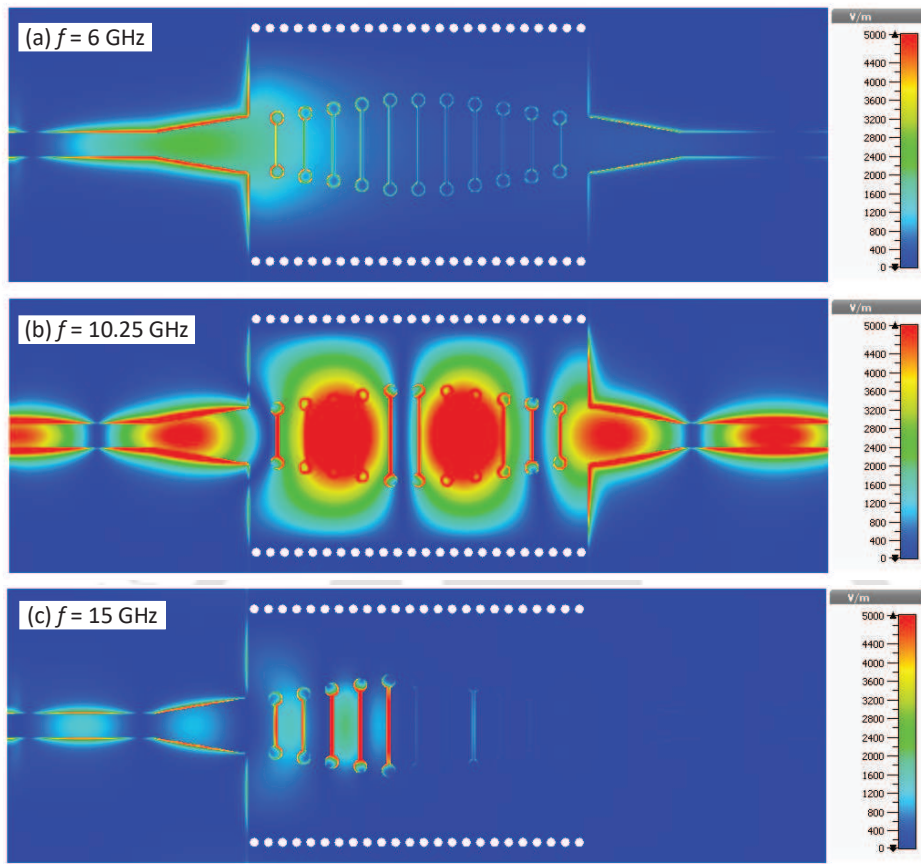


**Figure 6.14:** Electric field distributions of the dumbbell-shaped SSPP-SIW bandpass filter (a) At the lower frequency stopband (b) At the passband and (c) At the upper frequency stopband.

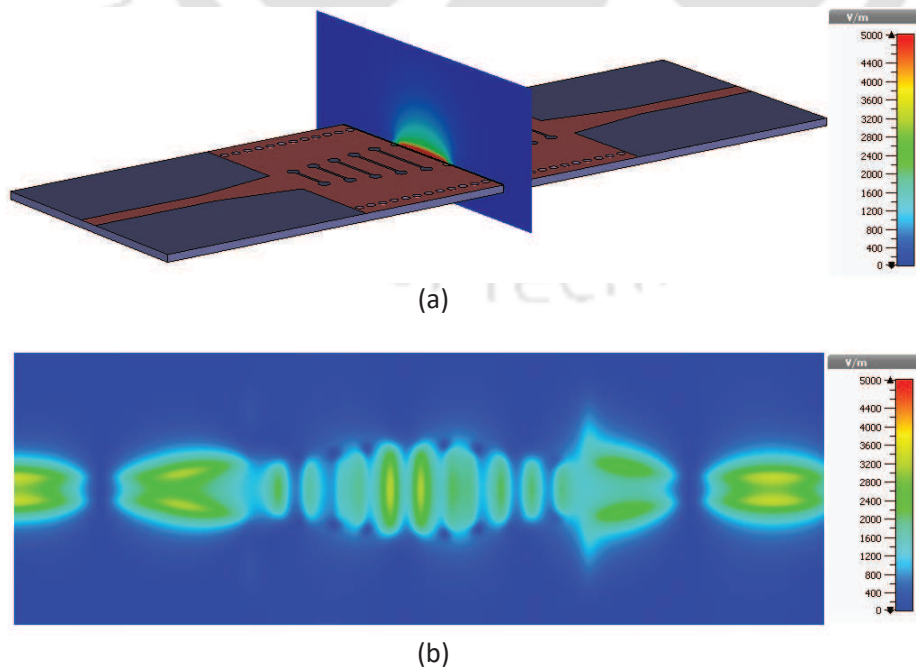


**Figure 6.15:** Electric field distributions of the dumbbell-shaped SSPP-SIW bandpass filter (a) Across the cross-sections at 10.25 GHz and (b) 0.5 mm above the top surface at 10.25 GHz.

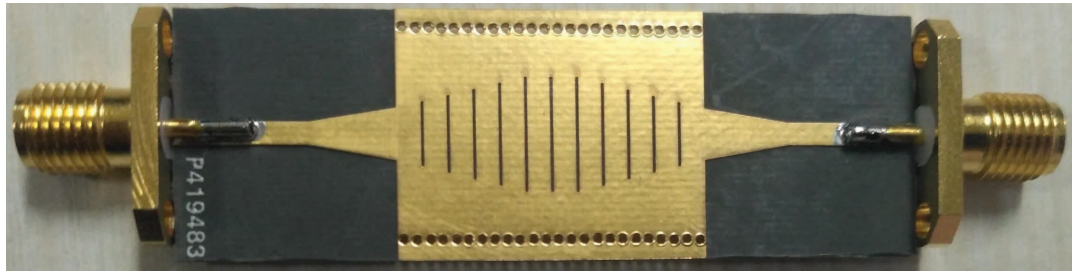


Figure 6.16: Photograph of the fabricated prototype rectangle-shaped SSPP-SIW BPF.

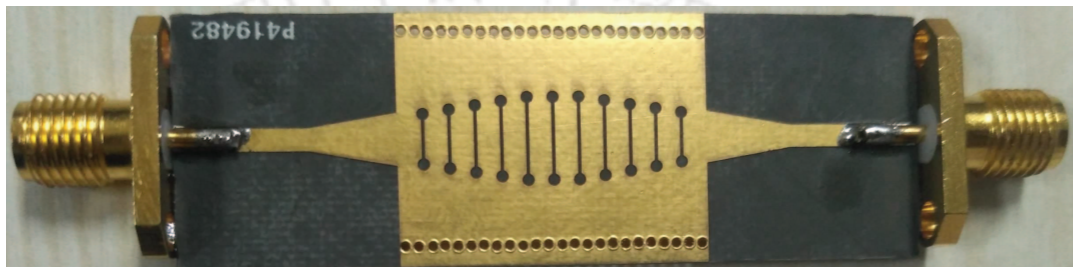


Figure 6.17: Photograph of the fabricated prototype dumbbell-shaped SSPP-SIW BPF.

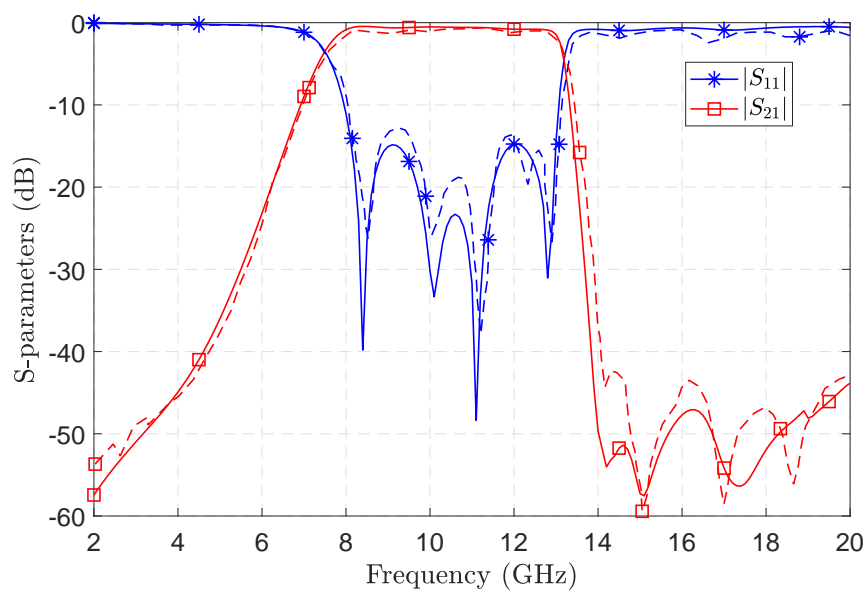
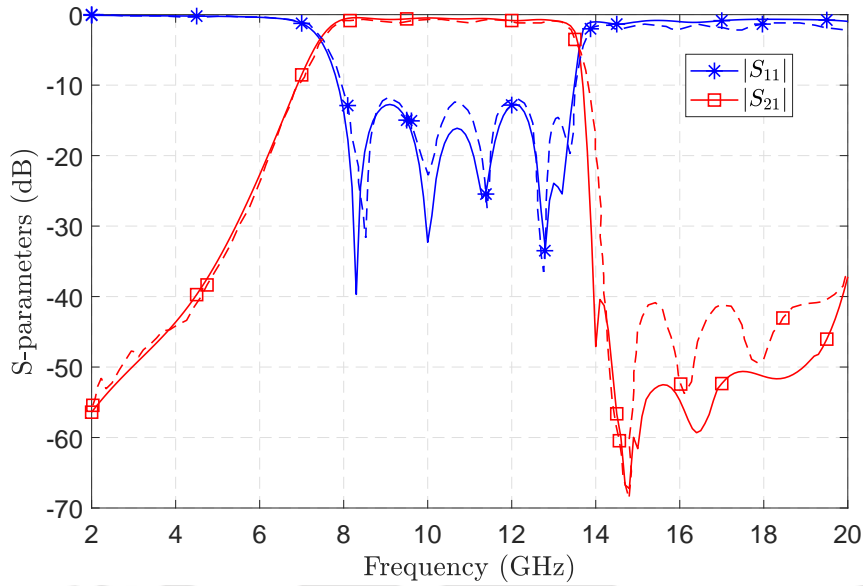


Figure 6.18: S-parameters of the rectangle-shaped SSPP-SIW bandpass filter (Solid lines represent simulated results and dashed lines represent measured results).

Table 6.3 compares the performance of the proposed hybrid SSPP-SIW filters with the existing SIW or hybrid SSPP-SIW filters. The proposed filters show excellent performance in the passband and out-of-band simultaneously. They also outperform almost in all parameters of the existing hybrid SSPP-SIW filters. As we have utilized least possible SSPP units (only three) and linearly graded

## 6. Filters design using SIW, SSPP and linear taper



**Figure 6.19:** S-parameters of the dumbbell-shaped SSPP-SIW bandpass filter (Solid lines represent simulated results and dashed lines represent measured results).

**Table 6.3:** Performance comparison with the existing planar SIW filters

References	10-dB BW (GHz)	FBW (%)	RL (dB)	IL (dB)	Size (Length $\times$ Width) ( $\lambda_g \times \lambda_g$ )	Upper-band Rejection	Type
[129]	6.75-10.25	41.1	>11	<1.1	1.2 $\times$ 0.6	20 dB @11.1-16.5GHz	U-slotted SIW
[95]	11.92-21.54	57.5	>10	<1	10.3 $\times$ 0.74	40 dB @22.5-30GHz	Hybrid SSPP-SIW
[97]	11.8-18.3	43.2	>10	<1	7.88 $\times$ 0.67	40 dB @20.3-22GHz	Hybrid SSPP-SIW
[98]	8-16	67	>12	<1.5	2.64 $\times$ 0.29	7 dB @16.2-17GHz	Hybrid HMSIW-SSPP
[1]	7.3-11.2	42.2	>12	<2	2.85 $\times$ 0.67	40 dB @11.8-19.8GHz	Hybrid SSPP-SIW
[100]	15.6-32.1	69.2	>10	<0.8	4.23 $\times$ 0.25	20 dB @35-40GHz	Hybrid HMSIW-SSPP
This work	8-13.15	48.7	>13	<1	0.99 $\times$ 0.69	42.5 dB @14.1-20GHz	Hybrid SSPP-SIW
	8-13.5	51.2	>12	<1	1.03 $\times$ 0.71	41 dB @14.2-19.5GHz	

rectangular slots for the optimum conversion of SIW to SSPP mode, the resultant structures are very compact. Their size are only about  $1\lambda_g \times 0.7\lambda_g$ , where  $\lambda_g$  is the guided wavelength in the SIW at the

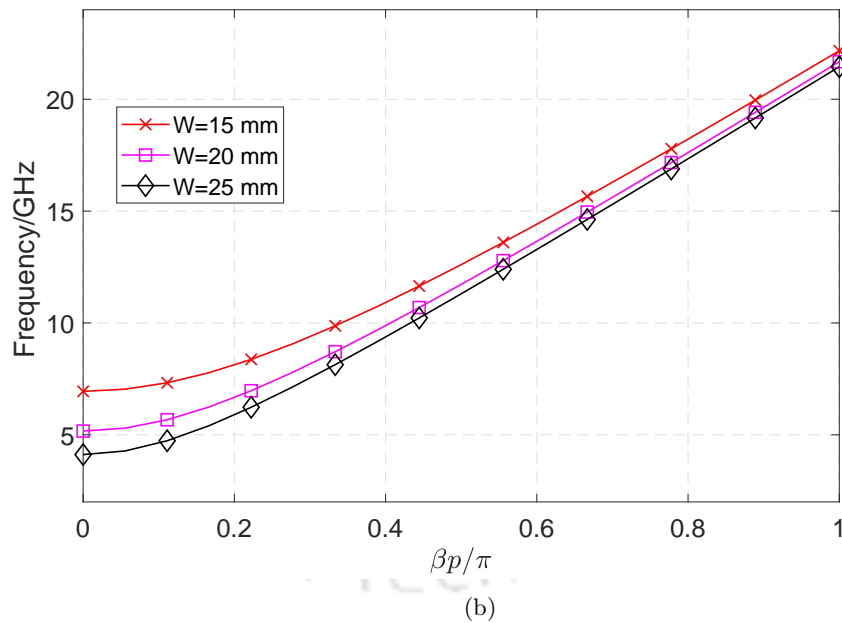
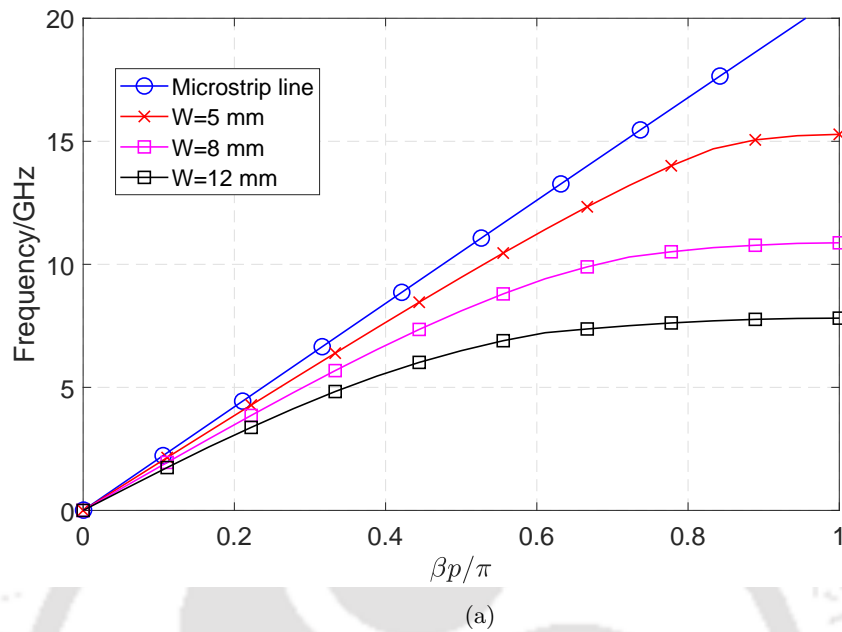


**Figure 6.20:** Dispersion diagrams (a) SSPP unit and (b) SIW unit.

center frequency.

### 6.3 Comment on “[1]”

The dispersion diagrams for proposed spoof surface plasmon polariton (SSPP) unit (Figure 1(b) of [1]) and substrate integrated waveguide (SIW) unit (Figure 1(c) of [1]) are plotted in Figure 2 of [1],

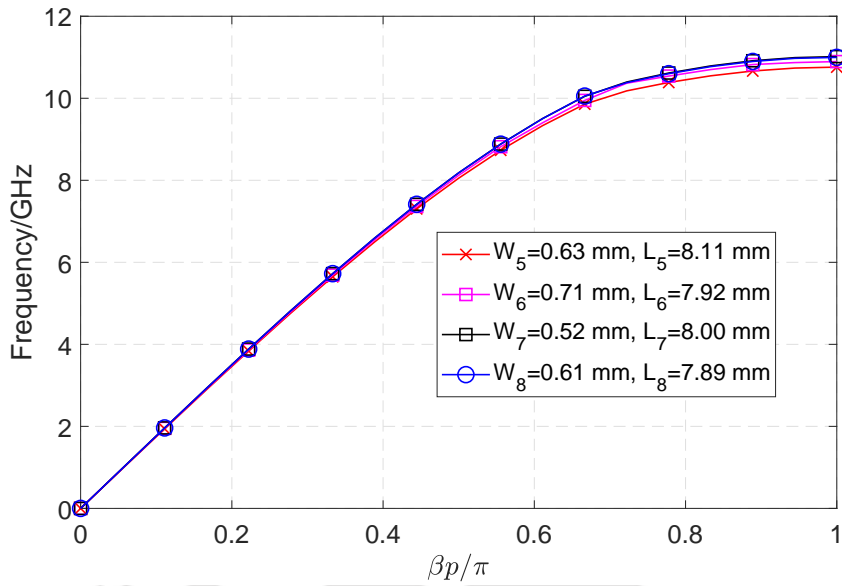


Figure 6.21: Dispersion curves for varied SSPP unit parameters.

which are incorrect and the correct dispersion curves for the same are presented here, as shown in Figure 6.20. The dispersion curves are analyzed and plotted for mode-1 simulation in eigen-mode solver of CST microwave studio. Furthermore, the dispersion curve with optimized dimensions,  $L_i$  and  $W_i$  where  $i \in (5, \dots, 8)$  for SSPP part (Figure 1(a) of [1]), are shown in Figure 6.21. The lower and upper cut-off frequencies for passband of the filter are defined from the structural parameters of SIW and SSPP units, respectively. It can be seen from the dispersion curves of SIW and SSPP units (Figure 2 of [1]) that the lower cut-off frequency obtained from SIW unit is around 7 GHz, while the upper cut-off frequency obtained from SSPP unit is around 6 GHz ( $W = 15$  mm of SIW unit and  $W = 8$  mm of SSPP unit). However, only the cutoff frequency in the dispersion curve of SIW unit is correct, from where the lower cut-off frequency of the proposed BPF is set around 7 GHz. The dispersion curve of SIW unit (Figure 1(c) of [1]) with correct distribution trend is shown here in Figure 6.20(b). The passband of proposed hybrid SSPP-SIW filter is about 7-11 GHz and hence the correct upper cut-off frequency for passband of the filter, as it can be seen from our corrected dispersion curve of SSPP unit, Figure 6.20(a), is about 11 GHz. It can also be noted that  $p$  is the period of SSPP in our corrected dispersion curves.

## 6.4 Summary

A design procedure has been presented for calculating iris width of an inductive window of narrow-band iris SIW filter followed by de-embedding technique; the fractional bandwidth is about 10%. At 60 GHz, a design equation has been developed for calculating different width of iris windows by using curve fitting technique and an iris SIW BPF has also been designed following the proposed method. The theoretical and calculated normalized reactance parameters are well matched which validate the same.

Two hybrid SSPP-SIW bandpass filters based on rectangle- and dumbbell-shaped SSPPs have been presented for X-band applications. The dispersion and propagation characteristics of SSPPs and SIW are analyzed. It has been found that the proposed dumbbell-shaped SSPP shows more slow-wave effects than rectangle-shaped SSPP for the same height of grooves, which could be very efficient in the design of compact, low loss and highly integrated microwave and terahertz devices. The lower and upper cutoff frequencies of hybrid SSPP-SIW bandpass filters can be adjusted independently by just varying the structural parameters of SIW and SSPP units, respectively. Linearly graded slots are being utilized for optimum conversion of SIW to SSPP mode in the proposed hybrid SSPP-SIW structures. The proposed filters show very good passband and wide upper out-of-band rejection simultaneously. They possess very compact size of  $\sim 1\lambda_g \times 0.7\lambda_g$ . Their length is only about a wavelength at the center frequency, which is much lesser than the length of existing hybrid SSPP-SIW filters.



# 7

## Conclusions and future work

### Contents

---

7.1	Conclusions . . . . .	112
7.2	Suggestions for future work . . . . .	113

---

The objective of the work presented in this thesis is to design, analyse and fabricate various microwave passive devices such as filters, power dividers, antennas, etc. for different microwave frequency band applications. Commercial full wave simulators (HFSS and CST microwave studio) and MATLAB are used for the design and analysis purpose. In this chapter, we conclude the thesis, discuss its findings and contributions, and also provide some suggestions for future extension of the presented works.

### 7.1 Conclusions

Briefly, the conclusions of the thesis are summarised as follows:

- An exponentially tapered impedance line stub loaded microstrip resonator (ETILSLMR) is proposed to design notched-UWB filter. An ultra-wideband (UWB) filter with a fractional bandwidth (FBW) of 121% at a center frequency of 6.6 GHz is designed first and then to suppress interference from IEEE 802.11a WLAN band, a sharp notch band is created around 5.5 GHz by tapered inductive loading on quarter-wavelength high impedance lines. An approximate theoretical analysis of the filters is also presented.
- Linear tapers have been theoretically characterized, and their results are compared with the other tapers. By using linearly tapered microstrip line, a broadband taper transition between microstrip line and SIW component and a novel coupled-line ultra-broadband bandpass filter are designed. The proposed filter possesses a very compact size of  $0.20\lambda_g \times 0.26\lambda_g$  and shows wide 10 dB passband from 4.5 to 12 GHz.
- An unequal T-junction power divider has been designed where the line to port 3 has also been tapered linearly for achieving higher power dividing ratio of more than 10 dB over a broad frequency range of 1.7-5 GHz. An approximate theoretical analysis of the power divider has also been presented. It has been observed that a SWB unequal T-junction power divider can be designed by using the same method. For example, in this work a SWB power divider is designed which shows a power dividing ratio of more than 10 dB in whole SWB bandwidth of 0.5-6 GHz.
- A dual-port, orthogonal polarized patch antenna with high isolation and low cross polarization has been proposed. The antenna can achieve a maximum isolation of 67.5 dB at 2.3 GHz and more than 59.5 dB in the band of 2.3-2.6 GHz. Such a simple and compact antenna can be

efficiently used for in-band full-duplex 2.4 GHz ISM operations. The same antenna geometry with the two feed lines (tapered feed and aperture coupled feed) can be tuned and used for designing antennas for in-band full-duplex radios such as for WiMAX applications.

- A design procedure has been presented for calculating iris width of an inductive window of narrowband iris SIW filter followed by de-embedding technique; the fractional bandwidth is about 10%. At 60 GHz, a design equation has been developed for calculating different width of iris windows by using curve fitting technique. An iris SIW BPF has also been designed validating the design equation for V-band applications.
- Two hybrid SSPP-SIW bandpass filters based on rectangle- and dumbbell-shaped SSPPs have been presented for X-band applications. The dispersion and propagation characteristics of SSPPs and SIW are analyzed. It has been found that the proposed dumbbell-shaped SSPP shows more slow-wave effects than rectangle-shaped SSPP for the same height of grooves. They could be very efficient in the design of compact, low loss and highly integrated microwave and terahertz devices. The lower and upper cutoff frequencies of hybrid SSPP-SIW bandpass filters can be adjusted independently by just varying the structural parameters of SIW and SSPP units, respectively. Linearly graded rectangular slots are being utilized for optimum conversion of SIW to SSPP mode in the proposed hybrid SSPP-SIW structures. The proposed filters exhibit excellent passband (8-13.15 GHz & 8-13.5 GHz) and wide upper-band rejection (>42.5 dB from 14.1-20 GHz & >41 dB from 14.2-19.5 GHz) simultaneously. They possess very compact size of  $\sim 1\lambda_g \times 0.7\lambda_g$ . Their length is only about a wavelength at the center frequency, which is much lesser than the length of existing hybrid SSPP-SIW filters.

## 7.2 Suggestions for future work

Some of the possible directions that can be taken up as extensions of this works are as follows:

- (1) **Equivalent circuit analysis for the notched-UWB filter:** As the notched-UWB filter is designed using exponentially tapered impedance line stub loaded microstrip resonator, the input-output feedlines,  $50 \Omega$  main line and the resonator can be demonstrated in the form of equivalent circuit containing series or parallel RLC circuits. If the circuit parameters R, L and C extracted correctly, then S-parameters and group delay can be plotted. Hence, the results

## 7. Conclusions and future work

---

from equivalent circuit analysis can be compared with the theoretical, simulated and measured results of the filter for the another validation.

- (2) **Ultra-broadband filtering power divider using tapers:** The linearly tapered coupled-line BPF, presented in Chapter 3, possibly can further be extended to design compact and ultra-broadband filtering power divider by properly utilizing defected ground structure (DGS) and placing the third tapered section coupled with the existing two linearly tapered coupled-line sections. The broadband nature of tapers can also be used in the design of other highly compact and efficient UWB or even SWB filtering power dividers.
- (3) **Super-wideband (SWB) filter design using tapers:** As it has been seen from reflection coefficient magnitude response for the tapers that setting length of the taper and choosing the frequency above which there will be minimum reflections, possibly over a very large bandwidth, can further be used for designing filter with a SWB bandwidth.
- (4) **New SSPPs structure implementation in SIW:** New shape of SSPPs exhibiting higher field confinement and better slow-wave characteristics can be designed and implemented in SIW for achieving excellent passband and wide out-of-band rejection simultaneously for different microwave and millimetre wave applications. As we have proposed circular dumbbell-shaped SSPP, rectangular dumbbell-shaped SSPP and other types are also possible which might shows even better slow-wave characteristics. The dimensional synthesis of hybrid SSPPs-SIW structures would also be a great future scope.

# Bibliography

- [1] P. Chen, L. Li, K. Yang, and Q. Chen, "Hybrid spoof surface plasmon polariton and substrate integrated waveguide broadband bandpass filter with wide out-of-band rejection," *IEEE Microwave and Wireless Components Letters*, vol. 28, no. 11, pp. 984–986, 2018.
- [2] D. M. Pozar, *Microwave engineering*. John Wiley & Sons, 2009.
- [3] R. E. Collin, *Foundations for microwave engineering*. John Wiley & Sons, 2007.
- [4] R. Collin, "The optimum tapered transmission line matching section," *Proceedings of the IRE*, vol. 44, no. 4, pp. 539–548, 1956.
- [5] R. W. Klopfenstein, "A transmission line taper of improved design," *Proceedings of the IRE*, vol. 44, no. 1, pp. 31–35, 1956.
- [6] M. A. Grossberg, "Extremely rapid computation of the Klopfenstein impedance taper," *Proceedings of the IEEE*, vol. 56, no. 9, pp. 1629–1630, 1968.
- [7] F. E. Gardiol, *Introduction to microwaves*. Artech House, 1984.
- [8] E. J. Wilkinson, "An N-way hybrid power divider," *IRE Transactions on Microwave Theory and Techniques*, vol. 8, no. 1, pp. 116–118, 1960.
- [9] "IEEE standard definitions of terms for antennas," *IEEE No 145-1973*, pp. 1–18, Aug 1973.
- [10] R. Collin, "Theory and design of wide-band multisection quarter-wave transformers," *Proceedings of the IRE*, vol. 43, no. 2, pp. 179–185, 1955.
- [11] G. L. Matthaei, L. Young, and E. M. T. Jones, *Microwave filters, impedance-matching networks, and coupling structures*. Artech House, 1980.
- [12] R. N. Ghose, "Exponential transmission lines as resonators and transformers," *IRE Transactions on Microwave Theory and Techniques*, vol. 5, no. 3, pp. 213–217, 1957.
- [13] C. P. Womack, "The use of exponential transmission lines in microwave components," *IRE Transactions on Microwave Theory and Techniques*, vol. 10, no. 2, pp. 124–132, 1962.
- [14] M. Khalaj-Amirhosseini, "Microstrip nonuniform impedance resonators," *Progress In Electromagnetics Research*, vol. 67, pp. 329–339, 2007.
- [15] A. Toscano, L. Vegni, and F. Urbani, "Exponentially tapered nonuniform transmission lines for high-pass filter design," *Microwave and Optical Technology Letters*, vol. 16, no. 4, pp. 227–229, 1997.
- [16] M. Le Roy, A. Pérennec, S. Toutain, and L. C. Calvez, "The continuously varying transmission-line technique-application to filter design," *IEEE Transactions on Microwave Theory and Techniques*, vol. 47, no. 9, pp. 1680–1687, 1999.
- [17] G. Xiao, K. Yashiro, N. Guan, and S. Ohkawa, "An effective method for designing nonuniformly coupled transmission-line filters," *IEEE Transactions on Microwave Theory and Techniques*, vol. 49, no. 6, pp. 1027–1031, 2001.
- [18] B. Kumar and G. Branner, "Application of empirical models to design microstrip tee junctions with prespecified power-divider ratios," in *Proceedings of 40th Midwest Symposium on Circuits and Systems. Dedicated to the Memory of Professor Mac Van Valkenburg*, vol. 1. IEEE, 1997, pp. 577–580.

## BIBLIOGRAPHY

---

- [19] B. Mencia-Oliva, A. Pelaez-Perez, P. Almorox-Gonzalez, and J. Alonso, "New technique for the design of ultra-broadband power dividers based on tapered lines," in *2009 IEEE MTT-S International Microwave Symposium Digest*. IEEE, 2009, pp. 493–496.
- [20] Z. Lin and Q.-X. Chu, "A novel compact UWB power divider for spatial power combining," *Journal of Electromagnetic Waves and Applications*, vol. 23, no. 13, pp. 1803–1812, 2009.
- [21] C. J. R. Smith and H. H. Sigmarsson, "Microstrip T-junction power divider with exponentially tapered transmission lines," *IEEE Microwave and Wireless Components Letters*, vol. 26, no. 12, pp. 987–989, 2016.
- [22] R. Sinha, R. Chatterjee, and H. Son, "Comments on "microstrip T-junction power divider with exponentially tapered transmission lines"," *IEEE Microwave and Wireless Components Letters*, vol. 27, no. 11, pp. 1037–1038, 2017.
- [23] S. Mathur and A. Sinha, "Design of microstrip exponentially tapered lines to match helical antennas to standard coaxial transmission lines," in *IEE Proceedings H-Microwaves, Antennas and Propagation*, vol. 135, no. 4. IET, 1988, pp. 272–274.
- [24] Y. Chen, W. T. Joines, Z. Xie, G. Shi, Q. H. Liu, and L. Carin, "Double-sided exponentially tapered GPR antenna and its transmission line feed structure," *IEEE Transactions on Antennas and Propagation*, vol. 54, no. 9, pp. 2615–2623, 2006.
- [25] R. S. Kshetrimayum and R. Pillalamarri, "Novel UWB printed monopole antenna with triangular tapered feed lines," *IEICE Electronics Express*, vol. 5, no. 8, pp. 242–247, 2008.
- [26] M. Manohar, R. S. Kshetrimayum, and A. K. Gogoi, "Printed monopole antenna with tapered feed line, feed region and patch for super wideband applications," *IET Microwaves, Antennas & Propagation*, vol. 8, no. 1, pp. 39–45, 2014.
- [27] K. Lu, "An efficient method for analysis of arbitrary nonuniform transmission lines," *IEEE Transactions on Microwave Theory and Techniques*, vol. 45, no. 1, pp. 9–14, 1997.
- [28] C. L. Edwards, M. L. Edwards, S. Cheng, R. K. Stilwell, and C. C. Davis, "A simplified analytic CAD model for linearly tapered microstrip lines including losses," *IEEE Transactions on Microwave Theory and Techniques*, vol. 52, no. 3, pp. 823–830, 2004.
- [29] M. H. Eghlidi, K. Mehrany, and B. Rashidian, "Analytical approach for analysis of nonuniform lossy/lossless transmission lines and tapered microstrips," *IEEE Transactions on Microwave Theory and Techniques*, vol. 54, no. 12, pp. 4122–4129, 2006.
- [30] U. F. C. Commission, "Revision of part 15 of the commission's rules regarding ultra-wideband transmission systems," *First Report and Order, ET Docket*, pp. 98–153, 2002.
- [31] G. R. Aiello and G. D. Rogerson, "Ultra-wideband wireless systems," *IEEE Microwave Magazine*, vol. 4, no. 2, pp. 36–47, 2003.
- [32] L. Zhu, S. Sun, and R. Li, *Microwave bandpass filters for wideband communications*. John Wiley & Sons, 2011.
- [33] J.-S. G. Hong and M. J. Lancaster, *Microstrip filters for RF/microwave applications*. John Wiley & Sons, 2004.
- [34] J.-T. Kuo and E. Shih, "Wideband bandpass filter design with three-line microstrip structures," in *2001 IEEE MTT-S International Microwave Symposium Digest (Cat. No. 01CH37157)*, vol. 3. IEEE, 2001, pp. 1593–1596.
- [35] —, "Wideband bandpass filter design with three-line microstrip structures," *IEE Proceedings-Microwaves, Antennas and Propagation*, vol. 149, no. 5, pp. 243–247, 2002.
- [36] L. Zhu, H. Bu, and K. Wu, "Aperture compensation technique for innovative design of ultra-broadband microstrip bandpass filter," in *2000 IEEE MTT-S International Microwave Symposium Digest (Cat. No. 00CH37017)*, vol. 1. IEEE, 2000, pp. 315–318.

- [37] W. Menzel, L. Zhu, K. Wu, and F. Bogelsack, "On the design of novel compact broad-band planar filters," *IEEE Transactions on Microwave Theory and Techniques*, vol. 51, no. 2, pp. 364–370, 2003.
- [38] C.-L. Hsu, F.-C. Hsu, and J.-K. Kuo, "Microstrip bandpass filters for ultra-wideband (UWB) wireless communications," in *IEEE MTT-S International Microwave Symposium Digest, 2005*. IEEE, 2005, pp. 679–682.
- [39] H. Wang, L. Zhu, and W. Menzel, "Ultra-wideband bandpass filter with hybrid microstrip/CPW structure," *IEEE Microwave and Wireless Components Letters*, vol. 15, no. 12, pp. 844–846, 2005.
- [40] H. Wang and L. Zhu, "Ultra-wideband bandpass filter using back-to-back microstrip-to-CPW transition structure," *Electronics Letters*, vol. 41, no. 24, pp. 1337–1338, 2005.
- [41] L. Zhu, S. Sun, and W. Menzel, "Ultra-wideband (UWB) bandpass filters using multiple-mode resonator," *IEEE Microwave and Wireless Components Letters*, vol. 15, no. 11, pp. 796–798, 2005.
- [42] L. Zhu and H. Wang, "Ultra-wideband bandpass filter on aperture-backed microstrip line," *Electronics Letters*, vol. 41, no. 18, pp. 1015–1016, 2005.
- [43] S. Sun and L. Zhu, "Capacitive-ended interdigital coupled lines for UWB bandpass filters with improved out-of-band performances," *IEEE Microwave and Wireless Components Letters*, vol. 16, no. 8, pp. 440–442, 2006.
- [44] R. Li and L. Zhu, "Compact UWB bandpass filter using stub-loaded multiple-mode resonator," *IEEE Microwave and Wireless Components Letters*, vol. 17, no. 1, pp. 40–42, 2007.
- [45] B. Yao, Y. Zhou, Q. Cao, and Y. Chen, "Compact UWB bandpass filter with improved upper-stopband performance," *IEEE Microwave and Wireless Components Letters*, vol. 19, no. 1, pp. 27–29, 2008.
- [46] P. Cai, Z. Ma, X. Guan, Y. Kobayashi, T. Anada, and G. Hagiwara, "A novel compact ultra-wideband bandpass filter using a microstrip stepped-impedance four-modes resonator," in *2007 IEEE/MTT-S International Microwave Symposium*. IEEE, 2007, pp. 751–754.
- [47] P. Cai, Z. Ma, X. Guan, X. Yang, Y. Kobayashi, T. Anada, and G. Hagiwara, "A compact UWB bandpass filter using two-section open-circuited stubs to realize transmission zeros," in *2005 Asia-Pacific Microwave Conference Proceedings*, vol. 5. IEEE, 2005, pp. 4–pp.
- [48] J.-S. Hong and H. Shaman, "An optimum ultra-wideband microstrip filter," *Microwave and Optical Technology Letters*, vol. 47, no. 3, pp. 230–233, 2005.
- [49] A. M. Abbosh, "Planar bandpass filters for ultra-wideband applications," *IEEE transactions on microwave theory and techniques*, vol. 55, no. 10, pp. 2262–2269, 2007.
- [50] J.-K. Lee and Y.-S. Kim, "Ultra-wideband bandpass filter with improved upper stopband performance using defected ground structure," *IEEE Microwave and Wireless Components Letters*, vol. 20, no. 6, pp. 316–318, 2010.
- [51] A. M. Abbosh, "Design method for ultra-wideband bandpass filter with wide stopband using parallel-coupled microstrip lines," *IEEE Transactions on microwave theory and techniques*, vol. 60, no. 1, pp. 31–38, 2011.
- [52] G.-M. Yang, R. Jin, C. Vittoria, V. Harris, and N. Sun, "Small ultra-wideband (UWB) bandpass filter with notched band," *IEEE Microwave and Wireless Components Letters*, vol. 18, no. 3, pp. 176–178, 2008.
- [53] H. Shaman and J.-S. Hong, "Ultra-wideband (UWB) bandpass filter with embedded band notch structures," *IEEE Microwave and Wireless Components Letters*, vol. 17, no. 3, pp. 193–195, 2007.
- [54] W. Zong, X. Zhu, C. You, and J. Wang, "Design and implement of compact UWB bandpass filter with a frequency notch by consisting of coupled microstrip line structure, DGS and EOS," in *2009 International Conference on Advanced Technologies for Communications*. IEEE, 2009, pp. 179–182.
- [55] S. S. Karthikeyan and R. S. Kshetrimayum, "Notched UWB bandpass filter using complementary single split ring resonator," *IEICE Electronics Express*, vol. 7, no. 17, pp. 1290–1295, 2010.

## BIBLIOGRAPHY

---

- [56] R. Uikey, R. S. Sangam, K. Prasadu, and R. S. Kshetrimayum, "Novel notched UWB filter using stepped impedance stub loaded microstrip resonator and spurlines," *International Journal of Microwave Science and Technology*, vol. 2015, 2015.
- [57] F. Wei, L. Chen, X.-W. Shi, X. H. Wang, and Q. Huang, "Compact UWB bandpass filter with notched band," *Progress In Electromagnetics Research*, vol. 4, pp. 121–128, 2008.
- [58] F. Wei, Q. Y. Wu, X. W. Shi, and L. Chen, "Compact UWB bandpass filter with dual notched bands based on SCRLH resonator," *IEEE Microwave and Wireless Components Letters*, vol. 21, no. 1, pp. 28–30, 2010.
- [59] M. M. Honari, L. Mirzavand, R. Mirzavand, A. Abdipour, and P. Mousavi, "Theoretical design of broadband multisection wilkinson power dividers with arbitrary power split ratio," *IEEE Transactions on Components, Packaging and Manufacturing Technology*, vol. 6, no. 4, pp. 605–612, 2016.
- [60] M. Villegas, G. Branner, P. B. Kumar, and W. Keese, "Analysis and design of microwave T-junction circuits for prescribed response characteristics," in *Proceedings of 36th Midwest Symposium on Circuits and Systems*. IEEE, 1993, pp. 604–607.
- [61] P. B. Kumar, G. Branner, G. Razmafrouz, and D. Brody, "Optimization of microwave T junction power-divider circuits," in *Proceedings of 1994 37th Midwest Symposium on Circuits and Systems*, vol. 2. IEEE, 1994, pp. 1235–1237.
- [62] G. Branner, B. P. Kumar, and D. Thomas, "Design of microstrip T junction power divider circuits for enhanced performance," in *38th Midwest Symposium on Circuits and Systems. Proceedings*, vol. 2. IEEE, 1995, pp. 1213–1215.
- [63] G. Branner, B. Kumar, and D. James, "Design formulae for a class of microstrip tee junction power-divider circuits," in *Proceedings of the 39th Midwest Symposium on Circuits and Systems*, vol. 3. IEEE, 1996, pp. 1351–1354.
- [64] D. M. Pozar, "Microstrip antenna aperture-coupled to a microstripline," *Electronics Letters*, vol. 21, no. 2, pp. 49–50, 1985.
- [65] P. Sullivan and D. Schaubert, "Analysis of an aperture coupled microstrip antenna," *IEEE Transactions on Antennas and Propagation*, vol. 34, no. 8, pp. 977–984, 1986.
- [66] D. Pozar, "A reciprocity method of analysis for printed slot and slot-coupled microstrip antennas," *IEEE Transactions on Antennas and Propagation*, vol. 34, no. 12, pp. 1439–1446, 1986.
- [67] M. Rahim, Z. Low, P. Soh, A. Asrokin, M. Jamaluddin, and T. Masri, "Aperture coupled microstrip antenna with different feed sizes and aperture positions," in *2006 International RF and Microwave Conference*. IEEE, 2006, pp. 31–35.
- [68] M. Civerolo and D. Arakaki, "Aperture coupled patch antenna design methods," in *2011 IEEE International Symposium on Antennas and Propagation (APSURSI)*. IEEE, 2011, pp. 876–879.
- [69] A. Adrian and D. Schaubert, "Dual aperture-coupled microstrip antenna for dual or circular polarisation," *Electronics Letters*, vol. 23, no. 23, pp. 1226–1228, 1987.
- [70] Y. Murakami, W. Chujo, I. Chiba, and M. Fujise, "Dual slot-coupled microstrip antenna for dual frequency operation," *Electronics Letters*, vol. 29, no. 22, pp. 1906–1907, 1993.
- [71] B. Lindmark, "A novel dual polarized aperture coupled patch element with a single layer feed network and high isolation," in *IEEE Antennas and Propagation Society International Symposium 1997. Digest*, vol. 4. IEEE, 1997, pp. 2190–2193.
- [72] K.-L. Wong, H.-C. Tung, and T.-W. Chiou, "Broadband dual-polarized aperture-coupled patch antennas with modified H-shaped coupling slots," *IEEE Transactions on Antennas and Propagation*, vol. 50, no. 2, pp. 188–191, 2002.
- [73] Y. Chung, S.-S. Jeon, D. Ahn, J.-I. Choi, and T. Itoh, "High isolation dual-polarized patch antenna using integrated defected ground structure," *IEEE Microwave and Wireless Components Letters*, vol. 14, no. 1, pp. 4–6, 2004.

- [74] S. Li, X. Cao, J. Gao, and P. Gao, "High-isolation dual-polarized microstrip antenna via substrate integrated waveguide technology," *Radioengineering*, vol. 23, no. 4, pp. 1092–1098, 2014.
- [75] C.-C. Chang, J.-S. Row *et al.*, "Dual-feed dual-polarized patch antenna with low cross polarization and high isolation," *IEEE Transactions on Antennas and Propagation*, vol. 57, no. 10, pp. 3405–3409, 2009.
- [76] K. Luo, W.-P. Ding, Y.-J. Hu, and W.-Q. Cao, "Design of dual-feed dual-polarized microstrip antenna with high isolation and low cross polarization," *Progress in Electromagnetics Research*, vol. 36, pp. 31–40, 2013.
- [77] B. Wang, Y. Zhuang, and X. Li, "Compact dual ports handheld RFID reader antenna with high isolation," *International Journal of RF and Microwave Computer-Aided Engineering*, vol. 25, no. 6, pp. 548–555, 2015.
- [78] C. Goodbody, T. Karacolak, and N. Tran, "Dual-polarised patch antenna for in-band full-duplex applications," *Electronics Letters*, vol. 54, no. 22, pp. 1255–1256, 2018.
- [79] G. Makar, N. Tran, and T. Karacolak, "A high-isolation monopole array with ring hybrid feeding structure for in-band full-duplex systems," *IEEE Antennas and Wireless Propagation Letters*, vol. 16, pp. 356–359, 2016.
- [80] I. Acimovic, D. A. McNamara, and A. Petosa, "Dual-polarized microstrip patch planar array antennas with improved port-to-port isolation," *IEEE Transactions on Antennas and Propagation*, vol. 56, no. 11, pp. 3433–3439, 2008.
- [81] Q. Ye, D. Wang, M. Wang, W. Wu, and J. Zhao, "Design of a dual-feed orthogonal polarized patch antenna array," in *2010 International Conference on Microwave and Millimeter Wave Technology*. IEEE, 2010, pp. 1031–1034.
- [82] B. Li, Y.-Z. Yin, Y. Zhao, Y. Ding, and R. Zou, "Dual-polarised patch antenna with low cross-polarisation and high isolation for WiMAX applications," *Electronics Letters*, vol. 47, no. 17, pp. 952–953, 2011.
- [83] J. R. Panda and R. S. Kshetrimayum, "A printed 2.4 GHz/5.8 GHz dual-band monopole antenna with a protruding stub in the ground plane for WLAN and RFID applications," *Progress In Electromagnetics Research*, vol. 117, pp. 425–434, 2011.
- [84] Y. Li, W. Li, and Q. Ye, "A compact asymmetric coplanar strip-fed dual-band antenna for 2.4/5.8 GHz WLAN applications," *Microwave and Optical Technology Letters*, vol. 55, no. 9, pp. 2066–2070, 2013.
- [85] D. Deslandes and K. Wu, "Integrated microstrip and rectangular waveguide in planar form," *IEEE Microwave and Wireless Components Letters*, vol. 11, no. 2, pp. 68–70, 2001.
- [86] —, "Design consideration and performance analysis of substrate integrated waveguide components," in *2002 32nd European Microwave Conference*. IEEE, 2002, pp. 1–4.
- [87] Y. Cassivi, L. Perregrini, P. Arcioni, M. Bressan, K. Wu, and G. Conciauro, "Dispersion characteristics of substrate integrated rectangular waveguide," *IEEE Microwave and Wireless components letters*, vol. 12, no. 9, pp. 333–335, 2002.
- [88] D. Deslandes and K. Wu, "Single-substrate integration technique of planar circuits and waveguide filters," *IEEE Transactions on Microwave Theory and Techniques*, vol. 51, no. 2, pp. 593–596, 2003.
- [89] —, "Millimeter-wave substrate integrated waveguide filters," in *CCECE 2003-canadian conference on electrical and computer engineering. toward a caring and humane technology (cat. no. 03ch37436)*, vol. 3. IEEE, 2003, pp. 1917–1920.
- [90] M. Bozzi, A. Georgiadis, and K. Wu, "Review of substrate-integrated waveguide circuits and antennas," *IET Microwaves, Antennas & Propagation*, vol. 5, no. 8, pp. 909–920, 2011.
- [91] D. Deslandes, "Design equations for tapered microstrip-to-substrate integrated waveguide transitions," in *2010 IEEE MTT-S International Microwave Symposium*. IEEE, 2010, pp. 704–707.
- [92] X.-P. Chen and K. Wu, "Substrate integrated waveguide filter: Basic design rules and fundamental structure features," *IEEE Microwave Magazine*, vol. 15, no. 5, pp. 108–116, 2014.

## BIBLIOGRAPHY

---

- [93] D. Zelenchuk and V. Fusco, "Low insertion loss substrate integrated waveguide quasi-elliptic filters for V-band wireless personal area network applications," *IET Microwaves, Antennas & Propagation*, vol. 5, no. 8, pp. 921–927, 2011.
- [94] R. C. Caleffo, "New design procedure to determine the taper transition for impedance matching between microstrip line and SIW component," *Journal of Microwaves, Optoelectronics and Electromagnetic Applications*, vol. 15, no. 3, pp. 247–260, 2016.
- [95] Q. Zhang, H. C. Zhang, H. Wu, and T. J. Cui, "A hybrid circuit for spoof surface plasmons and spatial waveguide modes to reach controllable band-pass filters," *Scientific Reports*, vol. 5, p. 16531, 2015.
- [96] D.-F. Guan, P. You, Q. Zhang, K. Xiao, and S.-W. Yong, "Hybrid spoof surface plasmon polariton and substrate integrated waveguide transmission line and its application in filter," *IEEE Transactions on Microwave Theory and Techniques*, vol. 65, no. 12, pp. 4925–4932, 2017.
- [97] K. Rudramuni, K. Kandasamy, A. Kandwal, and Q. Zhang, "Compact bandpass filter based on hybrid spoof surface plasmon and substrate integrated waveguide transmission line," in *2017 IEEE Electrical Design of Advanced Packaging and Systems Symposium (EDAPS)*. IEEE, 2017, pp. 1–3.
- [98] D.-F. Guan, P. You, Q. Zhang, Z.-B. Yang, H. Liu, and S.-W. Yong, "Slow-wave half-mode substrate integrated waveguide using spoof surface plasmon polariton structure," *IEEE Transactions on Microwave Theory and Techniques*, vol. 66, no. 6, pp. 2946–2952, 2018.
- [99] D.-F. Guan, P. You, Z.-B. Yang, S.-D. Xu, X. Huang, and S.-W. Yong, "A broadband filter based on hybrid spoof surface plasmon and half-mode substrate integrated waveguide structure," *International Journal of RF and Microwave Computer-Aided Engineering*, vol. 29, no. 5, p. e21558, 2019.
- [100] L. Zhao, Y. Li, Z.-M. Chen, X.-H. Liang, J. Wang, X. Shen, and Q. Zhang, "A band-pass filter based on half-mode substrate integrated waveguide and spoof surface plasmon polaritons," *Scientific Reports*, vol. 9, no. 1, pp. 1–8, 2019.
- [101] H.-R. Ahn, I. Wolff, and N.-H. Myung, "Small-sized wideband CVT-and CCT-ring filters," in *IEEE MTT-S International Microwave Symposium Digest, 2003*, vol. 3. IEEE, 2003, pp. 1607–1610.
- [102] F. Wei, W. T. Li, X. W. Shi, and Q. L. Huang, "Compact UWB bandpass filter with triple-notched bands using triple-mode stepped impedance resonator," *IEEE Microwave and Wireless Components Letters*, vol. 22, no. 10, pp. 512–514, 2012.
- [103] S. C. Gupta, M. Kumar, and R. S. Meena, "Design & analysis of a microstrip line multi band UWB filter," *AEU-International Journal of Electronics and Communications*, vol. 70, no. 11, pp. 1556–1564, 2016.
- [104] R. Johnson, "Design of linear double tapers in rectangular waveguides," *IRE Transactions on Microwave Theory and Techniques*, vol. 7, no. 3, pp. 374–378, 1959.
- [105] N. Ghassemi, I. Boudreau, D. Deslandes, and K. Wu, "Millimeter-wave broadband transition of substrate integrated waveguide on high-to-low dielectric constant substrates," *IEEE Transactions on Components, Packaging and Manufacturing Technology*, vol. 3, no. 10, pp. 1764–1770, 2013.
- [106] K. Li, D. Kurita, and T. Matsui, "An ultrawideband bandpass filter using broadside-coupled microstrip-coplanar waveguide structure," in *IEEE MTT-S International Microwave Symposium Digest, 2005*. IEEE, 2005, pp. 4–pp.
- [107] J.-S. Kim, N.-S. Kim, W.-G. Moon, S.-G. Byeon, and H. Shin, "A novel broadband suspended substrate stripline filter using resonators with T-shaped open-circuited stubs," in *2007 IEEE/MTT-S International Microwave Symposium*. IEEE, 2007, pp. 917–920.
- [108] J.-S. Park, J.-S. Yun, and D. Ahn, "A design of the novel coupled-line bandpass filter using defected ground structure with wide stopband performance," *IEEE Transactions on Microwave Theory and Techniques*, vol. 50, no. 9, pp. 2037–2043, 2002.
- [109] K. Matsushita and M. Fukuda, "Frequency characteristics of 1-D periodic structures with tapered microstrip lines," *IEEJ Transactions on Electrical and Electronic Engineering*, vol. 5, no. 2, pp. 245–250, 2010.

- [110] H. Heshmati and S. Roshani, "A miniaturized lowpass bandpass diplexer with high isolation," *AEU-International Journal of Electronics and Communications*, vol. 87, pp. 87–94, 2018.
- [111] A. Emadeddin, S. Shad, Z. Rahimian, and H. Hassani, "High mutual coupling reduction between microstrip patch antennas using novel structure," *AEU-International Journal of Electronics and Communications*, vol. 71, pp. 152–156, 2017.
- [112] P. K. Panda and D. Ghosh, "Isolation and gain enhancement of patch antennas using EMNZ superstrate," *AEU-International Journal of Electronics and Communications*, vol. 86, pp. 164–170, 2018.
- [113] R. Garg, I. Bahl, and M. Bozzi, *Microstrip lines and slotlines*. Artech house, 2013.
- [114] Y. Leviatan, P. G. Li, A. T. Adams, and J. Perini, "Single-post inductive obstacle in rectangular waveguide," *IEEE Transactions on Microwave Theory and Techniques*, vol. 31, no. 10, pp. 806–812, 1983.
- [115] S. A. Maier, *Plasmonics: fundamentals and applications*. Springer Science & Business Media, 2007.
- [116] W. L. Barnes, A. Dereux, and T. W. Ebbesen, "Surface plasmon subwavelength optics," *Nature*, vol. 424, no. 6950, p. 824, 2003.
- [117] J. Pendry, L. Martin-Moreno, and F. Garcia-Vidal, "Mimicking surface plasmons with structured surfaces," *Science*, vol. 305, no. 5685, pp. 847–848, 2004.
- [118] F. Garcia-Vidal, L. Martin-Moreno, and J. Pendry, "Surfaces with holes in them: new plasmonic metamaterials," *Journal of Optics A: Pure and Applied Optics*, vol. 7, no. 2, p. S97, 2005.
- [119] Q. Gan, Z. Fu, Y. J. Ding, and F. J. Bartoli, "Ultrawide-bandwidth slow-light system based on THz plasmonic graded metallic grating structures," *Physical Review Letters*, vol. 100, no. 25, p. 256803, 2008.
- [120] S. A. Maier, S. R. Andrews, L. Martin-Moreno, and F. Garcia-Vidal, "Terahertz surface plasmon-polariton propagation and focusing on periodically corrugated metal wires," *Physical Review Letters*, vol. 97, no. 17, p. 176805, 2006.
- [121] X. Shen, T. J. Cui, D. Martin-Cano, and F. J. Garcia-Vidal, "Conformal surface plasmons propagating on ultrathin and flexible films," *Proceedings of the National Academy of Sciences*, vol. 110, no. 1, pp. 40–45, 2013.
- [122] H. F. Ma, X. Shen, Q. Cheng, W. X. Jiang, and T. J. Cui, "Broadband and high-efficiency conversion from guided waves to spoof surface plasmon polaritons," *Laser & Photonics Reviews*, vol. 8, no. 1, pp. 146–151, 2014.
- [123] Z. Liao, J. Zhao, B. C. Pan, X. P. Shen, and T. J. Cui, "Broadband transition between microstrip line and conformal surface plasmon waveguide," *Journal of Physics D: Applied Physics*, vol. 47, no. 31, p. 315103, 2014.
- [124] L. Ye, Y. Xiao, Y. Liu, L. Zhang, G. Cai, and Q. H. Liu, "Strongly confined spoof surface plasmon polaritons waveguiding enabled by planar staggered plasmonic waveguides," *Scientific Reports*, vol. 6, p. 38528, 2016.
- [125] X. Gao, W. Che, and W. Feng, "Novel non-periodic spoof surface plasmon polaritons with H-shaped cells and its application to high selectivity wideband bandpass filter," *Scientific Reports*, vol. 8, no. 1, p. 2456, 2018.
- [126] Z.-C. Hao, W. Hong, J.-X. Chen, X.-P. Chen, and K. Wu, "Compact super-wide bandpass substrate integrated waveguide (SIW) filters," *IEEE Transactions on Microwave Theory and Techniques*, vol. 53, no. 9, pp. 2968–2977, 2005.
- [127] L. Geng, W. Che, and K. Deng, "Wideband bandpass filter of folded substrate-integrated waveguide integrating with stripline compact resonant cell," *Microwave and Optical Technology Letters*, vol. 50, no. 2, pp. 390–393, 2008.
- [128] L.-S. Wu, X.-L. Zhou, and W.-Y. Yin, "Ultra-wideband bandpass filter using half-mode T-septum substrate integrated waveguide with electromagnetic bandgap structures," *Microwave and Optical Technology Letters*, vol. 51, no. 7, pp. 1751–1755, 2009.

## BIBLIOGRAPHY

---

- [129] R. S. Chen, S.-W. Wong, L. Zhu, and Q.-X. Chu, "Wideband bandpass filter using U-slotted substrate integrated waveguide (SIW) cavities," *IEEE Microwave and Wireless Components Letters*, vol. 25, no. 1, pp. 1–3, 2014.
- [130] M. Salehi and E. Mehrshahi, "A closed-form formula for dispersion characteristics of fundamental SIW mode," *IEEE Microwave and Wireless Components Letters*, vol. 21, no. 1, pp. 4–6, 2010.



---

## List of Publications

### Journal Publications:

- **R. S. Sangam** and R. S. Kshetrimayum, “Notched UWB filter using exponential tapered impedance line stub loaded microstrip resonator,” *The Journal of Engineering (IET)*, vol. 2018, no. 9, pp. 768-772, Sept. 2018.
- **R. S. Sangam**, S. Poolakkal, R. Palthiya, N. Nallam and R. S. Kshetrimayum, “Dual-port, aperture coupled and tapered fed patch antenna for full-duplex ISM applications,” *Microwave and Optical Technology Letters (Wiley)*, vol. 61, no. 2, pp. 542-545, Feb. 2019.
- **R. S. Sangam** and R. S. Kshetrimayum, “Comment on “Hybrid spoof surface plasmon polariton and substrate integrated waveguide broadband bandpass filter with wide out-of-band rejection” ,” *IEEE Microwave and Wireless Components Letters*, vol. 30, no. 2, pp. 222-222, Feb. 2020.
- **R. S. Sangam**, Sumit Dash and R. S. Kshetrimayum, “Ultra-broadband bandpass filter using linearly tapered coupled-microstrip line and open loop defected ground structure,” *IEEE Transactions on Circuits and Systems II: Express Briefs* (Accepted for Publication on 13<sup>th</sup> July 2020).

### Conference Publications:

- **R. S. Sangam** and R. S. Kshetrimayum, “Approximate design equation for iris width calculation of iris substrate integrated waveguide (SIW) bandpass filters,” in *Proc. National Conference on Communications (NCC)*, Chennai, India, Mar. 2017.
- **R. S. Sangam** and R. S. Kshetrimayum, “Linear tapers: analysis, design and applications,” in *Proc. IEEE MTT-S International Microwave and RF Conference (IMaRC)*, Kolkatta, India, Nov. 2018.
- **R. S. Sangam** and R. S. Kshetrimayum, “An improved T-junction power divider using linearly tapered microstrip lines,” in *Proc. 2019 URSI Asia-Pacific Radio Science Conference (AP-RASC 2019)*, New Delhi, India, Mar. 2019.

## Manuscripts Under Review:

- **R. S. Sangam** and R. S. Kshetrimayum, “Hybrid spoof surface plasmon polariton and substrate integrated waveguide bandpass filter with high out-of-band rejection for X-band applications,” *IET Microwaves, Antennas & Propagation* (Under Review).



---

## Bio-Data

- 1 Name: Ramanand Sagar Sangam
  
- 2 Date of Birth: 15-July-1988  
  
August-2012, B. Tech. in Electronics & Communication Engineering (9.31/10 CGPA),  
The ICFAI University Dehradun,  
Uttarakhand, India
  
- 3 Educational Qualification: July-2014, M. Tech. in Electronics & Communication Engineering (Microwaves) (8.72/10 CGPA),  
The University of Burdwan,  
West Bengal, India  
  
March-2020, Ph.D (Thesis Submitted),  
Indian Institute of Technology Guwahati,  
Assam, India
  
- 4 Permanent Address: S/O Mr. Babulal Prasad  
At: Gaipahadi  
Post: Kalhabad  
Via: Barkatha  
District: Hazaribagh  
Jharkhand, India  
Pincode-825323
  
- 5 Contact Address: Communication Lab 2,  
Dept. of EEE,  
Indian Institute of Technology Guwahati,  
Guwahati, Assam, India  
Pincode-781039
  
- 6 Contact Number: (+91)-9085848928

